THESIS FOR THE DEGREE OF DOCTOR OF PHILOSOPHY

Modified Vanadium Oxide Catalysts for the Selective Catalytic Reduction of NO_x

Alexander Nellessen

Department of Chemistry and Chemical Engineering
CHALMERS UNIVERSITY OF TECHNOLOGY

Göteborg, Sweden 2025

Modified Vanadium Oxide Catalysts for the Selective Catalytic Reduction of NO_x
ALEXANDER NELLESSEN

© Alexander Nellessen, 2025
ISBN: 978-91-8103-278-9

Doktorsavhandlingar vid institutionen för kemi och kemiteknik
Chalmers tekniska högskola
Ny serie nr 5736
ISSN 0346-718X

Department of Chemistry and Chemical Engineering
Chalmers University of Technology
SE-412 96 Göteborg
Sweden
Telephone: +46 (0)767084885

Cover:
Illustration of an titania-supported vanadium oxide catalyst for the NO_x emission control in mobile sources, such as trucks. Nitrogen oxide gases (brown) are converted in presence of ammonia into harmless nitrogen and water (blue).

Printed by Chalmers Reproservice
Göteborg, Sweden 2025

Modified Vanadium Oxide Catalysts for the Selective Catalytic Reduction of NO_x
ALEXANDER NELLESSEN

Department of Chemistry and Chemical Engineering
Chalmers University of Technology

Abstract

Combustion processes in diesel engines are expected to play a significant role in the foreseeable future, especially in heavy-duty vehicles. In response to increasingly stringent legislations aimed at reducing emissions of nitrogen oxides (NO_x), considerable efforts have been devoted to developing effective technologies. Among them, the selective catalytic reduction (SCR) with ammonia (NH_3) is the most established method for both stationary and mobile sources. To date, titania-supported vanadium oxides (VO_x/TiO_2) are the most widespread SCR catalyst type in use. However, the application in vehicles presents several challenges due to the dynamic conditions. Both low-temperature activity and high-temperature stability are crucial due to temperature fluctuations in the exhaust gas. Catalyst development has focused on enhancing the activity by modification of the active VO_x species and the support.

In this work, the effects of the vanadium loading and catalyst modification were investigated, with a particular emphasis on the behavior after thermal stress, representing a critical factor in the context of mobile source applications. Promising results have been achieved through the modification with oxides of cerium (Ce), niobium (Nb), and antimony (Sb), demonstrating the optimization potential of V-based SCR catalysts. The results showed that the Ce-modification results in an improved low-temperature activity, while the incorporation of Nb contributes to a higher thermal stability. Remarkable catalyst activation was observed after aging upon Sb-modification. The addition of modifiers enhanced the stability by limiting sintering processes of both the TiO_2 and VO_x species. Infrared spectroscopic methods allowed the identification of surface VO_x species, surface hydroxyl groups, and adsorbed surface species of the reactants and products (NH_3, NO, H_2O). Further, the decomposition of the NO adsorption spectra enabled a comparison of the surface species ratio among the samples and provide potential for future in-depth spectroscopic studies. This thesis encourages further exploration of VO_x/TiO_2 catalysts to improve fundamental knowledge about catalyst design in the NO_x emission control and beyond other applications.

Keywords: NH_3-SCR, NO_x emission control, vanadium oxide, VO_x, titania, aging, Nb, Ce, Sb

List of Publications

This thesis is based on the following appended papers:

Paper I:
Impact of vanadium loading and thermal aging on surface properties of titania supported vanadium oxide NH_3-SCR catalysts
Alexander Nellessen, Andreas Schaefer, Anna Martinelli, Agnes Raj, Andrew Newman, and Per-Anders Carlsson
The Journal of Physical Chemistry C ***128*** *(2024) 2894-2908.*

Paper II:
Effect of thermal aging on Ce- and Nb-modified VO_x/TiO_2 NH_3-SCR catalysts
Alexander Nellessen, Roberta Villamaina, Andreas Schaefer, Anna Martinelli, Agnes Raj, Andrew Newman, and Per-Anders Carlsson
Submitted

Paper III:
Antimony modification of VO_x/TiO_2 NH_3-SCR catalysts and the effect of thermal aging
Alexander Nellessen, Roberta Villamaina, Andreas Schaefer, Anna Martinelli, Agnes Raj, Andrew Newman, and Per-Anders Carlsson
Journal of Catalysis ***450*** *(2025) 116303.*

Paper IV:
In situ infrared spectroscopic characterization of water adsorption on titania-supported vanadium oxide catalysts modified with cerium, niobium or antimony
Alexander Nellessen, Andreas Schaefer, Roberta Villamaina, Anna Martinelli, and Per-Anders Carlsson
Manuscript

Paper V:
The effect of thermal ageing and addition of CeO_x, NbO_x and SbO_x on the structure of dispersed VO_x in low-loaded anatase-supported vanadia catalysts
Alexander Nellessen, Iliana-Maria Stergiou, Roberta Villamaina, Andreas Schaefer, Anna Martinelli, Per-Anders Carlsson, and Soghomon Boghosian
Manuscript

My Contribution

Paper I
I planned and performed the experiments except for the sample preparation, activity, XPS measurements, and XPS analysis. I analyzed the data, interpreted the results, and wrote the first draft of the manuscript, which was finalized together with my co-authors.

Paper II
I planned and performed the experiments except for the sample preparation, activity, and XRF measurements. I analyzed the data, interpreted the results with my co-authors, and wrote the first draft of the manuscript.

Paper III
I planned and performed the experiments except for the sample preparation and activity measurements. I analyzed the data and interpreted the results together with my co-authors and wrote the first draft of the manuscript.

Paper IV
I planned and performed the experiments except for the sample preparation. I analyzed the data, interpreted the results with my co-authors, and wrote the first draft of the manuscript.

Paper V
I proposed the concept and planned the experiments. I carried out parts of the experimental work and data treatment, except for peak fitting. I interpreted the results together with my co-authors and wrote the first draft of the manuscript.

List of Figures

1.1 NO_x emissions by source sector and Euro emission standards for heavy-duty vehicles . . . 2
1.2 Temperature operating window of a VO_x/TiO_2 catalyst . . . 3

2.1 Illustration of a catalytic cycle as a sequence of elementary steps 8
2.2 Schematic illustration of the E-R, L-H, or M-vK mechanism . . 8
2.3 Schematic representation of the NH_3-SCR in mobile sources . . . 10
2.4 Ammonia adsorbed on Lewis and Brønsted acid sites of a vanadium oxide species . . . 11
2.5 Standard SCR mechanism proposed by Topsøe et al. . . . 12
2.6 Structures of monomeric, polymeric and crystalline vanadium oxide species on the catalyst surface . . . 14

3.1 Representation of flow reactor setup . . . 20
3.2 Simplified mechanism of X-ray fluorescence catalyst . . . 21
3.3 Illustration of the BET theory . . . 22
3.4 Schematic representation of a TPD experiment. . . . 23
3.5 Schematic representation of Bragg's law . . . 24
3.6 Interaction of IR light with matter . . . 26
3.7 Vibrational modes of isolated ammonia . . . 26
3.8 Schematic illustration of the in situ DRIFTS setup . . . 27
3.9 Example of a difference IR spectrum for the ammonia adsorption 28
3.10 Example of peak-fitted spectrum and illustration of peak profiles 30

4.1 NO_x conversion and N_2O formation over the VO_x/TiO_2 catalysts before and after aging . . . 35
4.2 Comparison of specific surface area and TiO_2-anatase crystallite size for the TiO_2 support as well as VO_x/TiO_2 catalysts before and after aging . . . 36
4.3 NH_3-TPD profiles and determined NH_3 uptake of the VO_x/TiO_2 catalysts and TiO_2 support . . . 37
4.4 Background-subtracted X-ray patterns and normalized Raman spectra of the VO_x/TiO_2 catalysts before and after aging . . 38
4.5 NO_x conversion and specific rate over the modified VO_x/TiO_2 catalysts before and after aging . . . 42
4.6 N_2O formation over the modified VO_x/TiO_2 catalysts before and after aging . . . 43

4.7 Comparison of specific surface area of the modified TiO_2 as well as VO_x/TiO_2 catalysts before and after aging. 44
4.8 Comparison of determined NH_3 uptake of the modified TiO_2 as well as VO_x/TiO_2 catalysts before and after aging. 44
4.9 Background-subtracted X-ray patterns and Raman spectra of the modified VO_x/TiO_2 catalysts before and after aging . . . 45
4.10 Proposed structures of dispersed VO_x species 47
4.11 In situ Raman spectra of the unmodified VO_x/TiO_2 sample before and after aging 48
4.12 Peak-fitted in situ Raman spectrum and proportion of the species in the spectra of V/Ti 48
4.13 In situ Raman spectra of the modified VO_x/TiO_2 before and after aging 49
4.14 DRIFT NH_3 adsorption spectra of the VO_x/TiO_2 catalysts and TiO_2 support 53
4.15 Proposed structure of ammonia adsorbed on monomeric and polymeric Brønsted acid sites 53
4.16 DRIFT NH_3 adsorption spectra of the modified TiO_2 before and after aging 55
4.17 DRIFT NH_3 adsorption spectra of the modified VO_x/TiO_2 catalysts before and after aging 56
4.18 Schematic illustration of the consequences of the aging procedure and the deactivation mechanisms 58
4.19 Structures of surface nitrate species on metal oxides 59
4.20 DRIFT spectra for the adsorption of NO at room temperature on the VO_x/TiO_2 catalysts as well as TiO_2 support 60
4.21 Decomposed spectrum and relative abundance of NO_x species on the VO_x/TiO_2 catalysts as well as TiO_2 support 61
4.22 Summary of peak-fitted spectra with relative abundance of NO_x species on the modified TiO_2 and VO_x/TiO_2 catalysts before and after aging. 62
4.23 Structure of adsorbed H_2O with different numbers of hydrogen bonds 63
4.24 DRIFT spectra for the adsorption of H_2O on the VO_x/TiO_2 catalysts as well as TiO_2 support 64
4.25 DRIFT spectra for the adsorption and desorption of H_2O on the modified VO_x/TiO_2 catalysts 65

Notation

BET	Brunauer-Emmett-Teller
DRIFTS	Diffuse reflectance infrared Fourier transform spectroscopy
FTIR	Fourier transform infrared spectroscopy
FWHM	Full width at half maximum
IR	Infrared
NO_x	Nitrogen oxides
SCR	Selective catalytic reduction
SSA	Specific surface area
TPD	Temperature programmed desorption
VO_x	Vanadium oxide
XPS	X-ray photoelectron spectroscopy
XRD	X-ray diffraction
XRF	X-ray fluorescence

Contents

Abstract iii

List of Publications vi

List of Figures vii

Notation ix

Contents xi

1 Introduction 1
- 1.1 Air pollution and emission regulation . . . 1
- 1.2 Challenges in the mobile emission control . . . 3
- 1.3 Objective of this thesis . . . 5

2 Background 7
- 2.1 Heterogeneous catalysis . . . 7
- 2.2 Selective catalytic reduction of nitrogen oxides with ammonia 9
- 2.3 Reaction mechanisms . . . 11
- 2.4 Vanadium-based SCR catalysts . . . 13
  - 2.4.1 W- and Si-modified VO_x/TiO_2 catalysts . . . 14
  - 2.4.2 Other modifiers . . . 15

3 Methodology 17
- 3.1 Sample preparation and aging procedure . . . 18
- 3.2 Catalytic tests . . . 19
- 3.3 Catalyst elemental composition and texture . . . 20
  - 3.3.1 X-ray fluorescence spectrometry . . . 20
  - 3.3.2 Nitrogen physisorption . . . 21
  - 3.3.3 Temperature programmed desorption . . . 23
  - 3.3.4 Powder X-ray diffraction . . . 24
- 3.4 Spectroscopic techniques . . . 25
  - 3.4.1 Diffuse Reflectance Infrared Fourier Transform Spectroscopy . . . 26
  - 3.4.2 Raman spectroscopy . . . 29
  - 3.4.3 Peak profiles and decomposition . . . 30

4 Results and Discussion 33

4.1 Investigation of VO_x/TiO_2 reference catalysts 33
4.1.1 Catalytic performance and thermal stability as a function of vanadium loading 34
4.1.2 Correlation between catalyst texture and SCR activity 35
4.2 Modification of VO_x/TiO_2 with Ce, Nb, and Sb 40
4.2.1 Catalyst performance and stability 41
4.2.2 Impact of the modifiers on the catalyst texture 43
4.2.3 Effect of the modifiers on the dispersed VO_x structure 46
4.3 Surface characterization by molecular probe infrared spectroscopy 51
4.3.1 Adsorption of ammonia 52
4.3.2 Adsorption of nitrogen monoxide 59
4.3.3 Adsorption of water 63

5 Conclusions and Outlook **67**

1 Introduction

1.1 Air pollution and emission regulation

The awareness and better scientific understanding of health and environmental issues caused by exhaust gases from combustion processes have brought these concerns to public attention. Those exhaust gases contain a variety of harmful pollutants, such as carbon monoxide, particulate matter, and nitrogen oxides (NO_x). In particular, NO_x gases contribute to respiratory illnesses, cardiovascular problems, acid rain, as well as ozone layer depletion [1, 2]. With escalating complications of smog in urban areas and mega-cities, government agencies across the world have established emission regulations, and thus ongoing efforts have focused on the development of cleaner technologies, stricter emission standards, as well as alternative energy solutions [3].

Diesel engines are widely used in the transportation sector in heavy-duty vehicles, ships, as well as for stationary purposes in compressors, pumps, or generators. Further applications can be found in agriculture, such as tractors or harvesters, and in construction, including bulldozers, cranes, or drilling equipment. The cost-efficient operation, higher thermodynamic efficiency, and robustness make diesel engines irreplaceable to date [4]. However, diesel engines operate continuously in an oxidizing environment (lean conditions, excess of oxygen in the exhaust gas), resulting in the unavoidable formation of NO_x gases. The term NO_x refers to nitrogen monoxide (NO) along with nitrogen dioxide (NO_2). As the transport sector is the largest source of NO_x emissions (Fig. 1.1), the first NO_x regulation in Europe was introduced in 1992 for light- and heavy-duty vehicles (Euro I) [5]. Since then, the emission standards have been regularly adjusted with increasingly stringent restrictions. In the upcoming Euro VII proposal (expected introduction in 2027), a NO_x emission standard of not more than $0.09\,\mathrm{g{\cdot}kWh^{-1}}$ is designated for heavy-duty vehicles [6]. Further, restrictions for nitrous oxide (N_2O) are considered, as N_2O is a strong greenhouse gas with approximately 300 times the warming potential of CO_2 [7].

A variety of techniques have been implemented to tackle this issue. The abatement of NO_x emissions in mobile sources can be categorized into three

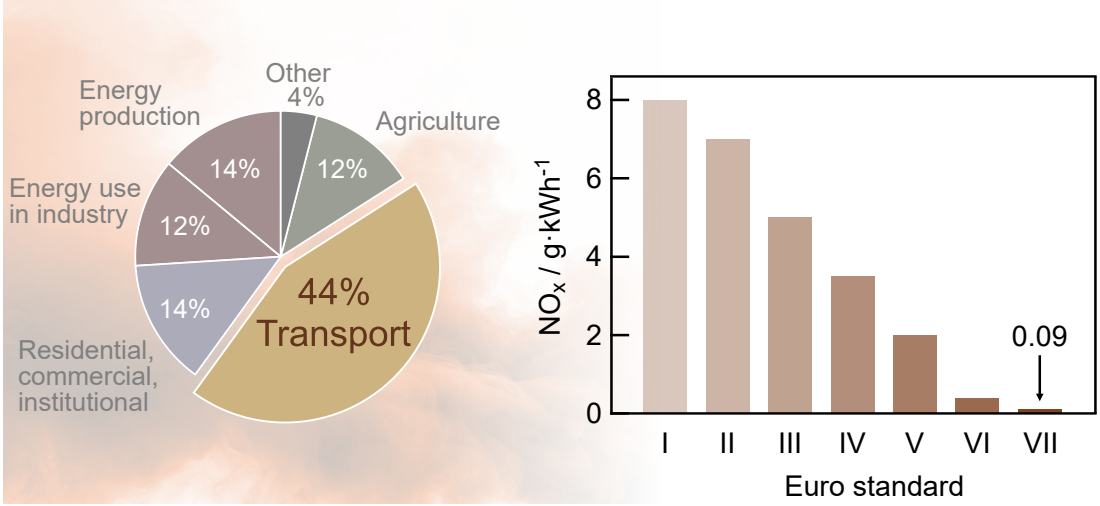

Figure 1.1: *NO_x emissions in the EU divided by source sector [8] (left) and historical Euro NO_x emission standards for heavy-duty vehicles (right). Data taken from [6, 9].*

classes, which include pre-combustion, combustion, and post-combustion modifications [10, 11]. The pre-combustion control can be achieved by lowering the nitrogen content in the fuel. In the combustion control, the emphasis lies on engine modifications such as an improved fuel delivery system and ignition timing. Although the pre-combustion and combustion control contribute to a reduction of the NO_x formation, they only achieve a moderate decrease of the total NO_x emissions [12]. Nowadays, the produced NO_x from the oxidation of organic nitrogen in the fuel is less considerable, due to the decrease of the nitrogen content in gasoline and diesel. The post-combustion control focuses on reducing the NO_x gases after they have been formed. This after-treatment approach is considered the most suitable for complying with the emission regulations, and has initiated research in the catalysis field since the 1980s.

The most commonly used technology is the selective catalytic reduction, which utilizes ammonia as a reducing agent (NH_3-SCR) to convert NO_x gases to nitrogen and water. However, the limited space in the after-treatment system and the dynamic environment involving fluctuating temperatures and exhaust gas compositions remain a challenge.

1.2 Challenges in the mobile emission control

The NH_3-SCR technology using titania-supported vanadium oxide (VO_x/TiO_2) catalysts was initially introduced in the 1970s in Japan for stationary systems [13, 14], until 1985 employed in Europe [4]. In the mid-1990s, development projects focused on the adaptation for diesel truck and car engines, coinciding with the introduction of the Euro IV emission standards in 2005 [15, 16]. The application in mobile sources involves different requirements and certain challenges that have to be addressed. In general, the catalysts must achieve a high efficiency and perform reliably in this dynamic system.

An unmodified VO_x/TiO_2 catalyst shows good performance in the temperature range of 300 to 400 °C, with a NO_x conversion over 90%, which, however, significantly declines outside that range (Fig. 1.2). Short-distance driving or cold starts lead to lower temperatures (≥150 °C), posing the risk of ammonium sulfate formation, which can block the catalyst surface as well as corrosion of the equipment [4]. Long-range drives on highways result in higher temperatures (≤650 °C), which can lead to the formation of V_2O_5 and potential vanadium release starting from 500 °C [17].

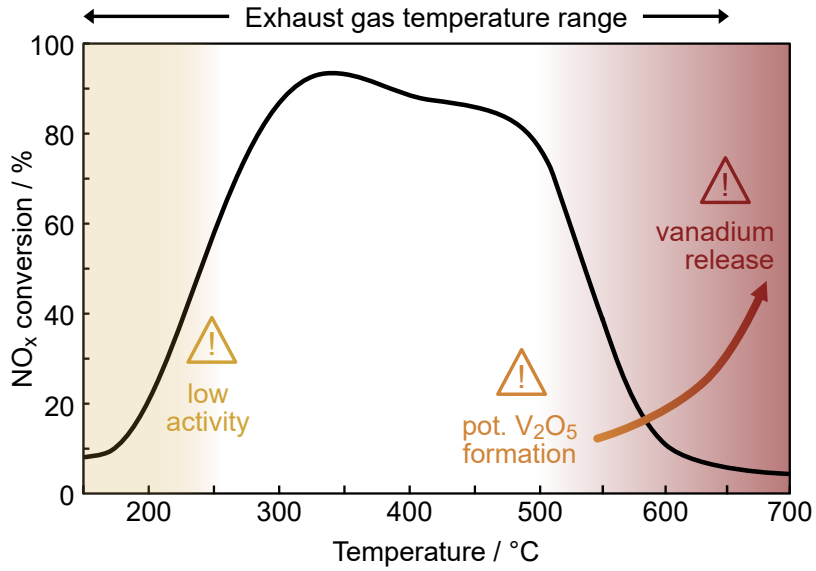

Figure 1.2: *Temperature operating window of a VO_x/TiO_2 catalyst: NO_x conversion versus temperature.*

V_2O_5 is declared as a harmful pollutant causing incidental hazard risks to human health and the environment [18] coupled with strict disposal limits [19, 20]. In addition, high temperatures cause side reactions such as the formation of N_2O or the oxidation of ammonia, resulting in an overall lower total efficiency.

The gradual loss of catalytic activity over time and understanding the corresponding processes, such as structural changes and the loss of active sites, are an essential subject of investigation. Placing the catalyst in a vehicle represents the best possible testing approach, to which a given catalyst is exposed under real driving conditions. Automotive manufacturers use vehicle aging test procedures; however, the use of such methods is usually limited due to the high efforts and costs. To address this, so-called accelerated "aging" procedures have been developed, mimicking the long-term application. An aging protocol may include tests in an atmosphere-controlled lab furnace, aiming to investigate the catalysts at elevated temperatures in the presence of water (hydrothermal aging) or specific contaminants (chemical aging). Since the primary factor is the catalyst's thermal stability, the exposure to high temperatures is a primary factor to be tested (thermal aging), especially when evaluating several new catalyst compositions.

In summary, an ideal catalyst should withstand peak temperatures up to 650 °C without releasing vanadium, should also be low-temperature active, and should not be affected by any contaminants. Further, the catalyst durability while maintaining a good performance is an important aspect to meet the vehicle's lifetime. In order to face the challenges for the application in mobile sources, the development of suitable SCR catalysts has focused on the modification with metal oxide additives to promote the activity over an expanded temperature range and to stabilize both the vanadium oxide species and the support. Commercially available catalysts are commonly modified with tungsten oxide (W); however, the development of this modifier is close to maturity. Since the activity at lower temperatures is of special interest, there is a driving force to explore alternative elements as promoters. Provided that both the activity and stability can be improved, the VO_x/TiO_2 system remains a relevant material platform for industrial catalysts and encourages further fundamental research.

1.3 Objective of this thesis

The goal of this work is to improve the fundamental understanding of VO_x/TiO_2 catalysts for the application in mobile sources, and guide towards a more rational catalyst design. The thesis is divided into three sections. The first part (Chapter 4.1) focuses on unmodified VO_x/TiO_2 catalysts with a varying vanadium content. The characterization of the catalysts and the impact of thermal aging, reflecting a long-term usage, was investigated. This chapter is based on the publication in "Journal of Physical Chemistry C" (*J. Phys. Chem. C* 2024, 128, 7, 2894–2908).

The second part (Chapter 4.2) addresses the improvement of the thermal stability and durability of VO_x/TiO_2 catalysts, and the impact of different modifiers (oxides of Sb, Ce, or Nb) on the catalyst was investigated in terms of activity and catalyst texture, in fresh state and after thermal aging. The chapter is based on publications in "Journal of Catalysis", (*J.Catal.* 2025, 450, 116303) and two manuscripts.

The final part (Chapter 4.3) focuses on surface characterization *via* infrared spectroscopy. The adsorption of ammonia (NH_3), nitrogen monoxide (NO), and water (H_2O) facilitates precise surface characterization in terms of adsorbed species on the surface as well as adsorption sites, and is thereby essential for the interpretation under complex and more application-relevant conditions.

2 Background

2.1 Heterogeneous catalysis

Catalysis can be described as a modification or an increase in the rate of a chemical reaction. In simpler terms, a chemical reaction occurs faster or with a reduced energy demand (e.g., temperature, pressure) with a catalyst. As a consequence, around 90% of all industrial chemical processes involve the utilization of catalysts and highlight their importance to industry and society [21].

A catalyst may be a single atom, molecule, or more complex structure, such as an enzyme, that bonds with the reactants, initiating the reaction to form a product, but it is not consumed by the reaction. In "heterogeneous catalysis", the catalyst is in a different phase (commonly solid) than the reactants (gaseous/liquid), which brings the benefit that it is easy to separate from the reactants and products of the reaction. Therefore, around 80% of all industrially utilized catalysts are heterogeneous catalysts [22]. The essential part of a heterogeneous catalyst is the active sites (or active centers), which are usually dispersed on an inert carrier material or support. The support is typically a high surface area material, and it is generally preferred to maximize the number of active sites per volume.

A catalytic reaction is a cyclic event (Fig. 2.1a) where the catalyst participates in the reaction and regenerates to its initial state at the end of each cycle [23]. In principle, for a chemical reaction to happen, an energy barrier must be overcome. A catalyst provides an alternative reaction pathway, which may involve several steps, in which reactants form intermediates and undergo structural changes. Still, the overall energy barrier is lower compared to a non-catalyzed reaction (Fig. 2.1b).

Understanding the reaction mechanism is crucial for an improved catalyst design. Several mechanisms for catalytic reactions are known, depending on how the adsorption takes place (cf. Fig. 2.2). The Eley-Rideal mechanism describes the adsorption of a molecule, followed by the reaction with another directly from the gas phase, without prior adsorption. The Langmuir-Hinshelwood mechanism defines the adsorption of two molecules on two neighboring surface sites, followed by a bimolecular reaction. The characteristic feature of the Mars-van Krevelen mechanism is the reaction

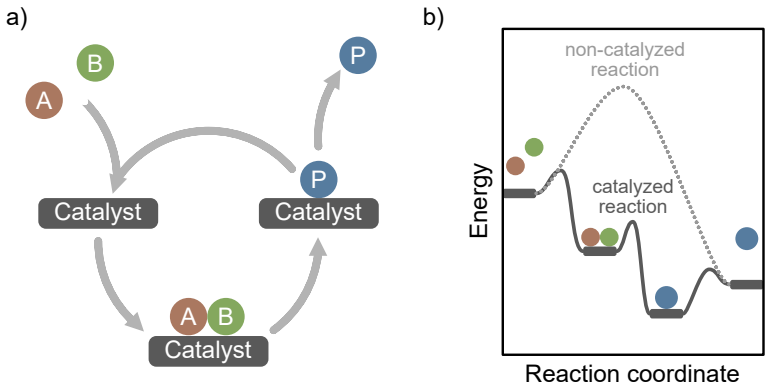

Figure 2.1: *a) Illustration of a catalytic cycle as a sequence of elementary steps. The reactants A and B adsorb on the catalyst to form the product P. b) Potential energy diagram of a catalytic reaction compared to a non-catalyzed reaction.*

of the adsorbed molecule with one or more constituents from the catalyst surface (often oxygen), leaving a vacancy that is regenerated through surface adsorption or lattice diffusion of the respective component [24].

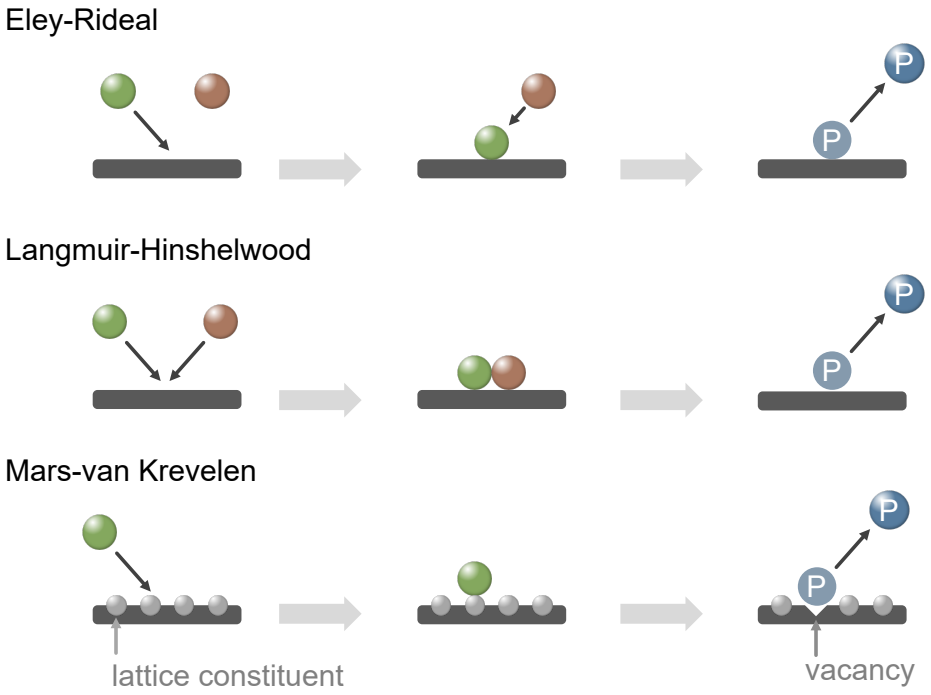

Figure 2.2: *Schematic illustration of the Eley-Rideal, Langmuir-Hinshelwood, and Mars-van Krevelen mechanism.*

2.2 Selective catalytic reduction of nitrogen oxides with ammonia

The selective catalytic reduction of nitrogen oxides (NO_x) with ammonia (NH_3) has been established as the foremost technology to comply with the increasingly stringent NO_x emission regulations. In the SCR reaction, gaseous NO_x and ammonia are selectively converted to harmless water and nitrogen (cf. Fig. 2.3). The main reaction in this process is the "Standard-SCR", in which equimolar amounts of ammonia and NO react in the presence of oxygen to form the products (Eq. 2.1). When NO_2 is present (∼10% in automotive exhaust [25]), the so-called "Fast-SCR" reaction (Eq. 2.2) takes place, which proceeds at a higher reaction rate, especially at lower temperatures [26].

$$4\,NO + 4\,NH_3 + O_2 \rightarrow 4\,N_2 + 6\,H_2O \tag{2.1}$$

$$NO + NO_2 + 2\,NH_3 \rightarrow 2\,N_2 + 3\,H_2O \tag{2.2}$$

Potential side reactions at higher temperatures demonstrate a serious obstacle, lowering the total SCR reaction efficiency and leading to the formation of nitrous oxide (N_2O), as shown in Eq. 2.3. Further, the oxidation of ammonia can contribute to formation of N_2O (Eq. 2.4).

$$4\,NO + 4\,NH_3 + 3\,O_2 \rightarrow 4\,N_2O + 6\,H_2O \tag{2.3}$$

$$2\,NH_3 + 2\,O_2 \rightarrow N_2O + 3\,H_2O \tag{2.4}$$

In stationary applications, catalyst bricks are grouped into metal frames, and the catalyst is held in place by their geometric structure [4]. For mobile applications, the catalyst is either washcoated onto an inert monolith substrate or extruded so that the monolith consists of the catalyst material. The monolith type structure (Fig. 2.3) provides a high contact area and mechanical strength to withstand forces and vibrations, which the catalysts will be exposed to within the vehicle. The installation of gaseous or liquid ammonia in mobile sources is not preferred due to the hazards and potential risks. Instead, a urea solution ($CO(NH_2)_2$) commonly known as AdBlue© (32 wt% urea in water) is used as an NH_3 source and is injected into the combustion gas stream. In the presence of water and heat, urea is converted to ammonia and carbon dioxide (Eq. 2.5).

$$CO(NH_2)_2 + H_2O \rightarrow 2\,NH_3 + CO_2 \tag{2.5}$$

For the exhaust after-treatment in mobile sources, the NH_3-SCR unit is only one unit within the system. Other units include the diesel oxidation catalyst (DOC), which partially oxidizes unburned hydrocarbons and NO to NO_2, diesel particulate filters (DPFs) remove soot particles, and finally an ammonia slip catalyst (ASC) oxidizes excess NH_3 not converted in the NH_3-SCR unit. Additional components, such as NO_x monitor sensors, are used for proper control to regulate the urea injection system. Moreover, a differential pressure sensor is installed in the DPF to monitor pressure drops, due to soot and ash build-up in the filter, which affects engine efficiency [27, 28].

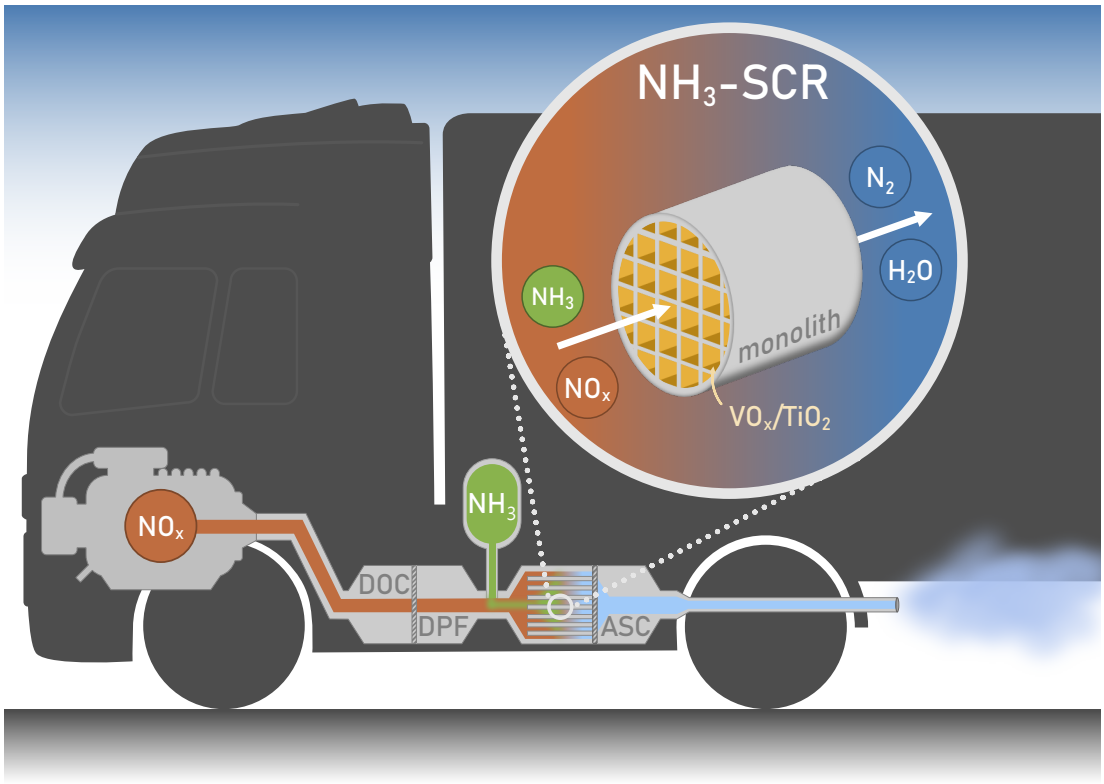

Figure 2.3: *Schematic representation of the NH_3-SCR in mobile sources: The exhaust gas composition containing NO_x flows through diesel oxidation catalysis (DOC), diesel particulate filters (DPF) until ammonia is injected in form of an urea solution prior to the NH_3-SCR unit. Any excess ammonia is removed via ammonia slip catalysis (ASC).*

2.3 Reaction mechanisms

Over the years, several NH_3-SCR reaction mechanisms for vanadium-based catalysts have been proposed. It is important to note that supported vanadium oxides have a formal oxidation state of either V^{5+} or V^{4+}, respectively, holding oxidized V=O or hydrolyzed V-OH groups, which play an important role in the SCR reaction. Ammonia, as a key reactant, adsorbs on those sites either as surface NH_3 on a Lewis acid site coordinated to the vanadium atom. Alternatively, the adsorption on a Brønsted acid site involves the abstraction of a proton from the V-OH group, consequently forming surface NH_4^+, as illustrated in Fig. 2.4.

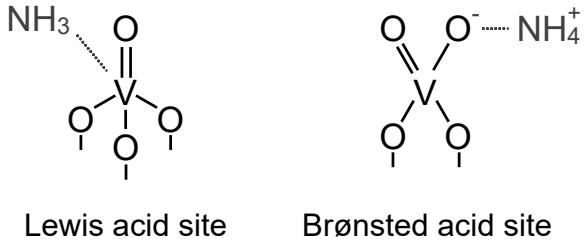

Figure 2.4: *Ammonia adsorbed on Lewis and Brønsted acid sites of a vanadium oxide (V^{5+}) species.*

The first popular proposal was an Eley-Rideal type mechanism, where ammonia is adsorbed on a Brønsted acid site followed by the reaction with gas phase NO to form N_2 and H_2O [29]. Further, a "nitrosamide" mechanism was proposed, with the ammonia adsorption occurring on a Lewis acid site, due to the higher thermal stability of the coordinated form of ammonia. It involves breaking of the N-H bond to form a radical-like amide species. The produced species reacts with gas phase NO to form a nitrosamide intermediate (NH_2NO), which readily decomposes to the products [30, 31].

A combination of both mechanisms was introduced by Topsøe et al. [32] and contains both an acid and a redox cycle. In this reaction mechanism, ammonia adsorbs on a Brønsted acid site (Step 1) and is activated by an adjacent vanadium V=O site, followed by the reaction with gaseous or weakly adsorbed NO (Step 2). The intermediate converts to N_2 and H_2O (Step 3), while partially reducing the vanadium site. Lastly, the reduced site is regenerated by oxygen (Step 4). Here, the activity is correlated to the number of Brønsted acid sites.

Despite the fact that these catalysts have been used and studied for decades, the exact nature of the NH_3-SCR reaction is still a subject of several investigations. Advances in *in situ* or *operando* spectroscopic techniques, as well as computational studies, continuously provide new

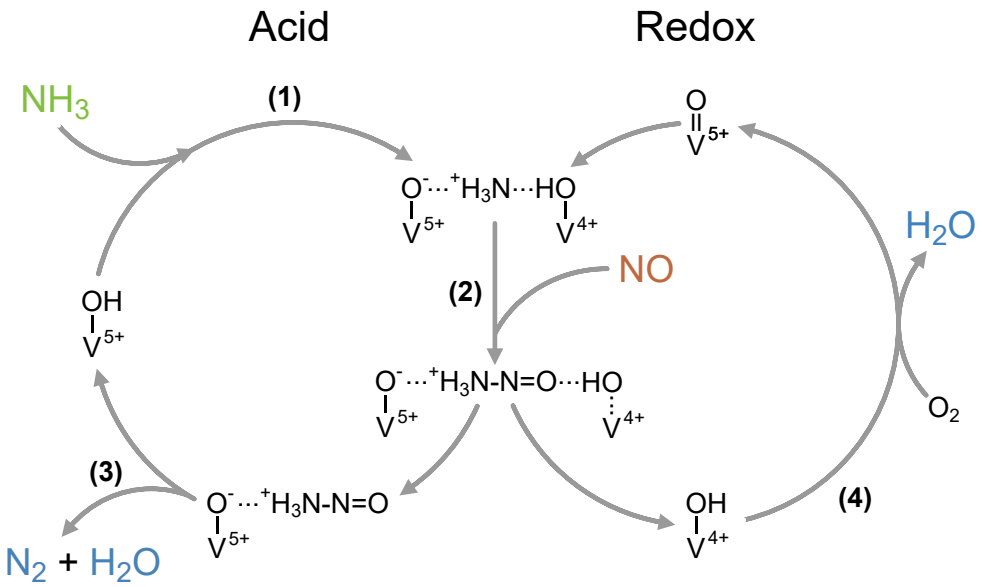

Figure 2.5: *Standard SCR mechanism proposed by Topsøe et al. [32]. The first step involves the ammonia adsorption (1) and activation by an adjacent V=O site. The reaction with NO (2) leads to the formation of water and nitrogen (3), and the reduced site is reoxidized (4).*

insights. Based on the mechanism by Topsøe [32], the formulation of a standard and fast SCR mechanism [26] and also a mechanism over monomeric and polymeric vanadium species [33] have been elaborated. Transient IR and Raman spectroscopic studies delivered further insights on mechanistic details, such as the importance of the Lewis acid sites, which are more active than Brønsted acid sites in the SCR reaction [34, 35]. Both TiO_2 and VO_x sites have been proposed to be involved in the SCR reaction, with only a fraction of coordinatively unsaturated VO_x being active, and the support that acts as a reservoir for ammonia [34, 36]. Studies with isotopically labeled reactants have shown that the nitrogen atoms that produce N_2 originate from both NH_3 and NO. Moreover, experiments with $^{18}O_2$ showed that oxygen from the TiO_2 lattice could have an active role in both the SCR reaction and ammonia oxidation, and the reoxidation step occurs with gas phase O_2 via the Mars-van Krevelen mechanism [35].

2.4 Vanadium-based SCR catalysts

Different types of SCR catalysts are used, including noble metals, metal oxides, or zeolites [37]. Among these titania-supported vanadium oxides (VO_x/TiO_2) have been used from the very beginning and are the most commonly used catalysts in urea-based SCR systems because of their high activity, even for a low vanadium content (∼1–2 wt%), and the relatively low material costs compared to other systems. Further advantages are the high chemical resistance to sulfuric compounds [14] and the low formation of nitrous oxide (N_2O) [38], considering potential N_2O emission standards for heavy-duty vehicles [6]. Anatase-TiO_2 is considered to be the most suitable support given to the high dispersion of the VO_x surface species [39], chemical robustness [40] and resistance to corrosive gases such as SO_2 and SO_3 [41, 42]. Besides the prominent application the NH_3-SCR reaction [43], further utilization is found in the valorization of hydrocarbons by selective oxidation [44], environmental protection by trapping mercury through oxidation (Hg^0 to Hg^{2+}) [45], or the production of sulfuric acid (H_2SO_4) by oxidation of sulfur dioxide (SO_2 to SO_3) [46]. More recently, potential in the biomass conversion to produce valuable fuels and chemicals has been demonstrated [47] and establishes titania-supported vanadium oxide catalysts as an interesting material platform beyond the scope of this work.

The vanadium content or loading plays a crucial role in the activity, selectivity, and thermal stability of the catalyst. Another depiction of the loading can be expressed as surface coverage with vanadium atoms per unit area (V/nm^2). At a low vanadium loading (<2 V/nm^2), the vanadium oxide species are widely dispersed on the support with three bridging Ti-O-V bonds and a terminal vanadyl (V=O) bond (monomeric VO_4 coordination, as displayed in Fig. 2.6). Further increasing the vanadium loading leads to the formation of oligomeric and polymeric VO_4 species with bridging V-O-V bonds up to the theoretical maximum of the monolayer coverage. Polymeric vanadium oxide species have been found to have the highest specific activity, which is associated with the so-called "coupling effect". The interacting adjacent VO_x species shorten the regeneration time of the redox sites, which results in an overall lower energy barrier of the catalytic cycle [33]. When the vanadium loading exceeds the monolayer coverage (>8 V/nm^2), crystalline V_2O_5 particles begin to form [38].

In general, a low vanadium loading is beneficial for the temperature stability as the VO_x species are finely dispersed [48]. A higher vanadium loading improves the low-temperature activity but decreases the thermal stability along with N_2O formation [33] and enhances the SO_2 oxidation. The resulting SO_3 can convert to sulfuric acid (H_2SO_4) in the presence

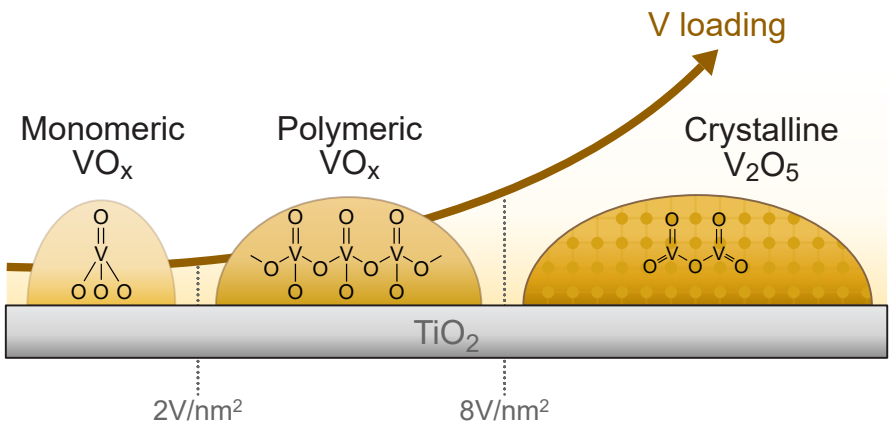

Figure 2.6: *Structures of monomeric, polymeric and crystalline vanadium oxide species on the catalyst surface as a function of vanadium loading.*

of moisture [38, 49, 50] and damage the equipment. Present industrial VO_x-SCR catalysts contain around 1-3 wt% vanadium to achieve a high ratio of polymeric VO_x but also to minimize the undesired side reactions (cf. Section 2.2).

2.4.1 W- and Si-modified VO_x/TiO_2 catalysts

The catalyst development of VO_x/TiO_2 catalyst involved the modification with various modifiers. Tungsten (W) oxide is the most widely used additive for both stationary and mobile applications [4, 51] and has been studied extensively.

The inclusion of tungsten oxide is proposed to have multiple promotional benefits, categorized as either chemical (or electronical) effects as well as structural (or physical) effects. In the first case, tungsten interacts with vanadium by modifying its reducibility, which facilitates the redox properties and thus results in an improved selectivity due to lower ammonia oxidation and extending the operating window [41, 52–55]. In the structural context, the presence of tungsten oxide promotes the polymerization of the VO_x species due to the occupation of the TiO_2 surface, resulting in an improved activity. Additional promotional effects include the improvement of thermal stability of the TiO_2-anatase phase [37, 56], increased acidity [57], and poisoning resistance to alkali metals [54].

Another common additive, often in combination with tungsten, is silicon (Si) oxide, which maintains the stability of the TiO_2 support by counteracting the sintering process [17, 56, 58–61]. However, the presence of silicon oxide can lead to reduced activity at low temperatures, due to coverage of VO_x species [62]. Both the modification with tungsten or silicon

oxide have demonstrated a significant effect on the thermal stability upon aging treatment [56]. In the case of tungsten, hydrothermal aging at 600 °C for 16 hours was shown to activate the catalyst, resulting in a higher NO_x conversion [63].

2.4.2 Other modifiers

Molybdenum (Mo) oxide has been investigated early in the development of these catalysts and has a similar effect on VO_x/TiO_2 as tungsten to prevent catalyst deactivation. The modification with Mo increases the acidity, reduces the NO and SO_2 oxidation, and inhibits TiO_2 sintering. However, the high formation of N_2O at high temperatures makes its application in mobile sources unfeasible [37, 39, 52, 64].

Since the low-temperature activity is a matter of special importance, the addition of cerium oxide (Ce) and manganese oxide (Mn) has recently been considered a promising approach due to their high oxygen storage capacity and redox properties of the active sites [65–68]. On the grounds of their inherent catalytic activity, Mn-based catalysts can be prepared without V, though lack in tolerance to water and SO_2 [65, 66].

The modification with niobium (Nb) oxide has been shown to increase the surface acidity, resistance to SO_2, and SCR performance [69–71] as well as to minimize the formation of crystalline V_2O_5 phases [72].

When antimony (Sb) oxide is added in small amounts, it prevents catalyst poisoning by SO_2, and promotes the decomposition of ammonium bisulfate [73–75], a critical catalyst poisoning compound in SCR applications. Furthermore, the Sb-modification increases the redox ability of the catalyst surface, beneficial for the low-temperature activity [71].

3 Methodology

This chapter provides descriptions of the sample preparation, aging procedure, experimental approaches, and characterization techniques used in this work. The catalytic activity of the prepared samples was evaluated in a gas flow reactor. The quantitative composition of the catalysts was determined by X-ray fluorescence (XRF). As the development for heterogeneous catalysts often aims for a high surface area to give an extensive access for the reactants, the specific surface area (SSA) was determined by N_2-physisorption. The temperature programmed desorption of ammonia (TPD) was used to evaluate the quantity and strength of the interaction between the catalyst surface and ammonia as the key reactant. Further, the existence or formation of crystalline particles on the samples after the aging procedure was investigated by X-ray diffraction (XRD) and Raman spectroscopy. The spectroscopic investigation involves *in situ* DRIFT spectroscopy as a valuable technique to investigate the sample surface as well as adsorbed surface species of the different probing molecules.

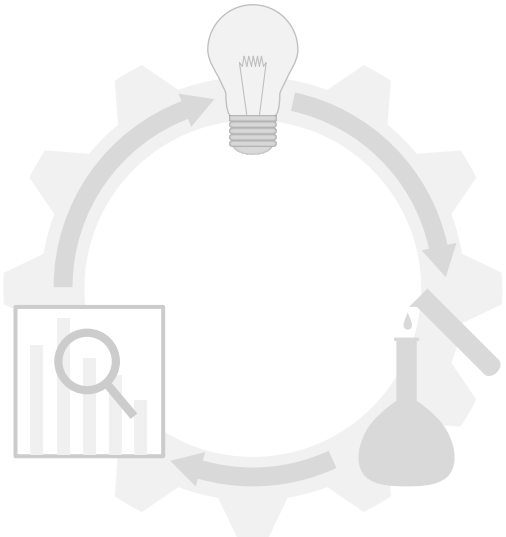

3.1 Sample preparation and aging procedure

The samples were prepared *via* the incipient wetness impregnation, where the support (TiO_2) is mixed with the precursor solution containing the active compound or promoting additives. When more than two components were loaded, the dissolved precursors were mixed beforehand and added by co-impregnation. This technique allows an accurate and reproducible control of the desired compound loading. In addition, low labor and cost requirements, along with minimal waste generation, make it a preferred method to prepare metal oxide catalysts. For the incipient wetness impregnation, the impregnation solution should correspond to the pore volume of the support to ensure a complete incorporation into the pores, without any excess solution. In contrast to that, the wet impregnation describes the preparation in an excess of solution, which is removed, e.g., under heat. The resulting samples underwent the calcination process, heating to 500 °C for one hour, which transforms the catalyst to its active state via removal or decomposition of the non-metallic compounds (such as oxalates, nitrates, etc.).

An overview of the utilized titania support and metal precursors is provided in Table 3.1.

Table 3.1: *Chemicals used for the catalyst preparation and precursor materials*

Name	Formula	Purity
DT51-D TiO_2	TiO_2	99 wt% anatase[a]
Vanadyl (IV) oxalate	$VO(C_2O_4)$	chemically pure[b]
Cerium(III) nitrate	$Ce(NO_3)_3{\cdot}6H_2O$	99.999%[c]
Niobium(V) oxalate	$(NH_4)NbO(C_2O_4)_2$	99.99%[c]
Antimony(III) acetate	$Sb(CH_3O_2)_3$	99.99%[c]

[a] Tronox plc, [b] GfE GmbH, [c] Sigma-Aldrich

As for the practical application in automobiles, the catalysts must maintain high catalytic activity over extended time periods in order to meet the vehicle's lifetime. To address this, the effect of thermal aging was tested. Since the operation temperature in vehicles varies widely, the maximum temperature is not used as the sole aging criterion. In this work, a portion of the prepared samples were thermally aged by exposure to a temperature of 580 °C for 100 hours in static air, representing a common aging protocol for the application in automotives, as reported in literature [48].

3.2 Catalytic tests

Reactor tests are the ultimate method to evaluate the catalytic activity of the prepared catalysts in the projected reaction or to test different reaction conditions. Beyond that, parameters such as the best sample composition, additives, or preparation method can be explored. The reactor experiments may involve testing the catalytic reaction at different temperatures in a controlled gas stream, or the effect of additional compounds (e.g., water or sulfuric compounds) in the stream, depending on the specific application. In this work (**Paper I–III**), the catalytic activity for the NO_x conversion over samples was measured in a fixed-bed flow reactor (Fig. 3.1) under standard SCR conditions. About 0.3 g of each sample, with a particle size of 250-300 µm, was used and pressed into pellets. The reaction conditions were adapted to a typical diesel exhaust gas mixture with a model feed gas containing 500 ppm NO, 525 ppm NH_3, 300 ppm CO, 3% CO_2, 10% O_2, 5 vol% H_2O, with N_2 as carrier. NH_3 was dosed in a slight excess in order to achieve a maximum NO_x conversion, unaffected by any potential side reaction of ammonia. The total gas flow was 2000 $mL \cdot min^{-1}$, representing a gas hourly space velocity of 60,000 h^{-1} as common flow conditions in conventional diesel vehicles [76, 77]. The composition of the effluent gas stream (including N_2O) was continuously analyzed by infrared spectroscopy. The NO_x conversion was determined from the ratio of inlet to outlet concentrations, as shown in Eq. 3.1

$$NO_x \text{ conversion} = \frac{NO_{x,in} - NO_{x,out}}{NO_{x,in}} \cdot 100\% \tag{3.1}$$

The specific rate was calculated by the amount of converted NO (in mol) normalized by the vanadium mass (in gram), which has been determined by X-ray fluorescence (see Section 3.3.1).

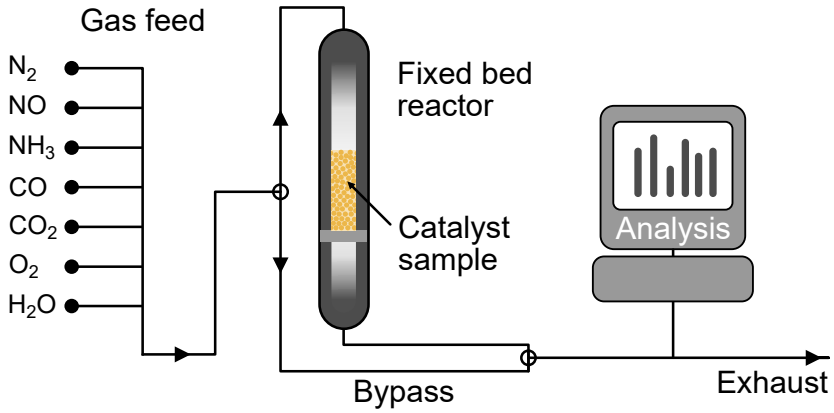

Figure 3.1: *Representation of the flow reactor setup used in this work. The gas feed is regulated with mass flow controllers and can be directed to the reactor or through a bypass. The effluent gas composition is analyzed by an IR spectrometer.*

3.3 Catalyst elemental composition and texture

3.3.1 X-ray fluorescence spectrometry

X-ray fluorescence (XRF) is a non-destructive technique that can be used for qualitative and quantitative analysis to determine the elemental composition of a material, including solids, liquids, or powders, with minimum sample preparation. At the atomic level, the X-ray fluorescence proceeds as follows: First, the sample is irradiated with X-rays, which induces the excitation of an atom within the material, which then ejects an electron from the inner orbital shells. This results in an electron vacancy and an unstable configuration for the atom. Lastly, a higher-energy electron from an outer shell refills the vacancy, lowering its energy, and this excess energy is emitted in the form of fluorescent X-rays (Fig. 3.2). The energy difference between the ejected and replaced electrons is characteristic of every element in which the fluorescence process occurs. These emitted X-rays have energies that are characteristic of the involved elements and transitions. In the resulting spectrum, each element is identified by its peak position, while the intensity or peak height correlates to the concentration.

In **Paper II**, XRF was used to determine the elemental composition of the samples. The measurements were performed with an AXIOS XRF spectrometer (Malvern-Panalytical), using a Rh Anode as X-ray source. The spectrometer was calibrated with a set of standard materials (Omnian, Malvern-Panalytical).

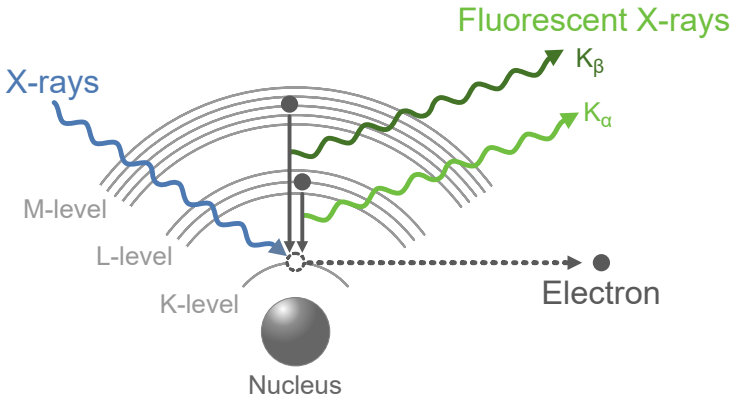

Figure 3.2: *Simplified mechanism of X-ray fluorescence: An incident X-ray ejects an electron (here from the K-level), followed by replacement of an outer-shell electron that emits characteristic fluorescence X-rays.*

3.3.2 Nitrogen physisorption

The physisorption of nitrogen (N_2) at -196 °C is a widely used analysis technique to determine the surface area of solid samples. The essential components of a catalyst are the active sites, which are usually dispersed on the high-surface area support, and it is generally desirable to maximize the number of active sites per volume. Nitrogen is commonly used as a gaseous adsorbate based on the weak interaction with solid surfaces and availability in high purity [78]. The specific surface area (SSA in $m^2 \cdot g^{-1}$) of the samples can be calculated using the Brunauer, Emmett and Teller (BET) method [79]. The BET theory extends the Langmuir model on monolayer adsorption, correlating the partial pressure of the adsorbate to its adsorbed volume. The BET method is based on several assumptions, expecting the solid surface to have a definite number of adsorption sites, where each site adsorbs only one molecule and is energetically equivalent. The gas molecules can adsorb in multilayers with no adsorbate-adsorbate interaction within the same layer. Each layer follows the Langmuir adsorption isotherm independently, and the heat of adsorption for all layers, beyond the first, is equal to the heat of liquefaction (i.e., physical condensation) [24, 80]. The resulting BET equation is presented in Eq. 3.2.

$$\frac{P}{V(P_0 - P)} = \frac{C - 1}{V_m \cdot C} \cdot \frac{P}{P_0} + \frac{1}{V_m \cdot C} \tag{3.2}$$

with P and P_0 as equilibrium and saturation pressure of the adsorbate, V is the total volume of adsorbed gas and C is the BET constant. At a low relative pressure (around P/P_0<0.25) the behavior follows a linear relationship and the nitrogen volume for monolayer formation (V_m) can be obtained from the slope and intercept of the regression line (cf. Fig. 3.3).

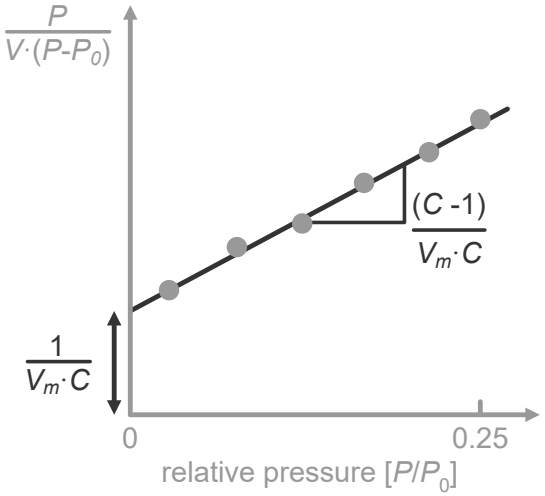

Figure 3.3: *Illustration of the BET theory. The value of the slope and the y-intercept are used to determine the specific surface area (SSA).*

With the given V_m, the SSA can be calculated in $m^2 \cdot g^{-1}$ (Eq. 3.3).

$$\mathrm{SSA} = \frac{V_m \cdot \sigma \cdot N_A}{m \cdot V_{N_2}} \tag{3.3}$$

in which σ represents the occupied area of a single N_2 molecule on the adsorbent, N_A the Avogadro constant, m refers to the mass of the investigated material and V_{N2} as the molar volume of nitrogen under standard conditions. The accuracy of the determined surface area may be affected by insufficient drying and a short equilibrium time at the measurement points. The BET method is only valid in a specific relative pressure range (commonly 0.05-0.25 P/P_0), while outside this range, the model does not accurately represent the experimental data. Due to the assumptions, the BET model may not reliably describe inhomogeneous surfaces. In addition to that, the gas adsorption in micro-pores can result in pore blocking, consequently overestimating the surface area.

In this work (**Paper I–III and V**), the specific surface area (SSA) was determined using a Tristar 3000 instrument (Micromeritics). About 200 mg of sample was used and degassed in nitrogen at 250 °C for 6 h prior to the measurements.

3.3.3 Temperature programmed desorption

Temperature-programmed desorption (TPD) is used to evaluate the quantity and strength of the interaction between the catalyst surface and respective reactants or adsorbates in a controlled temperature setting. Further information such as binding energy, kinetic parameters, or surface coverage can be obtained. The experimental TPD procedure includes a pretreatment step at elevated temperatures and an oxidizing or reducing atmosphere to remove any contaminants or gases on the surface. Then, the probe molecule or adsorbate is introduced at a low temperature until complete saturation of the surface. Following this, any weakly adsorbed molecules are flushed away by an inert gas (typically Ar or N_2). The temperature is then linearly increased with a specific heating rate while constantly monitoring the signal of the desorbing probe molecule (e.g., by a mass spectrometer). As the temperature rises, the adsorbates on different sites desorb from the surface and result in multiple desorption peaks, either sharp or broad, depending on the nature and composition of the adsorption sites [23]. In general, different peaks correspond to different surface sites (Fig. 3.4). Higher peak temperatures indicate a stronger interaction or higher activation energy.

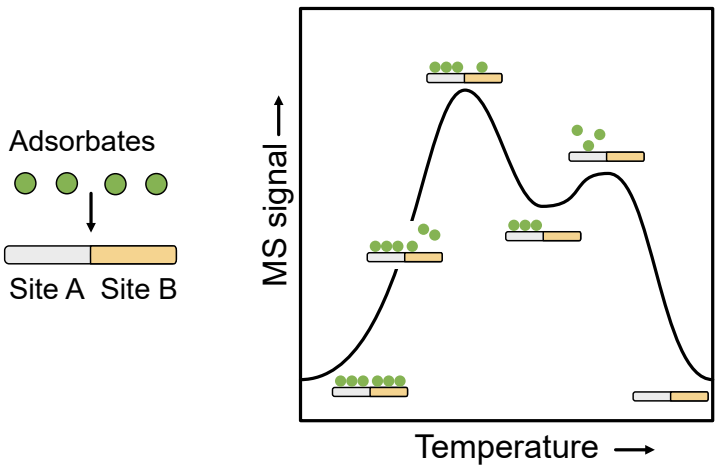

Figure 3.4: *Schematic representation of a temperature programmed desorption experiment. First, the surface is covered with the adsorbate, followed by a temperature increase, while the adsorbates on the different surface sites desorb at different temperatures.*

In this work, the TPD experiments were performed with ammonia (NH_3-TPD) as a probing molecule to investigate the acidity of the samples in **Paper I–III**. About 40 mg of the sample (100-250 µm) was pretreated in 10 % O_2 at 500 °C for 30 min and cooled down to 100 °C in Argon atmosphere. Then, the sample was exposed to 2000 ppm NH_3 at 100 °C,

followed by Ar purging to remove weakly adsorbed ammonia species until the NH_3 signal vanished. The desorption was monitored in the temperature range of 100 to 700 °C at a heating rate of 5 °C per minute. The resulting TPD profiles were baseline subtracted and calibrated to the concentration of the NH_3 signal. The NH_3 uptake (in $\mu mol \cdot g^{-1}$) was determined by integrating the TPD profile and normalized to the used sample mass.

3.3.4 Powder X-ray diffraction

Powder X-ray diffraction (XRD) is a conventional technique to evaluate the crystallinity of a material and provides information about crystalline and amorphous compounds, or the crystal structure. The structure of a crystal can be defined as an ordered arrangement of atoms in the crystal lattice and in a repeating unit. The X-rays that enter a sample are scattered by the electrons in the atoms, and those scattered waves can interfere constructively at certain angles. The X-ray wavelength (λ) is directly related to the spacing (d) between diffracting planes, as defined in Bragg's law ($n \cdot \lambda = 2d \cdot \sin\theta$), with n as an integer [81]. A schematic representation is shown in Figure 3.5.

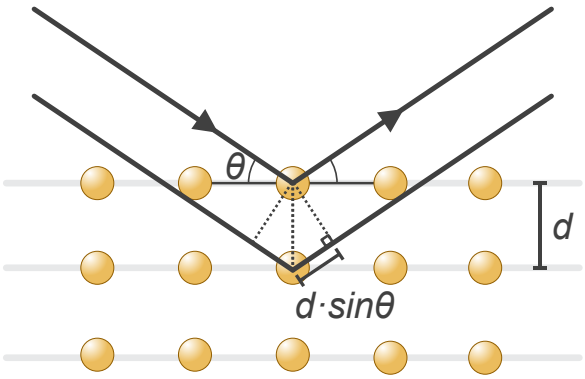

Figure 3.5: *Schematic representation of Bragg's law with the reflection of X-rays by crystal planes. The distance (d) of the planes can be determined with the known X-ray wavelength (λ) and angle (θ).*

By scanning across a range of incident angles, the constructive diffraction occurs from planes that are oriented at the correct angle to fulfill the Bragg's Law [82], resulting in a XRD diffractogram (or XRD pattern), with the intensity of the diffraction X-rays versus the angle between the incident and diffracted X-rays (2θ). Each material has a characteristic set of XRD patterns that can be compared with standard crystallographic databases for a qualitative analysis. Sharp and distinct signals indicate large crystals,

whereas broad peaks suggest the presence of smaller crystallites. The relation is expressed by the Scherrer equation (Eq. 3.4), which can be used to determine crystallite size (τ in Å) from a measured diffraction peak profile [83]. The value of τ represents the diameter of crystallites, which is expressed by X-ray wavelength (λ), full width at half maximum (FWHM) of the peak (β), and the Bragg angle θ. K is a dimensionless shape factor and depends on the geometry of the crystallite, with a typical value of 0.9 resembling nearly spherical particles.

$$\tau = \frac{K \cdot \lambda}{\beta \cdot cos\theta} \tag{3.4}$$

The samples in **Paper I–III** were analyzed by XRD to validate the formation of crystalline particles before and after the aging procedure. In addition, the crystallite size of TiO_2-anatase was determined for the signal at $2\theta = 25°$, to investigate the impact of thermal aging on the TiO_2 support. The XRD diffractograms were collected with an AXS D8 instrument (Bruker) equipped with a Cu-K_α radiation source (0.15406 nm) operating at 40 kV and 40 mA. The samples were mounted in a hollow puck holder with Si-Kapton© tape to avoid sample spreading. For the measurement, the sample was not rotated and measured in fixed-area mode with a length of 5 mm.

3.4 Spectroscopic techniques

In the field of surface science and catalysis, infrared (IR) spectroscopy is a well-established method to probe compounds in their solid, liquid, or gaseous state. When a molecule absorbs infrared radiation, the energy excites vibrational (or rotational) modes. Under the condition that diple moment changes during the vibration, an infrared spectrum can be recorded. If the vibration does not result in a change of the dipole moment, as in a linear, diatomic molecule (e.g., N_2, O_2), it is not IR active. When infrared radiation interacts with matter, it can be transmitted, reflected, scattered (diffuse reflected), or absorbed (Fig. 3.6). Various types of vibrations and rotations are defined by definite ranges of frequencies within the infrared spectrum. The frequency of the vibration depends on the mass of the respective atoms involved in the chemical bond. As a result, chemical bonds, functional groups, or molecular species can be distinguished in an IR spectrum, with subtle changes that can also depend on their adjacent environment. [84, 85].

The assignment of infrared bands requires a proper knowledge of the vibrational modes. For an isolated non-linear molecule with N atoms, there are typically 3N-6 normal vibration modes (3N-5 for linear molecules). The

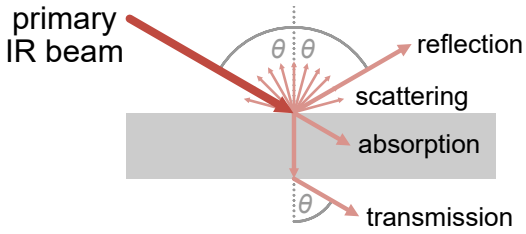

Figure 3.6: *Schematic representation of infrared light interacting with matter.*

modes correspond to the three degrees of freedom including translation, rotation, and vibration. For example, ammonia has six (3·4-6) vibrational modes that correspond to symmetric and anti-symmetric stretching as well as bending modes (Figure 3.7).

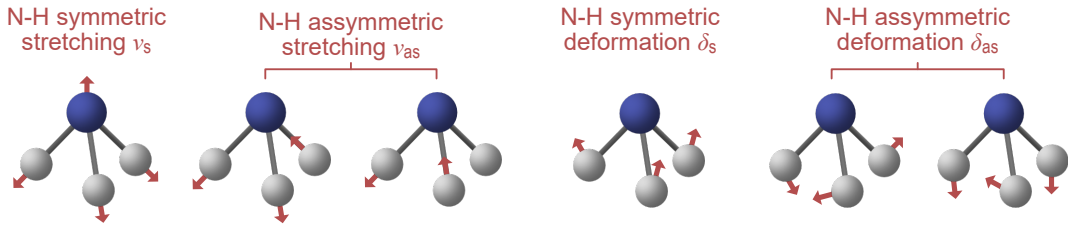

Figure 3.7: *Vibrational modes of isolated ammonia.*

3.4.1 Diffuse Reflectance Infrared Fourier Transform Spectroscopy

Diffuse reflectance infrared Fourier transform spectroscopy (DRIFTS) is a commonly used method in the field of heterogeneous catalysis. In general, this technique is relatively simple thanks to minimal sample preparation, which includes sieving the powder sample to an appropriate particle size (40-80 µm in this work), and enables rapid collection of spectra across a wide span of wavenumbers [86]. This technique allows the detection of surface changes upon the adsorption, desorption, or reaction of species by the vibrations of their functional groups. Further, minor species or intermediates adsorbed on the surface of the catalyst can be identified under the condition of a detectable intensity. A simplified illustration of the DRIFTS setup used in this work is shown in Figure 3.8.

In **Paper I–IV**, *in situ* DRIFTS was operated with a Vertex 70 or 80v (Bruker) spectrometer equipped with a high-temperature reaction cell (Harrick Scientific) and CaF_2 windows. The inlet gas flow was controlled by mass flow controllers (Bronkhorst). The temperature of the sample bed was measured with a thermocouple, inserted through the exhaust pipe and placed right below the sample surface. This was done due to the

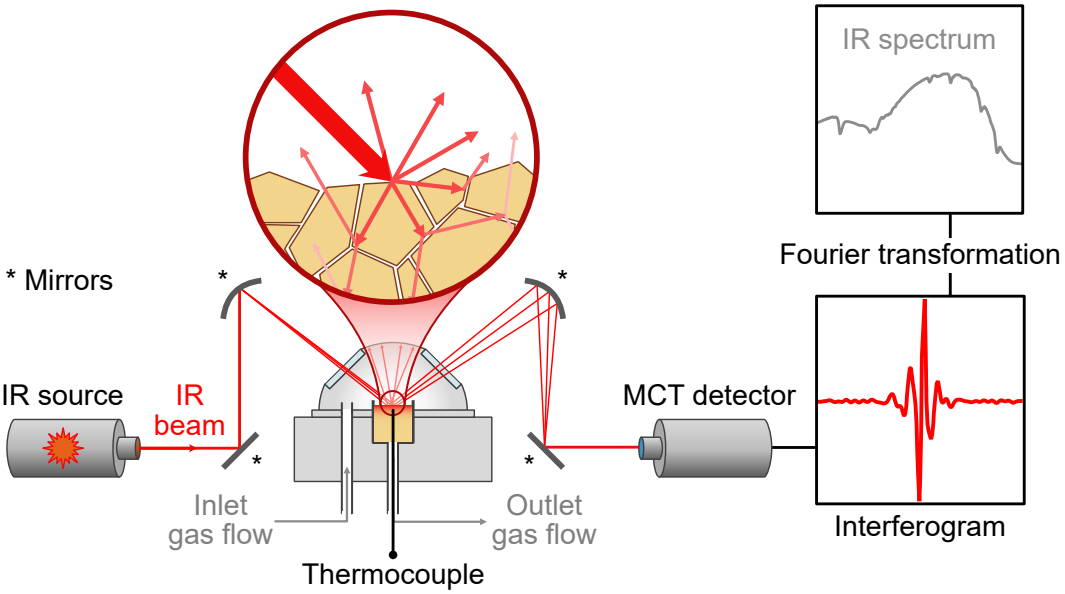

Figure 3.8: *Schematic illustration of the in situ diffuse reflectance infrared Fourier transformation setup in this work: The IR beam is directed via mirrors onto the sample. The diffuse reflected radiation is collected and guided to the detector. The resulting interferogram is Fourier-transformed to obtain the IR spectrum. The inlet gas flow and temperature can be controlled as preferred.*

temperature discrepancy between the sample bed and the set temperature of the Harrick cell [87]. Unless otherwise stated, the reported temperatures of the *in situ* spectra are referred to the sample bed temperature [88]. In **Paper IV**, water vapor was provided with a portable water reactor, fed with hydrogen and oxygen gas, allowing low concentrations of water in high purity [89]. Modulated infrared radiation is induced by passing a broadband light beam through a Michelson interferometer (not shown in Figure 3.8), which splits, reflects, and combines the waves so that the combined light produces an interference pattern. This pattern depends on the difference in the distances that the two waves traveled [90, 91]. The IR beam is directed onto the powder sample, and upon interaction with the rough surface of the sample, the incident radiation undergoes scattering (which is limited by the penetration depth), and is reflected in a diffuse manner across a range of multiple angles [92]. The reflected radiation is then collected and directed towards the MCT detector (Mercury-Cadmium-Telluride). The conductivity of the MCT-material is altered by the IR photons, and the signal is measured as a change in current. To reduce thermal noise, the implementation of a MCT detector requires cryogenic cooling with liquid nitrogen [93]. The collected and resulting raw data is called an interferogram, with the signal intensity versus

optical path difference, measured as the moving mirror in a Michelson interferometer changes position. It contains all the frequency information of the infrared radiation absorbed or emitted by the sample. With the Fourier transformation, the spectral raw data is converted to an IR spectrum with intensity versus wavenumber.

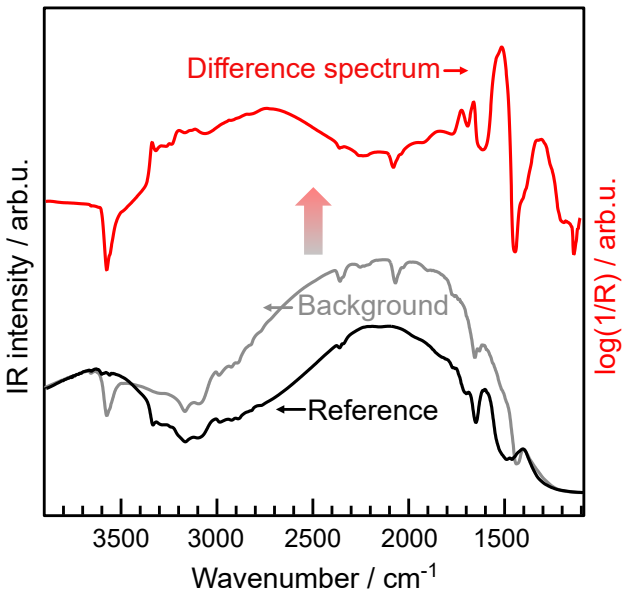

Figure 3.9: *Example of a difference DRIFT spectrum for the ammonia adsorption on a VO_x/TiO_2 catalyst. First, the background spectrum (grey) is recorded after a pretreatment step. Upon ammonia adsorption, the reference spectrum (black) is recorded and subsequently subtracted from the background to obtain the difference spectrum (red).*

The adsorption experiments were used for the qualitative investigation of the surface and identification of formed species on the investigated samples by recording difference spectra. An example of such a spectrum is shown in Figure 3.9, illustrating the adsorption of ammonia on a titania-supported vanadium oxide catalyst. The first step contains a pretreatment procedure, at elevated temperatures and an oxidizing atmosphere, to remove water and any other contaminants, followed by recording the background spectrum (Bkg). Upon adsorption of the respective probe, the reference spectrum (Ref) was recorded and subtracted with the background [-log(Ref)-log(Bkg)], resulting in the difference spectrum. The removal of the baseline contribution simplifies the interpretation. However, a drawback with this approach is a potential baseline drift due to water vapor or atmospheric fluctuations in the cell, and the loss of absolute identity of species. Any quantitative analysis of such spectra would require specific preparation and efforts, since the IR intensity generally does not directly correlate to the concentration of adsorbed species [94].

3.4.2 Raman spectroscopy

Raman and infrared spectroscopy are complementary techniques. Some vibrational modes can be observed by Raman spectroscopy, but cannot be probed by infrared spectroscopy, and *vice versa* [85]. While infrared spectroscopy relies on a change in a molecule's dipole moment, Raman spectroscopy is based on a change in the polarizability during the vibration. The illumination with a high-intensity laser, ranging from ultraviolet to near-infrared light, results in scattering of the light. Most of the light is elastically scattered, retaining the same energy as the incident light (Rayleigh scattering). A much smaller fraction of light is scattered inelastically (Raman scattering), either losing or gaining energy, depending on the vibrational state (Stokes, anti-Stokes). With the use of a monochromatic laser, the frequency shift between the incident light and the Raman scattered light can be determined (also called Raman shift) [95].

In this work, the samples were investigated in terms of the existence of the distinct VO_x species (monomeric, polymeric, crystalline V_2O_5) and alterations after the aging procedure. *Ex situ* Raman spectroscopy was performed in **Paper I-III**, with an InVia Reflex spectrometer (Renishaw) using a 532 nm wavelength diode laser as excitation source. The spectra were recorded on selected surface spots on the powder samples under ambient conditions. A moderate laser power (0.6 mW) was chosen to prevent local heating, hence the dehydration of the VO_x particles. Optical images of the selected spots were inspected before and after the spectra collection to verify that no damage occurred from the laser illumination. The resulting Raman spectra were baseline subtracted and normalized to the peak intensity of the feature at 639 cm^{-1}, associated to the anatase phase of titania. *In situ* Raman measurements (**Paper V**) were performed with a SPEX 1403 Monochromator (Horiba) and a 491 nm DPSS (Cobolt) laser in an oxygen (20% O_2/He) atmosphere. The samples (∼140 mg) were pressed into pellets and mounted on the sample holder of a homemade optical Raman cell [96]. Recording of the spectra under dehydrated feed conditions started at 430 °C, followed by subsequent cooling to lower temperatures (250, 175, and 120 °C) under the continuous flow of 20% O_2/He. The spectra were collected after one hour of sample treatment at each temperature and were normalized as described in more detail in Ref. [97].

3.4.3 Peak profiles and decomposition

Infrared spectra may contain non-symmetrical vibrational bands, variation of the band positions, or bandwidths, which are related to the presence of more than one component resulting in a series of overlapping bands as a total spectrum [98]. Since each vibrating molecule is affected by its surrounding environment (e.g., different adsorption sites or interaction with other molecules), it leads to slight variations in the vibration frequencies. Further, the vibrations of different compounds can be located within a narrow frequency range, which complicates a correct assignment.

Peak decomposition by curve fitting is a valuable method in order to obtain additional information from the spectra, considering the spectrum as a sum of individual peak profiles (Fig. 3.10a). The choice of peak profiles is of importance since the natural relaxation and instrumental broadening must be considered. For solids, a low molecular movement is expected so that the statistical distribution of vibrations results in a Gaussian profile with a symmetric "bell curve" shape and relatively narrow wings. For gases, the fast movement and frequent collisions, as well as rotations, follow a distribution with broad wings as in a Lorentzian profile. A Voigt profile is the convolution of a Gaussian and Lorentzian profile (Fig. 3.10b) and is usually considered for compounds in a liquid state [99].

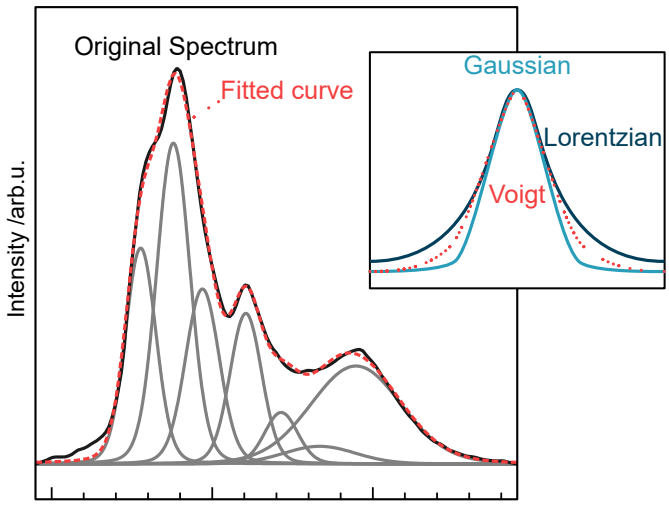

Figure 3.10: *a) Example of a peak-fitted spectrum and b) illustration of a Gaussian and Lorentzian profile with the same peak height. The Voigt profile is their convolution.*

In this work, peak decomposition was done in order to evaluate the contribution of respective species/bands as well as to observe trends or alterations throughout the sample series before and after thermal aging. The NO adsorption spectra were fitted in **Paper I–III**, using the IGOR Pro

8 (WaveMetrics) software. The adsorbed species are neither a gas, solid, nor liquid. Therefore, the spectra were fitted by Voigt profiles, as to include both a Gaussian and Lorentzian character. A shape parameter, which is defined as the ratio of Lorentzian and Gaussian widths ($\sqrt{ln2}\cdot \mathrm{W}_L/\mathrm{W}_G$), with a value of 0.1 was used. Prior to fitting the experimental data in **Paper I-III**, a linear spline was fitted to the spectra and subtracted. The number of peaks and their respective positions were verified based on the time-resolved spectra. For fitting the series of spectra, the positions of peaks are usually fixed with a constraint $\pm 1\,\mathrm{cm}^{-1}$, while the intensity was set free to vary. The *in situ* Raman spectra in **Paper V**, were fitted with the in-built function of the OriginPro© (OriginLab) software. Prior fitting, each spectrum was subtracted with the spectrum of the bare TiO_2 support at the respective temperatures. The spectra were fitted with Gauss profiles, in which the width of each band was fixed, while the position was fixed with a constraint of ± 1 cm^{-1}. Further details of the fitting procedure are described in Ref. [97].

Through integration of the fitted peaks and normalizing to the total peak area, a comparison of proportions of the different species for each sample can be made.

4 Results and Discussion

4.1 Investigation of VO_x/TiO_2 reference catalysts

The vanadium loading is an important parameter for titania-supported vanadium oxide catalysts (VO_x/TiO_2) in terms of both activity and stability, due to the presence of different VO_x species on the surface. Monomeric VO_x species are expected to be predominant below a loading of 1.5 wt% while crystalline V_2O_5 forms at loadings higher than 4 wt%. Present industrial V-based catalysts contain around 2 wt% vanadium as a compromise between activity and stability at higher temperatures, while also containing a high ratio of polymeric VO_x. In **Paper I**, a series of VO_x/TiO_2 model catalysts with five different vanadium loadings was prepared (0.5, 1.5, 2.0, 4.0, and 8.0 wt%) to investigate the effect of loading on the catalytic performance and stability before and after thermal aging. Accordingly, this series is expected to include the entire range of VO_x species, with only monomeric VO_x at a loading of 0.5 wt% and mainly crystalline V_2O_5 species at 8 wt%. The two samples with a loading of 1.5 and 4 wt% represent transition zones, with multiple VO_x species being present.

4.1.1 Catalytic performance and thermal stability as a function of vanadium loading

The catalytic activity of the VO_x/TiO_2 catalysts was evaluated under operation of the standard SCR reaction, testing the NO_x conversion in a temperature range from 175 to 450 °C (Fig. 4.1a-b). The results from the vanadium loading series in fresh state show that a high vanadium loading is advantageous to achieve high NO_x conversions at lower temperatures. On the other hand, catalysts with a low loading benefit the long-term stability, as they maintain catalytic activity after aging.

As an example, the catalyst with a loading of 1.5 wt% shows a low to moderate NO_x conversion up to 300 °C (≤46%), which steadily increases with temperature, reaching 92% at 450 °C. Notably, after the aging procedure, the NO_x conversion is enhanced at low to mid-temperatures (≤350 °C) and reaches a maximum of 86% at 350 °C. In addition to that, the 1.5V catalyst represents the best catalytic activity among all aged catalysts. The NO_x conversion over the fresh 8V catalyst achieves moderate conversions starting from lower temperatures and reaching the overall highest observed NO_x conversion of 99% at 350 °C. However, with increasing temperatures, the performance reduces significantly, which is likely attributed to the partial oxidation of NH_3 to NO_x [100]. After the aging procedure, the overall catalytic activity is substantially reduced with a maximum NO_x conversion of 50%. The overall lower NO_x conversion, observed for the aged catalysts, may also be related to sintering processes of the VO_x particles, forming less active species together with V_2O_5 particles, decreasing the number of accessible sites (vanadium atoms in "bulk").
The formation of nitrous oxide (N_2O) is an important indicator for the reaction selectivity but also a critical parameter in practice, due to the expected legislative restrictions, as mentioned in the Introduction (Chapter 1). Therefore, the effluent N_2O signal was also monitored during the activity measurements (Fig. 4.1c-d). Over the fresh catalysts N_2O is formed in a minor degree at low- to mid-temperatures (≤4 ppm up to 350 °C). At 450 °C, the N_2O formation increases significantly to 13.2 and 70.6 ppm for the 4V and 8V catalyst, respectively. This suggests that N_2O is prevalently formed over crystalline V_2O_5 or highly polymerized VO_x.

To correlate the observed catalytic performance with the physicochemical properties, the catalysts were further analyzed by N_2 physisorption, temperature-programmed desorption with ammonia (NH_3-TPD), X-ray diffraction (XRD), and Raman spectroscopy.

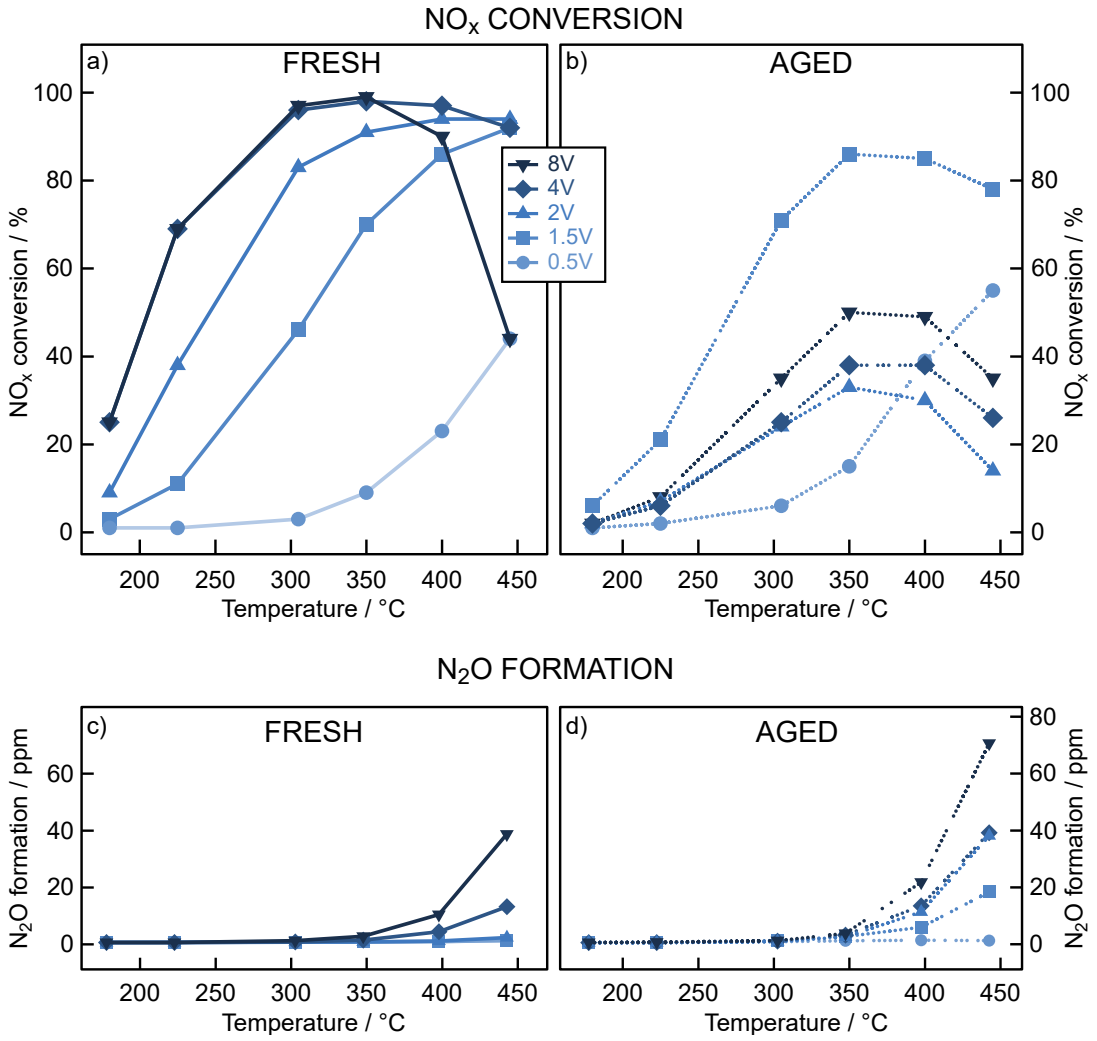

Figure 4.1: *NO_x conversion a-b) and N_2O formation c-d) over the VO_x/TiO_2 catalysts with varying vanadium loading before and after aging. Reaction conditions: 525 ppm NH_3, 500 ppm NO, 300 ppm CO, 3% CO_2, 10% O_2, 5% H_2O in N_2 balance with a GHSV = 60,000 h^{-1}.*

4.1.2 Correlation between catalyst texture and SCR activity

The comparison of specific surface area (SSA) with the crystallite size shows the interrelation of the two parameters (c.f. Fig. 4.2). The bare TiO_2 support exhibits a specific surface area of 88 $m^2 \cdot g^{-1}$, which is reduced by almost a half after the aging procedure (47 $m^2 \cdot g^{-1}$). This loss of surface area is related to the particle growth of TiO_2-anatase [101], which is confirmed by XRD through determination of the crystallite size, which increases by 24% (196 to 257 Å). The addition of a small amount of vanadium oxide (0.5 wt%) has been found to increase the SSA, while higher loadings lead to a

SSA decrease for catalysts in fresh state, presumably due to potential pore blocking. After the aging procedure, the SSA of the catalysts significantly reduces as the loading increases. This significant loss is likely due to the promoting impact of vanadium oxide, which contributes to sintering of the support. Coupled with that, previous studies [102–104] confirmed that vanadium has a catalytic effect on the anatase-to-rutile transformation, starting from 575 °C, and accelerates the decrease of the surface area at high vanadium loadings [61]. The growth in particle size increases with a higher vanadium load.

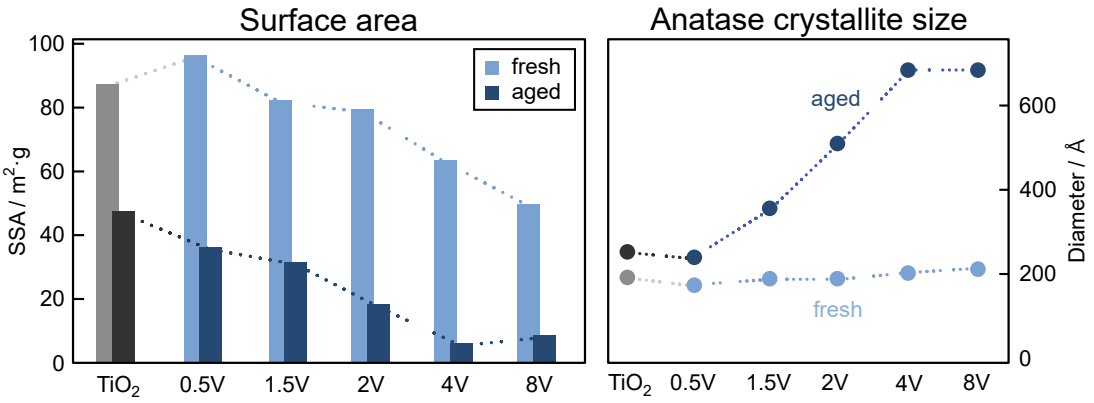

Figure 4.2: *Comparison of specific surface area (SSA) (left) and TiO_2-anatase crystallite size (right) for the TiO_2 support as well as VO_x/TiO_2 catalysts before and after aging. The crystallite size was determined by the Scherrer equation for the signal at $\theta = 25°$.*

In order to gain further insight into the interaction of the catalysts with ammonia, a key reactant in the SCR reaction, temperature-programmed desorption (TPD) experiments with NH_3 were carried out (Fig. 4.3a). The TPD profile of the TiO_2 support shows a broad desorption peak that begins with a sharp increase around 150 °C and extends to 390 °C, followed by a tail to 550 °C. With lower loadings of vanadium (≤2 wt%), the TPD profiles show features similar to those of the bare support. Notably, the desorption peak around 390 °C decreases with increasing vanadium loading, indicating a weaker interaction of ammonia with the vanadium oxides. At a higher loading (>4 wt%), only one main desorption peak at lower temperatures (∼250 °C) is present. While it is likely that these broad profiles originate from different acid sites (i.e., Lewis, Brønsted), a clear assignment remains difficult, as those peaks are also present on the bare TiO_2 support.

Alternatively, the integration of the TPD profiles and determination of the NH_3 uptake (in $\mu mol \cdot g^{-1}$) allows a comparison of the overall acidity for

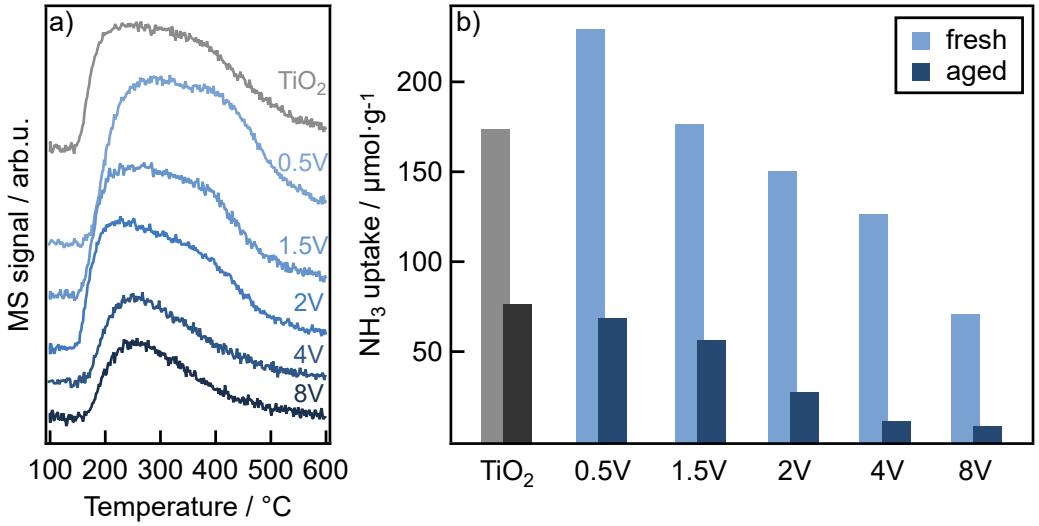

Figure 4.3: *a) NH_3-TPD profiles and b) determined NH_3 uptake of the VO_x/TiO_2 catalysts and TiO_2 support before and after aging.*

the samples (Fig. 4.3b). The observed trends of the NH_3 uptake before and after aging correlate with the results from the surface area (SSA). The TiO_2 support loses more than half of its NH_3 uptake capacity after the aging procedure (175 to 78 µmol·g^{-1}, -56%). A low amount of vanadium in fresh state (0.5V) results in a higher uptake of 231 µmol·g^{-1}, presumably due to the higher surface area or formation of V-O-Ti bonds that have a higher acidity. With the introduction of more vanadium, the NH_3 uptake gradually decreases, which is in accordance with previous studies [39, 105, 106] given that the NH_3 adsorption energy is lower for vanadium than for TiO_2 [106, 107]. After aging, the NH_3 uptake significantly decreases for all catalysts. The correlation of specific surface area together with NH_3 uptake suggests that both parameters are primarily directed by the support, or influenced by the degree of exposed titania. Yet, in relation to the activity, both parameters appear not to be the limiting parameters for the SCR reaction (under steady state conditions). For example, the aged 1.5V catalyst achieves an increased NO_x conversion compared to the fresh state, despite significant losses of SSA and NH_3 uptake.

X-ray diffraction and Raman spectroscopy provide information about respective alterations of the vanadium oxide particles as well as potential formation of crystallites. In fresh state, all catalysts show broad XRD patterns of the anatase phase of TiO_2, indicating that the VO_x species are highly dispersed in a rather amorphous state on the surface (Fig. 4.4a). For a loading of 8 wt%, signatures of crystalline V_2O_5 are detected. After the aging procedure, the signatures of TiO_2-anatase sharpen, indicating a higher crystallinity resulting from the growth in particle size. The catalysts

with a high loading, starting from 4 wt%, show characteristic signatures of crystalline V_2O_5 and rutile TiO_2.

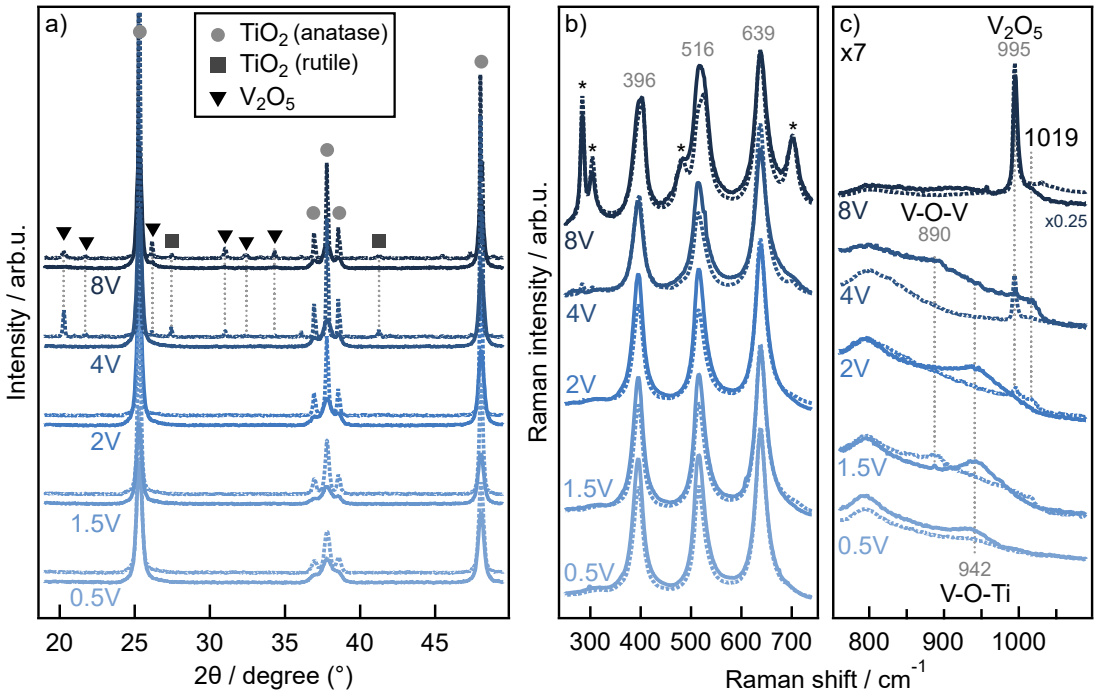

Figure 4.4: *a) Background-subtracted X-ray patterns and b) normalized Raman spectra of the fresh (solid line) and aged (dashed line) VO_x/TiO_2 catalysts recorded under ambient conditions. The Raman spectra are shown after normalization to the intensity of the mode at 639 cm^{-1} and the * symbols mark additional V_2O_5 features. c) displays the V=O vibration area, which is magnified by a factor of 7, and the intensity of 8V was adjusted by a factor of 0.25 for better visibility.*

The Raman spectra of the bare TiO_2 support and the VO_x/TiO_2 catalysts, recorded at ambient conditions, are shown in Fig. 4.4b-c. The Raman spectrum of the bare TiO_2 support reveals three Raman active modes in the region of 300–700 cm^{-1} that are related to the anatase phase of TiO_2. The region around 800–1100 cm^{-1} displays the V=O vibration area (Fig. 4.4c). Vibrational modes at 942 cm^{-1} represent V-O-Ti stretching vibrations of monomeric VO_x species [108], while V-O-V vibration modes of polymeric VO_x are located around 890 cm^{-1} [109]. The catalysts with a loading lower than 2 wt% reveal a main feature around 942 cm^{-1} and therefore suggest to contain a high ratio of monomeric VO_x. With a loading of 4wt% and thus reaching the theoretical vanadium monolayer coverage, the vibrational modes of V-O-V and a weak signature of V_2O_5 (995 cm^{-1} [42, 109, 110]) are observed. Further, an additional feature at 1019 cm^{-1} is observed. In dehydrated conditions, vibrational modes around 1030 cm^{-1} have been assigned to isolated or monomeric VO_x

species [42]. Because of the high vanadium loading and the fact that the feature around 1019 cm^{-1} arises also for pure V_2O_5, this band is here proposed to originate from highly polymerized VO_x species. Reaching the highest vanadium loading in this study (8 wt%), mainly crystalline V_2O_5 modes are observed, with an intense and sharp feature at 995 cm^{-1} and additional modes at lower wavenumbers (marked with an *). After aging, the Raman spectra show an intrinsic morphological transition of titania due to changes in the intensity of the respective modes in between 300–700 cm^{-1} [111, 112]. The presence of rutile TiO_2 cannot be excluded, and the detection is challenging since the Raman scattering cross section of rutile is significantly smaller than that of anatase [113]. In addition to that, the characteristic vibrational modes of rutile (expected at around 612 and 480 cm^{-1} [114]) were not observed in the spectrum of the 4V sample, while the presence was confirmed by XRD. In the spectra of the aged VO_x/TiO_2 catalysts, modes related to V-O-V vibrations and a shoulder at 1019 cm^{-1} for a loading starting from 1.5 wt% appear, which indicate the formation of more polymeric VO_x species [115]. Starting from a vanadium loading of 2 wt%, the vibrational modes of V_2O_5 are also observed. Although the XRD gives evidence for the formation of V_2O_5 only at higher loadings ($\geq$4 wt%), Raman spectroscopy reveals the V_2O_5 formation even for the catalysts with a moderate V loading of 2 wt%.

To summarize, it has been shown that a low loading is beneficial for the thermal stability, while a high loading improves the overall activity at lower temperatures. Linking the physicochemical properties with catalytic performance, the observed lower NO_x conversion after thermal aging is related to sintering of the VO_x species to form crystalline V_2O_5, at the expense of decreased number of accessible surface sites. The VO_x species promote the loss of SSA and NH_3 uptake and beyond transformations of the titania support as evidenced by XRD and Raman spectroscopy. When reaching or exceeding the monolayer coverage of the support, the formation of crystalline V_2O_5 cannot be avoided, which is detrimental for the SCR activity and reaction selectivity at higher temperatures. The presence of V_2O_5 correlates with the formation of N_2O. Lastly, the results demonstrate that the SSA and NH_3 uptake should generally not be considered as main design parameters for VO_x/TiO_2 catalysts with respect to the SCR activity (under stationary conditions). In reference to the SCR mechanism (cf. Section 2.3), it appears that the redox properties play a major role in the SCR reaction, especially for the activity at lower temperatures.

4.2 Modification of VO_x/TiO_2 with Ce, Nb, and Sb

With relevance to the challenges in the application for mobile sources, the development of suitable SCR catalysts has focused on improving the catalysts thermal stability without sacrificing the SCR performance by modification of the VO_x/TiO_2 system with other metal oxides. In **Paper II** and **III**, the VO_x/TiO_2 catalysts were modified with either cerium oxide, niobium oxide, or antimony oxide, and the effect of thermal aging was investigated. In addition to that, samples labeled as 'modified support' were prepared to study the impact of the modifier on the support. The respective loading was chosen to obtain a near equimolar ratio of vanadium and the respective modifier. The prepared samples were investigated *via* X-ray fluorescence (XRF)to confirm that the target loading of the respective compounds has been achieved. The vanadium loading was 2.1–2.2 wt%, with either 4.6 wt% cerium, 3.6 wt% niobium, or 4.7 wt% antimony. The modified samples were compared to the bare TiO_2 support and an unmodified VO_x/TiO_2 catalysts containing an equal vanadium loading (2.2 wt%) as references.

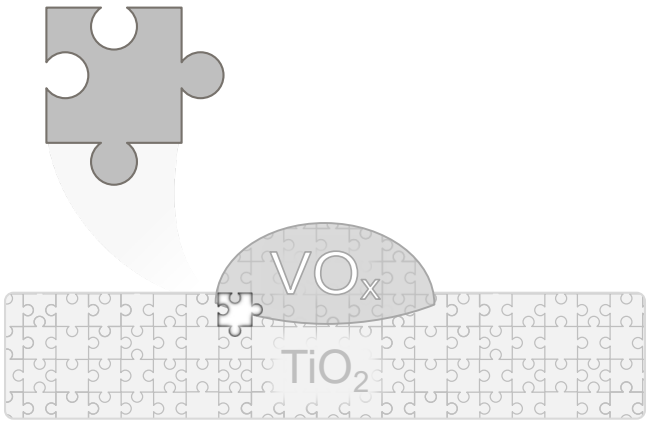

4.2.1 Catalyst performance and stability

The NO_x conversion over the modified VO_x/TiO_2 catalysts as well as the unmodified reference (V/Ti) in the temperature range from 175 to 450 °C is shown in Fig. 4.5. In the fresh state, the addition of the modifiers resulted in NO_x conversion values that are similar to the reference, with a slight advantage at low- to mid-temperatures (≤300 °C). The enhanced activity of the Ce-modified catalyst (V-Ce/Ti) can be attributed to the inherent redox capability of ceria [116], as the modified support (Ce/Ti) proved a particular SCR activity with 54% conversion at 450 °C. The antimony oxide species also proved to be SCR active (49%), while niobium oxide is rather inactive (8%). At high temperatures (≥400 °C), the unmodified catalyst shows the overall best performance (94%) among the tested catalysts.

After the aging procedure, some significant changes in the NO_x conversion among the different samples can be observed. While V/Ti exhibits a considerable drop in the catalytic performance, the modified catalysts maintained high to moderate NO_x conversions. However, the Ce-modified catalyst (V-Ce/Ti) indicates to be more adversely affected, particularly at lower temperatures. On the other hand, the V-Nb/Ti catalyst favors the preservation of the overall activity after aging, showing similar conversions up to 300 °C compared to that in fresh state and just a slight decline at higher temperatures. Notably, the aged catalyst modified with antimony oxide (V-Sb/Ti) shows a remarkably improved performance over all tested temperatures.

Normalizing the NO_x conversion by the vanadium loading offers a different perspective to evaluate the effect of the modifiers on the catalytic performance (Fig. 4.6). The specific rate (in converted mol NO per gram vanadium) determined at a low (225 °C) and high temperature (300 °C), further confirms the previous observations. In comparison with the reference catalyst, the implementation of cerium oxide and niobium oxide in fresh state reveals a higher activity at lower temperatures, while degrading after thermal stress. After aging the modification with niobium oxide also especially demonstrates a preserved activity. The aged antimony-modified catalysts exhibit the overall best performance at both temperatures.

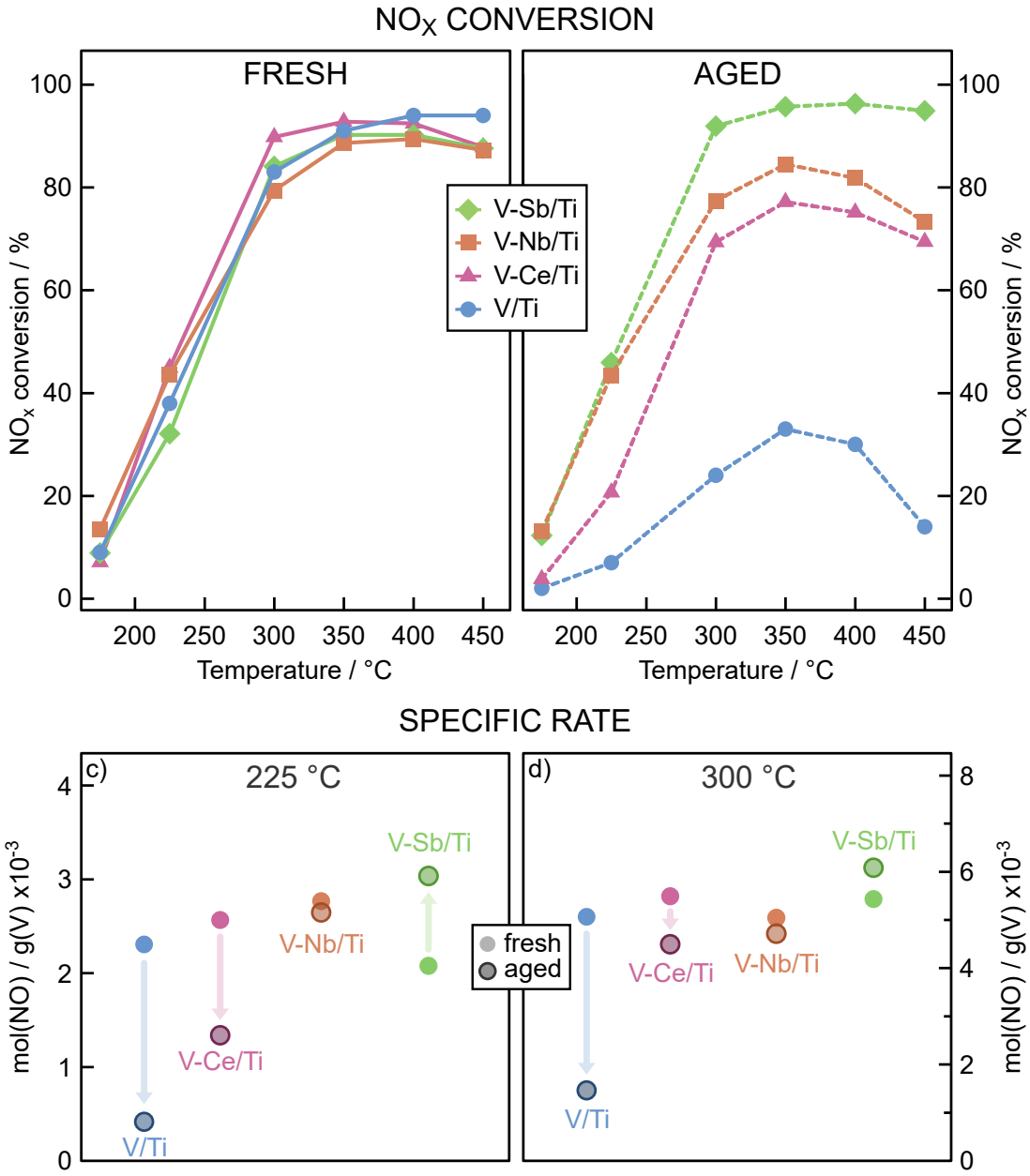

Figure 4.5: *a-b) NO_x conversion and c-d) specific rate of the modified VO_x/TiO_2 catalysts with the reference before and after aging. Reaction conditions: 525 ppm NH_3, 500 ppm NO, 300 ppm CO, 3% CO_2, 10% O_2, 5% H_2O in N_2 balance with a GHSV = 60,000 h^{-1}.*

With respect to the formation of nitrous oxide (N_2O), all modified catalysts suppress the formation of N_2O, especially at higher temperatures compared to the reference (V/Ti). In fresh state, concentrations of less than 2 ppm ($\leq$300 °C) and at most 3.4 ppm at 450 °C were measured (4.5 c,d). Only V-Ce/TiO_2 reveals a slightly higher N_2O formation of 2.7 ppm at 300 °C, increasing to 5.2 ppm at 450 °C. After the aging procedure, the

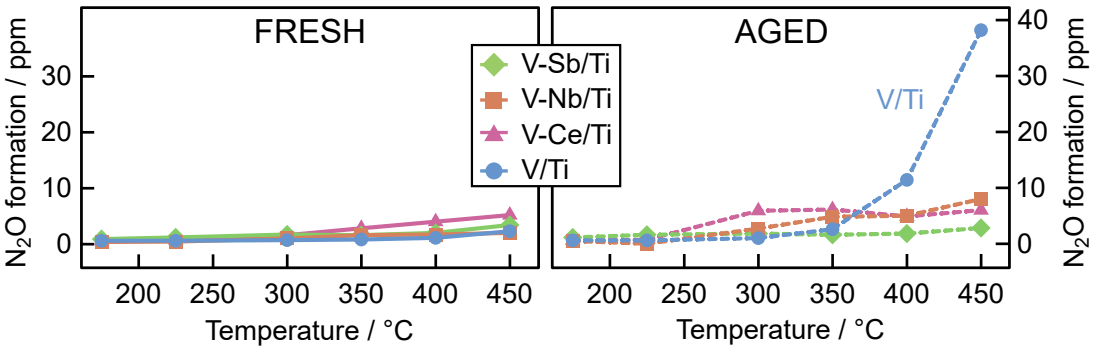

Figure 4.6: *N_2O formation over the modified VO_x/TiO_2 catalysts with the reference before and after aging.*

N_2O formation over V-Ce/Ti and V-Nb/Ti increases for mid-temperatures (300-350 °C), reaching a maximum of 6 ppm (V-Ce/TiO_2) and 8 ppm (V-Nb/TiO_2) at 450 °C, respectively. Notably, the Sb-modified catalyst reveals the overall lowest N_2O formation (3.4 ppm at 450 °C).

4.2.2 Impact of the modifiers on the catalyst texture

The specific surface area (SSA) of modified samples as well as the references before and after aging are displayed in Fig. 4.7. The implementation of the modifiers demonstrated a notable preservation of the surface area after the aging procedure. In comparison to the fresh support (TiO_2), the addition of niobium oxide resulted in a slightly higher SSA, which could relate to the three-dimensional growth of the Nb-species even before reaching monolayer coverage [113]. When cerium oxide or antimony oxide was added, the determined SSA was lower than the reference. After the aging procedure, Sb/Ti proved a significant stabilization effect by only a marginal loss of 5% of its initial surface area. The SSA of Nb/Ti decreased by 26% followed by 29% for Ce/Ti. The modified catalysts reveal a similar SSA in fresh state. After aging, the SSA of V-Sb/Ti decreased by 3%, demonstrating an exceptional preservation of the SSA, proving a stabilizing effect of antimony oxide on TiO_2 with and without the presence of vanadium oxide. With the addition of niobium oxide, V-Nb/Ti retains about half the original surface area. The addition of cerium oxide stabilizes the TiO_2 support effectively, but does not seem to counteract the TiO_2 particle sintering in presence of VO_x.

The comparison of the determined NH_3 uptake in Fig. 4.8 shows that the promoted supports have a lower NH_3 uptake than the reference catalyst, suggesting that the promoters do not contribute to the overall acidity. While the Ce- and Nb-modified support reveals a rather similar NH_3 uptake in fresh state (168, 191 $\mu mol \cdot g^{-1}$), the NH_3 uptake for the Sb-modified

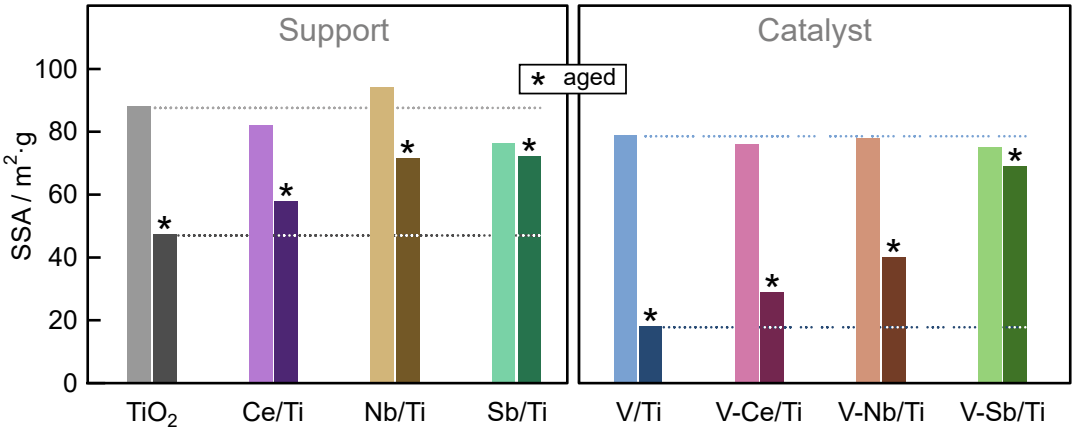

Figure 4.7: *Comparison of specific surface area (SSA) of the modified TiO_2 (left) as well as VO_x/TiO_2 catalysts (right) before and after (*) aging. Dotted lines are inserted to guide the eye.*

support is much lower (80 µmol·g^{-1}). However, after the aging procedure, the uptake for Sb/Ti is increased (+54%). The presence of niobium oxide appears to preserve the surface acidity by a marginal loss (-1%), while with cerium oxide, this effect is more pronounced (-27%).

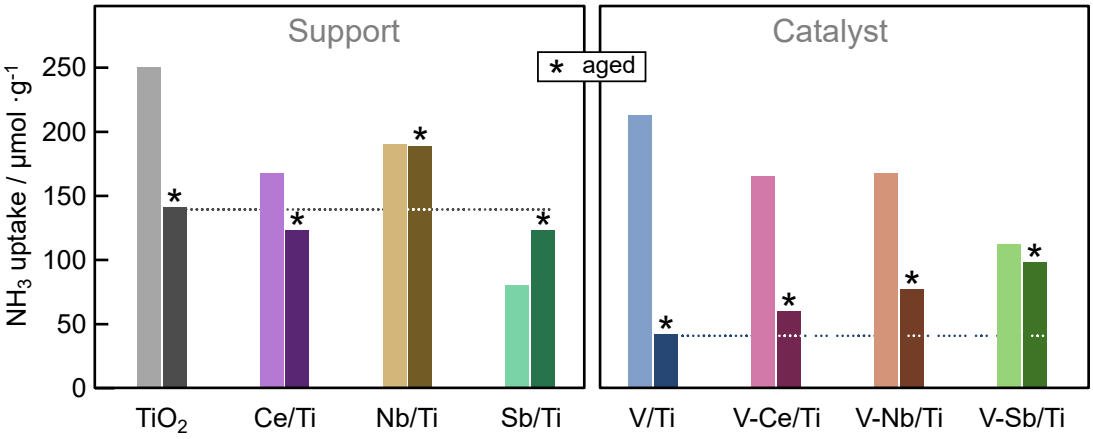

Figure 4.8: *Comparison of determined NH_3 uptake for the modified TiO_2 (left) and VO_x/TiO_2 catalysts (right) before and after (*) aging. Dotted lines are inserted to guide the eye.*

The comparison of the modified VO_x/TiO_2 catalysts with the reference show similar trends. The Sb-modified catalyst (V-Sb/Ti) reveals a much lower uptake than V-Ce/Ti or V-Nb/Ti in their fresh state. After aging, V-Sb/Ti shows a preservation of the NH_3 uptake with a slight decrease of -13% (98 µmol·g^{-1}), while for V-Ce/Ti it decreases by -64% and V-Nb/Ti decreases by -54%. Nevertheless, compared to the reference sample, all modified catalysts demonstrate a higher preservation of the NH_3 uptake

throughout the aging procedure.

The diffractograms and Raman spectra of the modified catalysts and the reference catalyst are shown in Fig. 4.9. The X-ray diffractograms are dominated by features of TiO_2-anatase. In fresh state, no reflections related to vanadium oxide, the modifiers or mixed vanadates (e.g., $CeVO_4$) were observed, suggesting that both the VO_x species and the additives are highly dispersed on the surface. After the aging procedure, reflections related to CeO_2 are seen for V-Ce/Ti, and demonstrate a sintering process of the cerium oxide species. All modified catalysts reveal a maintained intensity of the features, suggesting that no significant changes occurred.

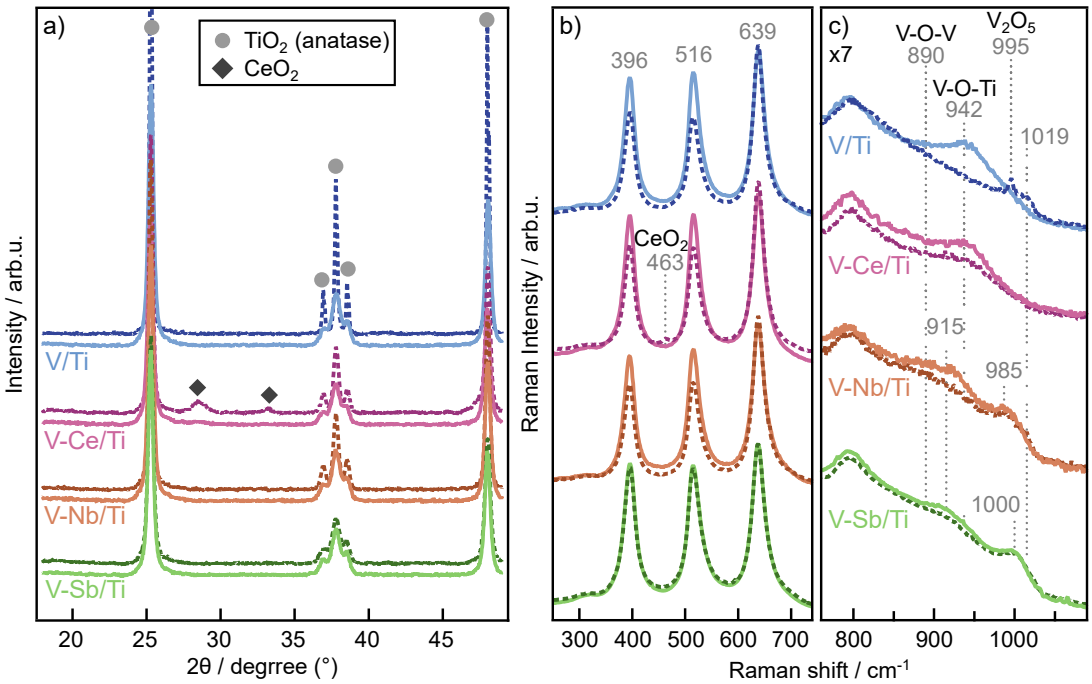

Figure 4.9: *a) Background-subtracted X-ray patterns and b) normalized Raman spectra of the modified VO_x/TiO_2 catalysts before (solid line) and after (dashed line) aging. Raman spectra were measured under ambient conditions (λ = 532 nm) and are here shown after normalization to the peak intensity of the mode at 639 cm^{-1}. c) displays the V=O vibration area, which is magnified by factor of 7.*

The Raman spectrum of the aged reference catalyst (Fig. 4.9c) indicates the formation of V_2O_5 by the feature at 995 cm^{-1} [42, 109, 110]. The shoulder around 1019 cm^{-1} has been discussed in Section 4.1.1, and it is expected to relate to highly polymerized VO_x species, since it was only observed for catalysts with vanadium loadings nearby or above monolayer coverage. The modified catalysts show features that are related to polymeric VO_x species. While the spectrum of V-Ce/Ti exhibits one

main feature around 942 cm^{-1}, the modification with antimony oxide and niobium oxide (V-Nb/Ti, V-Sb/Ti) shows features around 915 and 1000 cm^{-1}, thus representing a higher degree of polymerized VO_x species. After aging, no V_2O_5 was detected on all modified catalysts, and no notable changes in the features in the spectra were observed. In the spectrum of V-Ce/Ti, an additional feature at 463 cm^{-1} is related to CeO_2 [117].

As shown by XRD and Raman spectroscopy, the modifiers stabilize the support by preventing the TiO_2 particle growth and the formation of crystalline V_2O_5 upon aging. The modified catalysts exhibit a high ratio of polymeric VO_x, which is preserved upon thermal stress, and thus facilitate the SCR activity to a greater extent while suppressing the formation of N_2O.

4.2.3 Effect of the modifiers on the dispersed VO_x structure

In **Paper V**, low-loaded samples ($\sim$0.5 V·nm^{-2}) were prepared to investigate the effect of the modifiers on dispersed VO_x species before and after aging. The sample composition was chosen to obtain an equimolar ratio of vanadium (0.35 wt%) and the modifier (0.96 wt% Ce, 0.64 wt% Nb, or 0.84 wt% Sb). Such a loading was chosen to ensure the existence of isolated VO_x sites, thereby enabling the spectroscopic distinction of the structurally different species. Infrared spectroscopic methods, such as *in situ* Raman and FTIR are one of the best suitable techniques to investigate the structure of the VO_x species. A combined Raman-FTIR *in situ* spectroscopic study [97] described structures of three monomeric VO_x species for low coverages ($\leq$0.74 V·nm^{-2}). Species-I is the predominant species, with a mono-oxo distorted tetrahedral configuration. Species-II has a mono-oxo distorted octahedral configuration, and the minority Species-III with a di-oxo configuration (Fig. 4.10). The relative presence of those species was found to be temperature-dependent, leading to reversible structural transformations, where underlying mechanism is the hydrolysis of the V–O–Ti sites [97]. When decreasing the temperature (from 430 to 250 °C), retained water molecules by the surface, mediate transformations from Species-II to Species-I. Further decreasing the temperature (from 250 to 120 °C) leads to the transformation of Species-I to Species-III.

The analysis of the recorded *in situ* Raman spectra as a sequence of decreasing temperature, focuses on the V=O stretching vibrations in the 900–1050 cm^{-1} region. Fig. 4.11 shows the *in situ* Raman spectra obtained for the unmodified V/Ti sample in fresh state and after the

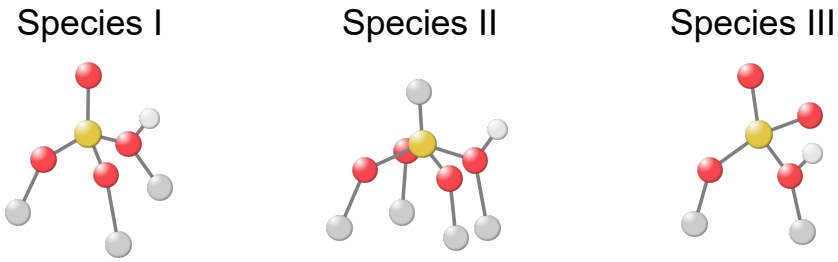

Figure 4.10: *Proposed strucutres of the dispersed VO_x species I–III at a low vanadium loading. Atom colors: gold (V), red (O), grey (Ti), white (H). Adapted from Ref. [97].*

aging procedure. The corresponding spectra obtained for the bare TiO_2 support are shown as a grey background under each spectrum. At 430 °C, the main Raman feature at 1024-1026 cm^{-1} is associated to the majority Species-I, followed by Species-II at ∼1014–1016 cm^{-1} and a third weak feature (Species-III) located at ∼1000 cm^{-1}). The presence of the three species is also confirmed by *in situ* FTIR, recorded in the overtone region (2200-1900 cm^{-1}), providing a separation of the overtone counterparts due to the approximate doubling of the features' distances. The *in situ* Raman spectra recorded after the aging procedure indicate a structural transformation of the dispersed VO_x species. In the spectra series, a broad feature around ∼900-950 cm^{-1} is observed, gaining intensity as the temperature decreases, and correlates to V–O–V modes [42, 109, 110, 118], thus suggest the agglomeration of the dispersed VO_x species to form polymeric or oligomeric VO_x. Under the condition that the specific surface area lowers upon aging, it results in a higher V surface density, thereby accounting for the agglomeration of isolated VO_x units to polymeric VO_x and an increase of the normalized Raman intensities of, e.g., Species-I and Species-II in the aged sample relative to its non-aged counterpart.
A peak analysis procedure was performed to identify the separate contributions to the respective species. Only the spectra recorded at 430 and 250 °C were analyzed, due to the relevance in the NH_3-SCR process and the distortive impact of the broad V-O-V features at lower temperatures. The existence of two bands assigned to Species-III is due to the symmetric (ν_s) and antisymmetric (ν_{as}) vibrations of the di-oxo group. An example of a peak-fitted spectrum is shown in Fig. 4.12 along with the results of the peak analysis, which provides further insight into the effect of thermal aging on the dispersed VO_x phase. By lowering the temperature, the extent of Species-I presence is increased at the expense of Species-II for both fresh and aged samples.

The spectra of the fresh Ce-modified sample (V-Ce/Ti) in Fig. 4.13 show a

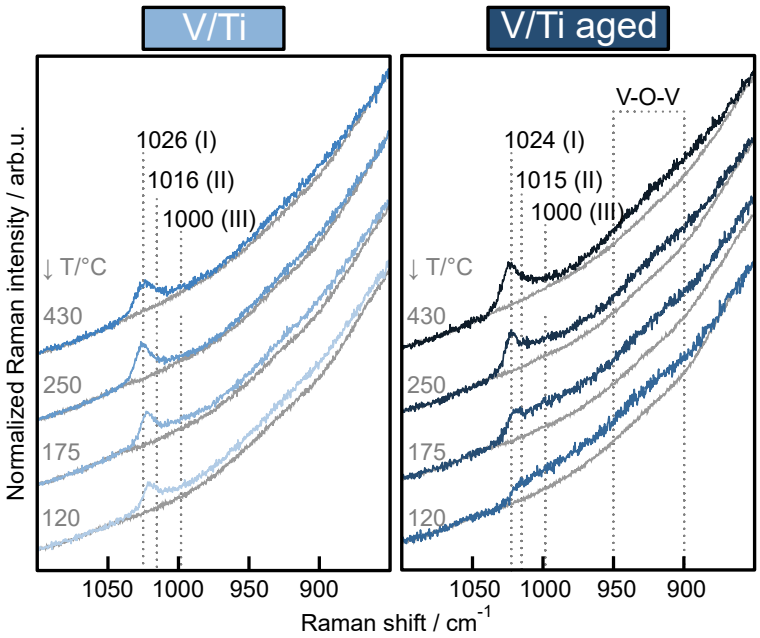

Figure 4.11: *In situ Raman spectra of the unmodified VO_x/TiO_2 before (left) and after (right) the aging procedure. The grey traces represent the TiO_2 spectra.*

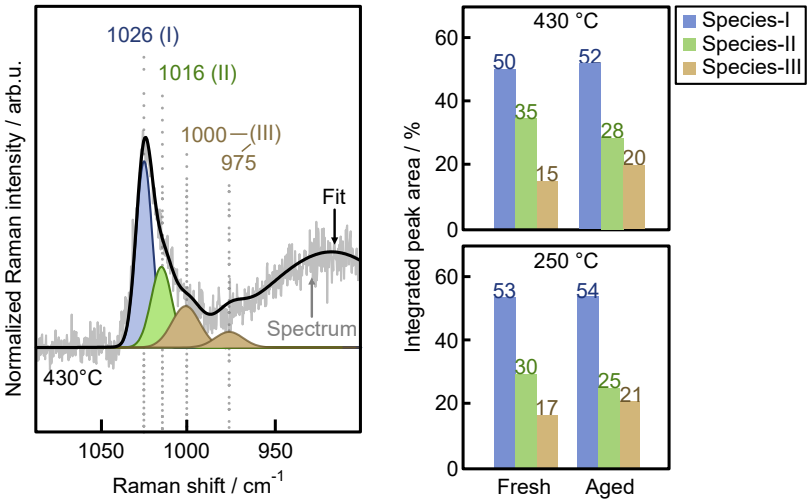

Figure 4.12: *Example of peak-fitted in situ Raman spectrum after subtraction with the corresponding TiO_2 background (left) and proportion of the species at 430 and 250 °C (right)*

slightly increased intensity of the feature at 1025 cm^{-1} (Species-I), compared to the unmodified V/Ti reference, and confirmed by peak analysis. During cooling to 250 °C, the relative distribution of all species remains widely consistent. After thermal aging, the peak analysis shows a limited increase of Species-I over Species-II. These findings imply that thermal aging of the

V-Ce/Ti sample does not significantly affect the temperature-dependent transformation of the dispersed VO_x species.

With the modification with niobium oxide (V-Nb/Ti) or antimony oxide (V-Sb/Ti), the corresponding spectra for the fresh samples exhibit a higher intensity of the feature of Species-I ($\sim$1025 cm^{-1}). The same trend is followed, as demonstrated by the peak analysis, for the proportions of Species-II and Species-III. IN contrast to the V-Ce/Ti sample, the existence of broad features in the 900–950 cm^{-1} region indicates the presence of polymeric V–O–V domains and potential V-O-Sb or V-O-Nb bridging modes [113, 119–121]. As expected, the lower temperature (250 °C) results in a transformation from Species-II to Species-I. After the aging procedure, the resulting spectra exhibit a strong increase in the Species-I/Species-II ratio for both V-Sb/Ti and V-Nb/Ti. Further, a higher intensity of the previously mentioned bridging modes (900-950 cm^{-1}) is observed. The peak analysis confirms the established transformation of Species-I to Species-II.

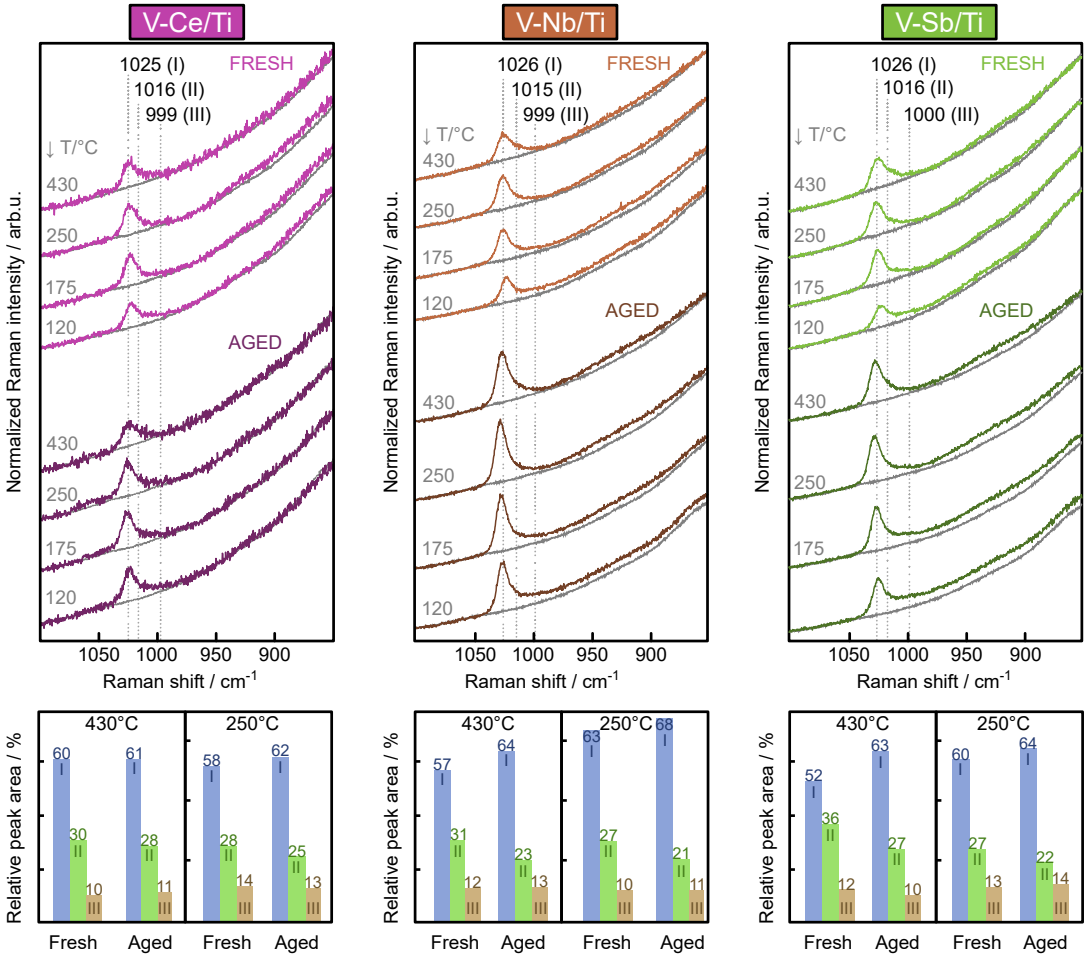

Figure 4.13: *In situ Raman spectra of the modified VO_x/TiO_2 before and after the aging procedure (top). The grey traces represent the TiO_2 spectra. (bottom) Peak analysis of the spectra at 430 and 250 °C (right).*

The comparison of the modified samples suggests that Ce-modification at a low vanadium loading enhances the stabilization of the dispersed VO_x species, while suppressing the agglomeration of vanadium oxides during thermal aging. The modification with both niobium oxide and antimony oxide introduces bridging V-O-M (M = V, Nb, Sb) domains, indicating an interaction of the vanadium and antimony/niobium species, in particular after thermal aging.

4.3 Surface characterization by molecular probe infrared spectroscopy

Catalyst surfaces can be analyzed by infrared spectroscopy using suitable chemical probes, such as IR-active molecules that adsorb on the surface of the samples. Ammonia (NH_3) as well as nitrogen monoxide (NO) are common probe molecules and water is IR-active. As those molecules have a direct relevance to the NH_3-SCR reaction, representing reactants or products, studying the adsorption of these molecules is particularly convenient in this case. The catalyst surfaces were investigated by adsorption of either NH_3, NO, or water after an oxidizing pretreatment step. While the adsorption experiments performed in **Paper I-IV** differ from practical SCR conditions. This approach facilitates a well-defined setting to characterize the surface and to analyze the fundamental adsorption of these gases, minimizing the influence of overlapping signals from other compounds. These insights are essential for the interpretation under more complex conditions.

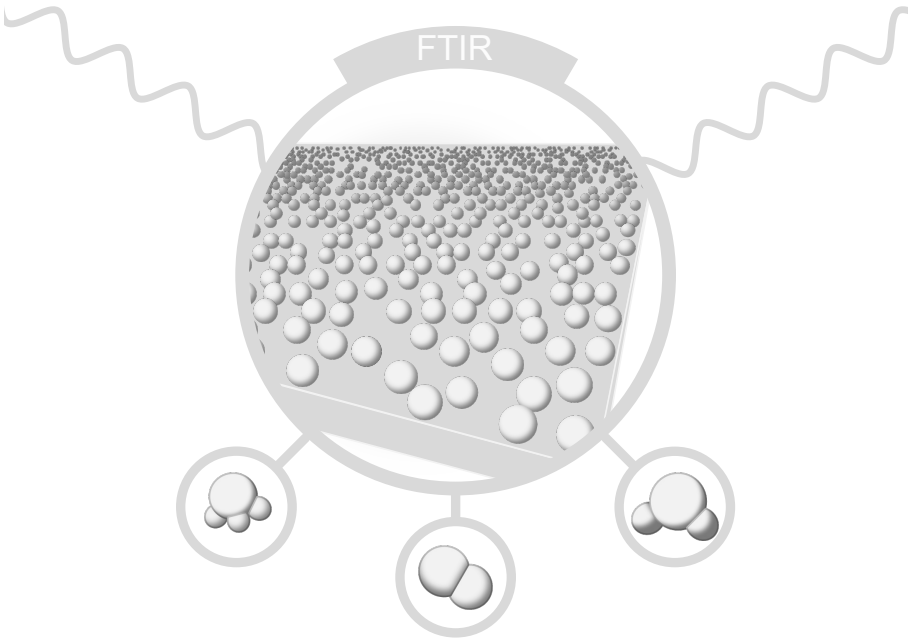

4.3.1 Adsorption of ammonia

The DRIFT spectra of the ammonia adsorption exhibit two vibrational regions of interest. Positive IR bands in the N-H deformation region between 1800 and 1100 cm^{-1} allow the identification of coordinated NH_3 on Lewis acid sites, alongside with NH_4^+ formed on Brønsted acid sites. Due to the self-absorption of the anatase phase of TiO_2, the samples are opaque to the infrared light below wavenumbers of 1000 cm^{-1} [122]. Negative bands appear in the region between 3800 and 3500 cm^{-1} and provide information about suppressed surface hydroxyl (OH) groups as a consequence of the formation of NH_4^+ upon ammonia adsorption.

In **Paper I**, the *in situ* DRIFT adsorption spectra of ammonia on TiO_2 and the VO_x/TiO_2 catalysts were recorded after exposing the samples to 500 ppm of NH_3 for 30 min at room temperature and are displayed in Fig. 4.14. In the OH region on TiO_2, bands of isolated or terminal Ti-OH (3735, 3718 cm^{-1}) and bridged Ti-(OH)-Ti groups (3672, 3642 cm^{-1}) on different surface facets [101, 123] are observed. With the introduction of vanadium (0.5 wt%), the isolated Ti-O-H bands are significantly weaker, indicating that the vanadium oxides preferentially interact with those groups and the main band at 3650 cm^{-1} is related to isolated V-OH groups [30, 124]. When reaching a higher vanadium loading ($\geq$2 wt%), an additional band at 3635 cm^{-1} can be identified and is assigned to bridged V-(OH)-V, following the analogy of the surface hydroxyl groups on titania.
In the N-H deformation region (Fig. 4.14b), the negative band around 1360 cm^{-1} is assigned to asymmetric S=O stretching vibrations of surface sulfates due to the preparation of the TiO_2 support via the sulfate route [125, 126]. While the TiO_2 support mainly exhibits an adsorption band related to Lewis acid sites (1595 cm^{-1}), the VO_x/TiO_2 catalysts additionally reveal bands related to Brønsted acid sites (1480-1430 cm^{-1}). Throughout the sample series, two overlapping bands can be distinguished with positions around 1480–70 cm^{-1} and 1440–1430 cm^{-1}. The latter emerges as the main band as the loading increases. According to the observations in the OH region, these bands are correlated to NH_4^+ that is formed on isolated V-OH, here labeled as "monomeric Brønsted acid site" (1480–1470 cm^{-1}), and bridged V-(OH)-V or V-(OH)-Ti groups as "polymeric Brønsted acid site" (1440–1430 cm^{-1}). In addition, the shift of the Lewis acid site from 1599 cm^{-1} to 1606 cm^{-1} indicates an altered environment due to the higher polymerization degree of the VO_x species, as confirmed earlier by XRD and Raman spectroscopy. After thermal aging, the spectra of the samples generally showed a reduced intensity. In the OH region, the main band shifts to 3635 cm^{-1} indicating the oligomerization/polymerization of VO_x species and the formation of bridged V-(OH)-V groups. In the N-H region, the feature of the Brønsted acid sites shifts to 1430 cm^{-1} as the main signal,

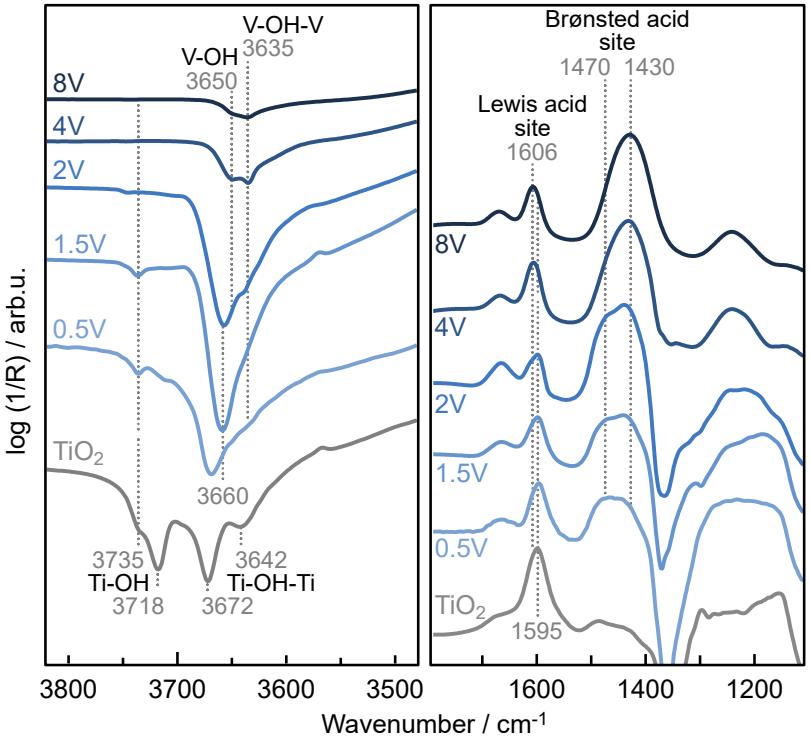

Figure 4.14: *DRIFT spectra of the NH_3 adsorption at room temperature on the VO_x/TiO_2 catalysts and TiO_2 support. ν(O-H) region (left) and δ(N-H) deformation modes (right) of NH_3 adsorbed on Lewis and Brønsted acid sites.*

representing the NH_4^+ formation predominantly on bridged OH groups.

The outcomes of the band assignment for the ammonia adsorption on Brønsted acid sites are summarized in Fig. 4.15.

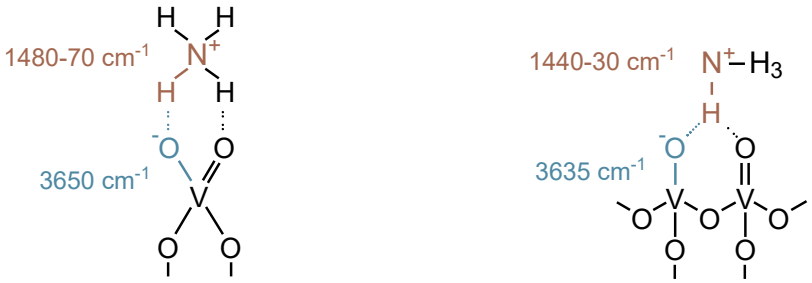

Figure 4.15: *Proposed structure of ammonia adsorbed on monomeric (left) and polymeric (right) Brønsted acid sites.*

Based on the acquired expertise in **Paper I**, the band assignment was further conducted on the modified TiO_2 and the VO_x/TiO_2 catalysts before and after aging in **Paper II** and **III**. The adsorption spectra are displayed in Fig. 4.16 and 4.17. In particular, the correlation of the O-H signals from the modified TiO_2 with those of the modified VO_x/TiO_2 catalysts, allowed the differentiation of isolated and bridged hydroxyls for the respective modifier (M), e.g. M-(OH)-Ti or M-(OH)-V.

In Fig. 4.16, the Ce- and Nb-modified supports (Ce/Ti, Nb/Ti) feature O-H bands similar to those of bare TiO_2. The broad features around 3630–3600 cm^{-1} and 3650–3620 cm^{-1} indicate bridging hydroxyls between titanium and the modifier, as Ce-(OH)-Ti or Nb-(OH)-Ti, respectively. For Nb/Ti, the more pronounced intensity around 3690 cm^{-1} is similar to Nb-OH in bulk Nb_2O_5 at 3702 cm^{-1} [127] and suggests the presence of isolated Nb-OH, which appears more distinctly after aging. With the addition of antimony oxide (Sb/Ti), the intensity of the suppressed O-H signals is relatively low, suggesting that most of the titania sites are covered by antimony oxide entities. The bands at 3707 and 3624 cm^{-1} are proposed to originate from isolated Sb-OH and bridged OH groups, either Sb-(OH)-Ti or Sb-(OH)-Sb. Notably, after the aging procedure, the O-H bands intensify. The more intense band at 3707 cm^{-1} suggests that more isolated Sb-OH sites have formed throughout the aging process while revealing additional titania sites as the intensities of the bands at 3735 cm^{-1} and 3670 cm^{-1} are also increased.

In the N-H deformation region, Ce/Ti and Nb/Ti show weak bands of Brønsted acid sites, while the modification with niobium oxide results in a higher intensity, suggesting that the niobium oxide species have a Brønsted acid character. After the aging procedure, the intensity of the Brønsted bands on Ce/Ti increases, suggesting that more Ce-(OH)-Ti sites have been formed. With respect to that, Li et al. [128] discussed the potential incorporation of titanium into ceria species as to create Ce-O-Ti sites. On Nb/Ti, the intensity decreases and shifts to a higher wavenumber, representing the adsorption primarily on isolated/monomeric surface sites, which indicates a segregation of the niobium oxide species to form isolated NbO_x species. For Sb/Ti, the intensity increases for both acid sites. Notably, the Brønsted bands shift to higher wavenumbers, also suggesting a segregation and formation of isolated SbO_x species, while exposing additional TiO_2 sites. These observations correlate with the findings of Eppler [129], suggesting the incorporation of antimony into titania. The exposed additional TiO_2 may contribute to the observed higher NH_3 uptake after aging, due to the higher ammonia adsorption capacity [39, 106] (as discussed in Section 4.2).

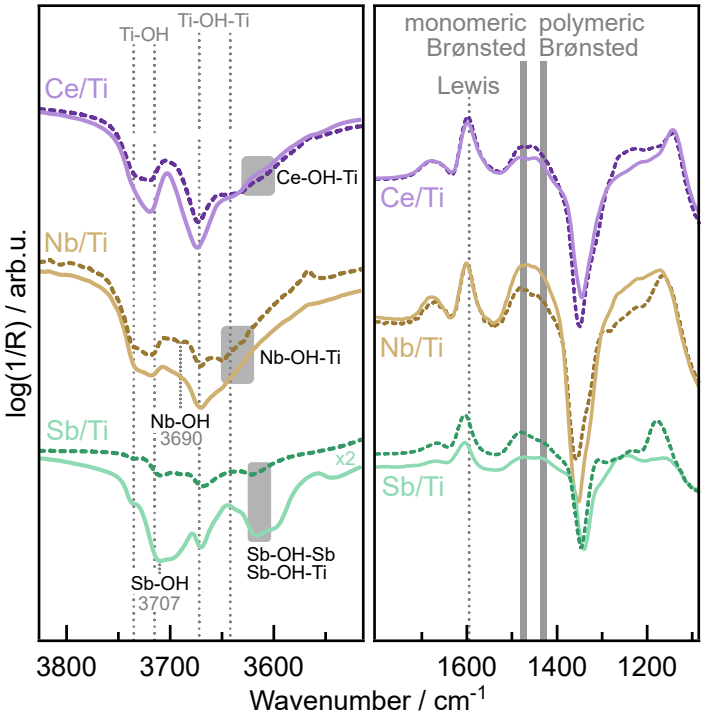

Figure 4.16: *DRIFT spectra of the NH_3 adsorption at room temperature on the modified TiO_2 before (solid line) and after (dashed line) aging. ν(O-H) region (left) and δ(N-H) deformation modes of NH_3 adsorbed on Lewis and Brønsted acid sites (right). The intensity of the O-H bands on Sb/Ti was adjusted by a factor of two for better visibility.*

The spectral analysis of the modified VO_x/TiO_2 catalysts (Fig. 4.17) reveals the formation of different hydroxyl species and provides information about the interaction of vanadium with the modifiers. The spectrum of V-Ce/Ti exhibits a main band centered at 3660 cm^{-1}, suggesting a high degree of monomeric V-OH sites. In addition, a broad shoulder at around 3620–3600 cm^{-1} is assigned to bridged Ce-(OH)-V sites. After aging, the band shifts to 3639 cm^{-1}, suggesting that more bridged hydroxyls and thus more polymerized VO_x species have formed throughout the thermal treatment. The shoulder at around 3704 cm^{-1} indicates Ce-OH sites, which originate from the formed crystalline CeO_2 as confirmed by XRD and Raman spectroscopy. The spectra of the V-Nb/Ti catalysts exhibit a shoulder related to isolated Nb-OH sites (3690 cm^{-1}). A weak feature around 3620–3590 cm^{-1} is observed and assigned to Nb-(OH)-V groups, suggesting a low initial interaction between V and Nb and resulting in a higher degree of polymerized VO_x (3648 cm^{-1}) compared to the reference. The Sb-modified catalyst shows strong bands related to bridged Sb-(OH)-V hydroxyl groups (3624 cm^{-1}), alongside isolated Sb-OH (3707 cm^{-1}) and

vanadium hydroxyl groups (3651 cm^{-1}). After aging, the intensities of the vanadium hydroxyls and Sb-O-H bands increase. In contrast, the intensity of the bridged Sb-(OH)-V groups decreases, suggesting a segregation of vanadium and antimony oxides on the surface throughout the aging process, resulting in isolated Sb-OH and more available sites of vanadium hydroxyls.

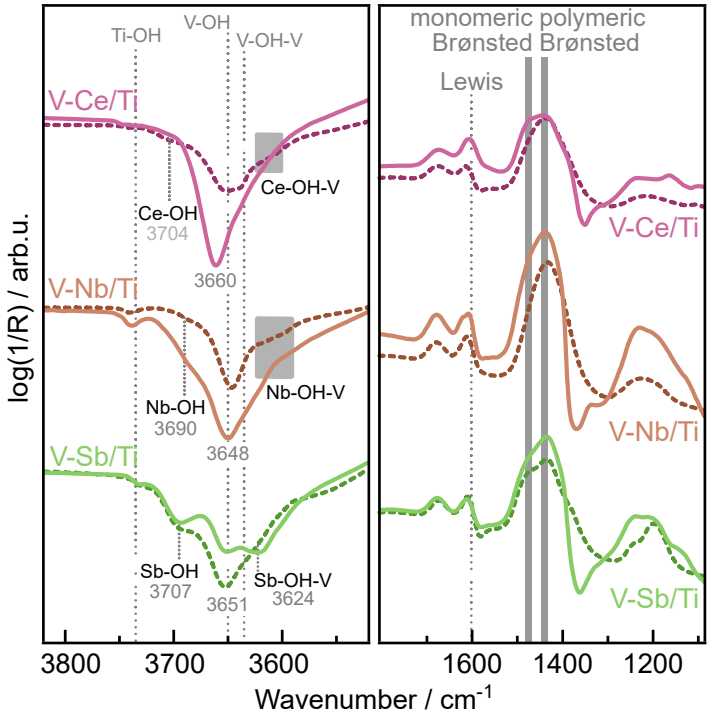

Figure 4.17: *DRIFT spectra of the NH_3 adsorption at room temperature on the modified VO_x/TiO_2 catalysts supports before (solid line) and after (dashed line) aging. ν(O-H) region (left) and δ(N-H) deformation modes of NH_3 adsorbed on Lewis and Brønsted acid sites (right).*

The spectra in the N-H deformation region show a more intense band at 1430 cm^{-1} on V-Ce/Ti, suggesting that NH_4^+ predominantly forms on bridged OH sites after aging, which indicates that aging causes polymerization of VO_x species. The Brønsted feature located at 1439 cm^{-1} and a shoulder around 1480 cm^{-1} indicate that mainly bridged V-(OH)-V or V-(OH)-Nb sites are present, which becomes more pronounced after aging. The V-Sb/Ti catalyst shows that the intensity of Lewis acid sites increases after aging. Correlating the DRIFT spectra with the activity data (Section 4.2.1) suggests that increased performance after aging is directly related to the increased intensity of the vanadium hydroxyl groups.

Table 4.1: *Assignment of hydroxyl bands in the wavenumber region of 3700-3600 cm^{-1} upon the adsorption of ammonia*

Position /cm^{-1}	Assignment	Vibration
3660-3650	terminal V-OH	ν(OH)
3635	bridging V-(OH)-V	ν(OH)
3704	terminal Ce-OH	ν(OH)
3630-3600	bridging Ce-(OH)-Ti	ν(OH)
3620-3600	bridging Ce-(OH)-V	ν(OH)
3690	terminal Nb-OH	ν(OH)
3650-3620	bridging Nb-(OH)-Ti	ν(OH)
3620-3590	bridging Nb-(OH)-V	ν(OH)
3707	terminal Sb-OH	ν(OH)
3622-3604	bridging Sb-(OH)-Ti / Sb-(OH)-Ti	ν(OH)
3624	bridging Sb-(OH)-V	ν(OH)

Concluding interpretation of characterization results with DRIFTS

Correlating the DRIFT adsorption spectra with the activity and characterization helped to gain a better understanding of the catalyst's surface before and after thermal aging. A visualization of the interpreted results is given in Fig. 4.18, with emphasis on the respective alteration of the surface area (SSA) and theoretical monolayer coverage of titania by the different compounds. During thermal aging of VO_x/TiO_2 catalysts, the titania support and VO_x phases undergo different changes. Commonly, thermal aging involves sintering of the TiO_2-anatase particles, eventually accompanied by an anatase-to-rutile phase transformation, leading to a significant loss of specific surface area, which is directly linked to particle growth. The presence of vanadium oxides on titania enhances these processes, and the effect correlates with the added amount, or surface density, of the vanadium oxides [102–104]. Consequently, the available surface area for the dispersed phase shrinks, which affects the VO_x species. They may undergo aggregation, forming higher polymerized VO_x species, and in some cases form crystalline V_2O_5, which potentially leads to pore clogging [48]. The crystalline V_2O_5 particles promote side reactions such as ammonia oxidation and N_2O formation, ultimately resulting in an overall decreased catalytic performance [104].

The modification of VO_x/TiO_2 with the modifiers shows a stabilizing effect on both the TiO_2 support and the VO_x species. The absolute majority of the titania sites are covered by vanadium and the modifiers, with the latter counteracting the TiO_2-anatase sintering. This is apparent for the niobium and antimony oxide modifications, for which the surface area remains high and no crystalline metal oxides are detected. This in turn prevents the agglomeration of the VO_x species such that no detectable

V_2O_5 forms. The preserved structural properties result in an overall consistent activity and selectivity after the aging procedure, compared to the unmodified catalyst reference.

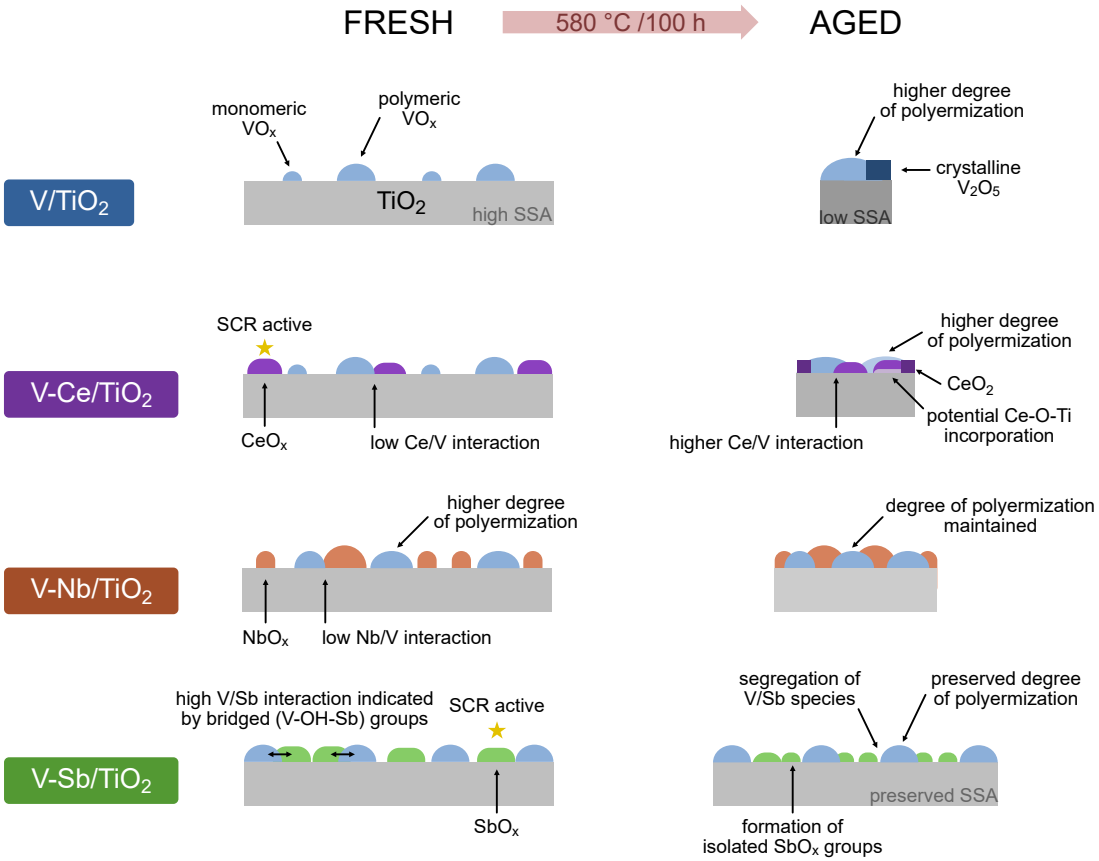

Figure 4.18: *Schematic illustration of the consequences of the aging procedure and the deactivation mechanisms that are counteracted by the modification with Ce, Nb, or Sb. All modifiers hinder the formation of V_2O_5. The cerium oxide and antimony oxide species show some SCR activity.*

4.3.2 Adsorption of nitrogen monoxide

Surface NO_x species are important intermediates in the NH_3-SCR reaction, and their identification is essential. The number of coexisting species on the surface and overlapping infrared bands within a narrow wavenumber region make the assignment challenging. Despite the challenges, it is commonly accepted that nitrates, NO, and NO_2 are the predominant species adsorbed on vanadium-titanium oxide surfaces [130, 131]. The structure of the nitrates is presented in Fig. 4.19.

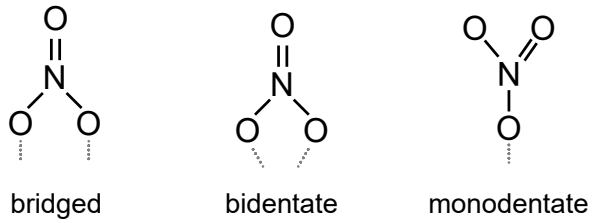

Figure 4.19: *Structures of surface nitrate species on metal oxides.*

In **Paper I**, the *in situ* DRIFT adsorption spectra of nitrogen monoxide on TiO_2 and the VO_x/TiO_2 catalysts were recorded after exposing the samples to 500 ppm of NO for 20 min at room temperature, and are displayed in Fig. 4.20. The region of interest (1700–1200 cm^{-1}) is related to $\tilde{\nu}$(N=O) and asymmetric $\tilde{\nu}$(ONO) vibrations of surface nitrates as well as gaseous or weakly adsorbed NO_2. The respective symmetric $\tilde{\nu}$(ONO) vibrations are located below 1000 cm^{-1} and cannot be observed due to the lattice vibrations of TiO_2. Based on the values found in literature [131–133], the assignment of bridged nitrates (1645 cm^{-1}), bidentate (1578 cm^{-1}), and monodentate nitrates (1508 cm^{-1}) as well as their respective split vibrations was made. The main band for most of the samples is centered around 1625 cm^{-1}, corresponding to the asymmetric $\tilde{\nu}$ vibration of NO_2, which is easily formed in the presence of surface oxygen. The respective symmetric mode (1325 cm^{-1}) is only observed with Raman spectroscopy [130, 131].
The spectrum of the TiO_2 support reveals a main band related to N_2O (1628 cm^{-1}), and vibrations of bidentate (1585 cm^{-1}) as well as monodentate nitrates (1504 cm^{-1}). The respective $\tilde{\nu}_{as}$(ONO) vibrations of bidentate and monodentate nitrates are located at 1288 and 1244 cm^{-1}. The negative bands around 1360-50 cm^{-1} belong to covered surface sulfates, as mentioned in Section 4.3.1. With vanadium introduced onto the support, the bands undergo slight shifts with respective positions at 1624 cm^{-1} (NO_2), 1579 and 1284 cm^{-1} (bidentate NO_3^-), 1510 and 1242 cm^{-1} (monodentate NO_3^-). As the vanadium loading increases, the relative amount of monodentate and bidentate nitrates decreases whereas the band related to bridged nitrates (1645 cm^{-1}) arises until becoming the main band for a vanadium

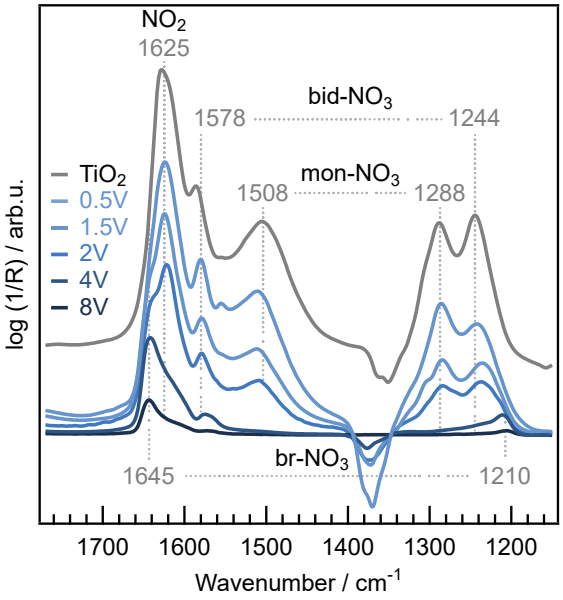

Figure 4.20: *DRIFT spectra for the adsorption of NO at room temperature on the VO_x/TiO_2 catalysts as well as TiO_2 support.*

loading higher than 4 wt%. The respective split vibrations in the area of 1300–1200 cm^{-1} further confirm the gradual decrease of monodentate and bidentate nitrate bands, resulting in a distinct band for bridged nitrates at 1210 cm^{-1} as the loading increases.

To investigate how the contribution of the respective species changes, the adsorption spectra were decomposed through peak fitting using Voigt profiles. The positions of the bands were reviewed by analysis of the time-resolved spectra and revealed additional bands for NO_2, bidentate and monodentate nitrates. An example of the peak decomposition for the spectrum of the VO_x/TiO_2 catalyst with a loading of 2 wt% is presented in Fig. 4.21. Additional bands for NO_2, bidentate and monodentate nitrates (bid-NO_3, mon-NO_3) were found. A detailed band assignment of the NO_x surface species on VO_x/TiO_2 along with the respective wavenumbers is summarized in Table 4.2.

The integration of the fitted peaks enables comparison of the ratio of the different NO_x species on the samples (Fig. 4.21). For the bare TiO_2, adsorbed NO_2 and monodentate nitrates are the dominant species. As the vanadium loading increases, the proportion of monodentate nitrates declines, while the ratio of bridged nitrates steadily increases. Adsorbed NO_2 remains the dominant species for most of the catalysts, as only the highest vanadium loading (8 wt%) reveals bridged nitrates as the main species. This suggests that bridged nitrates are preferably formed on crystalline V_2O_5 particles.

Table 4.2: *Assignment of NO_x adsorption bands in the wavenumber region 1700-1200 cm^{-1}*

Band position /cm^{-1}	Band Assignment	Notation	Vibration
1645	bridged nitrate on V	bri-NO_3	$\tilde{\nu}$(N=O)
1631	bridged nitrate on Ti	bri-NO_3	$\tilde{\nu}$(N=O)
1625	gaseous/adsorbed NO_2	NO_2	$\tilde{\nu}_{as}$(NO_2)
1605	gaseous/adsorbed NO_2	NO_2	$\tilde{\nu}_{as}$(NO_2)
1578	bidentate nitrate	bid-NO_3	$\tilde{\nu}$(N=O)
1556	bidentate nitrate	bid-NO_3	$\tilde{\nu}$(N=O)
1533	monodentate nitrate	mon-NO_3	$\tilde{\nu}$(N=O)
1508	monodentate nitrate	mon-NO_3	$\tilde{\nu}$(N=O)
1288-81	monodentate nitrate	bri-NO_3	$\tilde{\nu}_{as}$(ONO)
1244-33	bidentate nitrate	bid-NO_3	$\tilde{\nu}_{as}$(ONO)
1210	bridged nitrate	mon-NO_3	$\tilde{\nu}_{as}$(ONO)

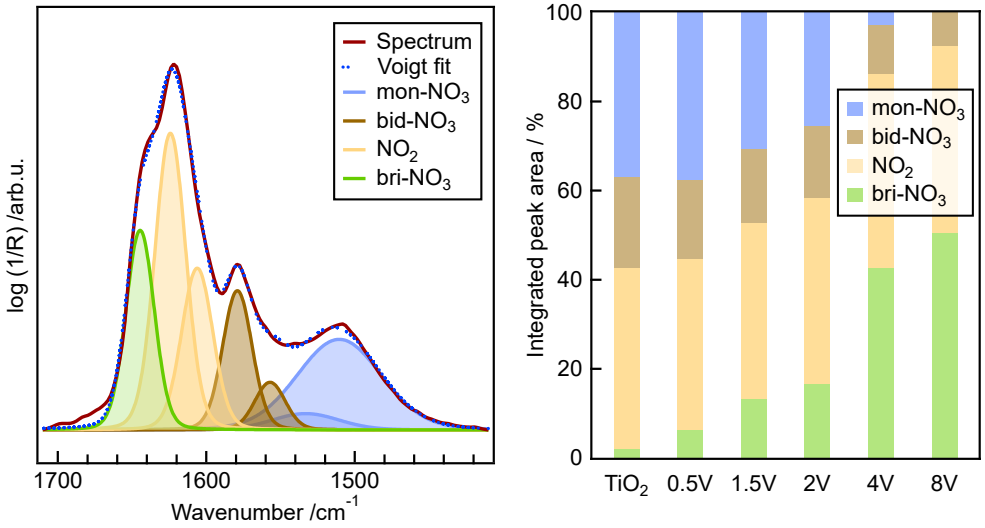

Figure 4.21: *Decomposed spectrum for the VO_x/TiO_2 catalyst with a vanadium loading of 2 wt% (left) and relative abundance of NO_x species on the VO_x/TiO_2 catalysts as well as TiO_2 support (right).*

Based on the expertise gained in **Paper I**, peak decomposition was also conducted for the modified supports and catalysts before as well as after aging (**Paper II** and **III**). The comparison from the integrated peak area shows a different distribution of the surface NO_x species. The modification with cerium oxide (Ce/Ti) induces a higher ratio of monodentate nitrates (42%) compared to the bare support. In contrast, with the presence of niobium oxide (Nb/Ti), a higher ratio of bridged nitrates (25%) is formed. The aging procedure does not significantly alter the species distribution on those samples. In contrast, Sb/Ti exhibits notable changes throughout

aging. While in the fresh state, the distribution of the surface species resembles that of bare TiO_2, aging leads to a higher ratio of NO_2 and bidentate nitrates at the expense of monodentate nitrates.

The comparison of the modified catalysts with the reference shows that V-Ce/Ti has a high ratio of bidentate nitrates (42%), which shifts to a higher fraction of bridged nitrates (36%) after aging. The modification with niobium oxide (V-Nb/Ti) shows a high ratio of bridged nitrates (29%), which becomes even more pronounced after aging (49%). For the Sb-modified catalysts (V-Sb/Ti), NO_2 remains the dominant species throughout thermal stress, with minimal changes upon aging.

The results of peak decomposition show that the addition of the modifiers affects the overall ratio of formed NO_x species on the surface. While the correlation between respective nitrate species and catalytic activity remains unresolved, the findings encourage future investigations. Transient *in situ* spectroscopic studies by modulation excitation experiments and phase-sensitive detection analysis may give insights about active and spectator species through a periodic perturbation of the given system [36, 134, 135].

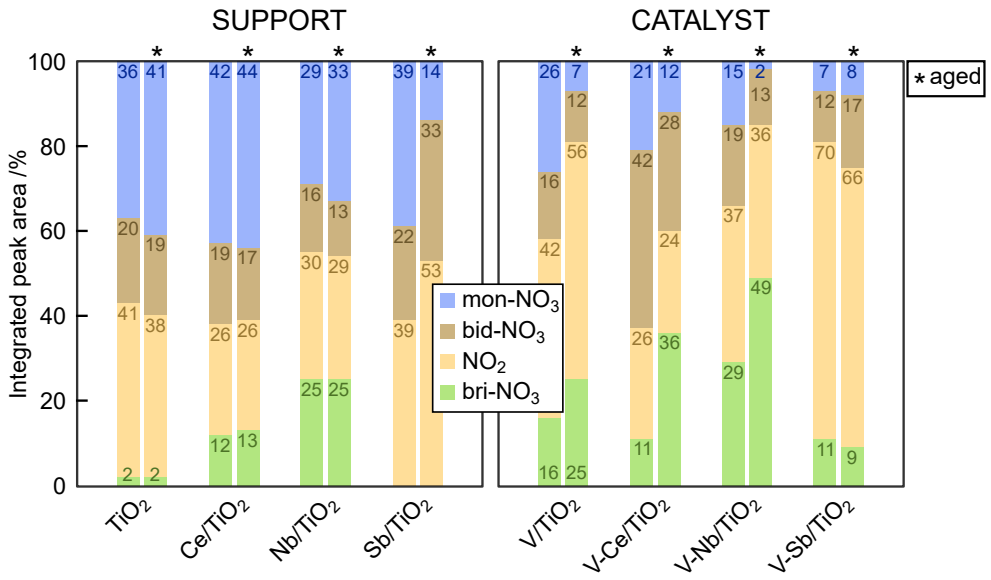

Figure 4.22: *Summary of peak-fitted spectra with relative abundance of NO_x species on the modified VO_x/TiO_2 catalysts and TiO_2 before and after (*) aging.*

4.3.3 Adsorption of water

Understanding the interaction of water with VO_x/TiO_2 is essential for catalyst optimization in the NH_3-SCR reaction, where water is both a product but also an inhibitor. In general, the presence of water is known to significantly reduce the overall NO_x conversion at low temperatures due to blocking the adsorption sites and competing with the reactants [64, 136]. Takeuchi et al. [137] proposed structures of adsorbed H_2O that differ in the number of intermolecular hydrogen bonds, as demonstrated in Fig. 4.23.

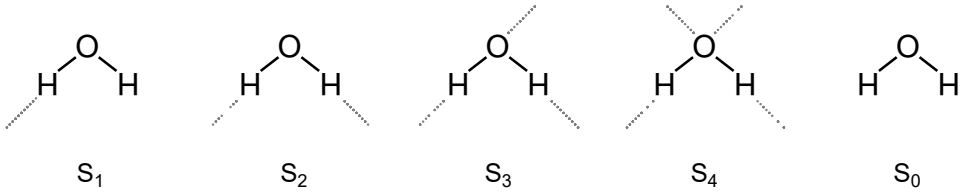

Figure 4.23: *Structure of adsorbed H_2O with different numbers of hydrogen bonds. Adapted from Ref. [137].*

In **Paper IV**, the adsorption of water was conducted with an Argon stream, containing 600 ppm of H_2O, at temperatures starting from 350 °C to 50 °C. Followed by desorption in an Argon atmosphere from 50 °C to 350 °C. The analysis of the DRIFT spectra focused on the H-O-H deformation modes of water (1700–1500 cm^{-1}). The adsorption of water on the TiO_2 support at 350 °C reveals a weak adsorption band around 1617 cm^{-1}, which most likely correlates to the S_1 mode as described by Takeuchi et al. [137]. As the temperature decreases, the intensity of this band increases coupled with a shift to a higher wavenumber ($\sim$1635 cm^{-1}), suggesting an increase in surface coverage and the formation of multilayers, with a higher degree of hydrogen bonds (S_3, S_4). Below a temperature of 100 °C another band located at 1595 cm^{-1} arises. While this band has been attributed to water coordinated to Ti^{4+} sites [138], which is thermally stable, the observed temperature-dependent behavior in the spectra suggests an alternative assignment that is related to the presence of water vapor. Kevorkyants et al. [139] proposed the vibration around 1560 cm^{-1} as a single water molecule in the water bulk. Potential shifts to higher frequencies (1590 cm^{-1}) originate from the interaction of H-atoms of the adsorbed water molecule with O-atoms in the bulk. A summary of the band assignment is provided in Table 4.3.

Upon the desorption experiment, the spectrum at 50 °C exhibits a decrease in intensity of the vibrational band around 1635 cm^{-1}, which suggests to be related to weakly bound water. In the temperature range of 100–200 °C, the desorption spectra closely resemble those obtained under

Table 4.3: *Band assignment of deformation vibrations of H_2O*

Position /cm^{-1}	Assignment	Mode
1645	liquid water [139]	S_0 [137]
1635	multilayer or weakly bonded water	S_3,S_4 [137]
1617	monolayer or strongly bonded water	S_1,S_2 [137]
1595	associated with water vapor [140] or physisorption	-
1560	isolated water molecules in bulk-like state [139]	-

a continuous flow of water, suggesting that a dynamic equilibrium exists between adsorption and desorption within this temperature range, where the water molecules are neither firmly bound nor irreversibly lost. At higher temperatures ($\geq 300\,°C$), the spectral intensity is markedly reduced compared to the adsorption spectra and implies the irreversible desorption of water molecules.

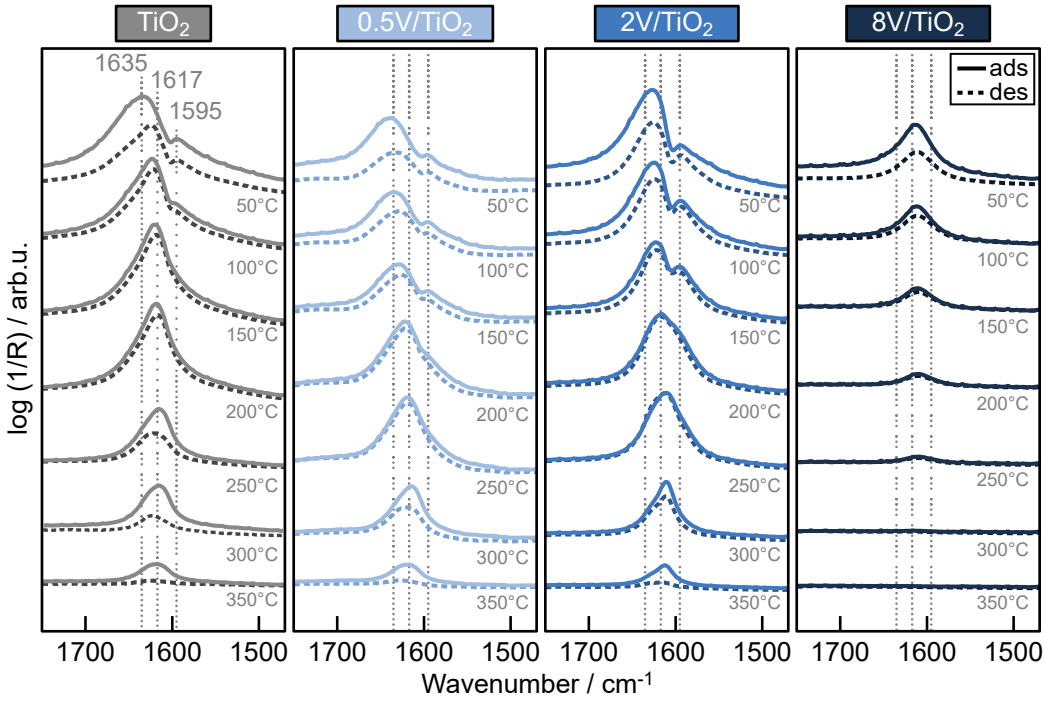

Figure 4.24: *DRIFT spectra for the adsorption and desoprtion of H_2O on the VO_x/TiO_2 catalysts as well as TiO_2 support at temperatures from 350 to 50 °C.*

To evaluate the influence of the vanadium loading on the adsorption and desorption of water, the same experimental procedure was conducted on VO_x/TiO_2 catalysts with a vanadium loading of 0.5, 2.0, and 8.0 wt%, respectively. The spectra of the water adsorption on the catalyst with a loading of 0.5 wt% show generally similar adsorption characteristics as the bare TiO_2 support, which implies that such low quantities of vanadium

oxide do not impact the adsorption of water. With a higher vanadium content (2 wt% V), the adsorption band at 50 °C centers around 1627 cm^{-1}, indicating a lower surface coverage. For the catalysts with a loading of 8 wt%, the water adsorption is low for high temperatures (>150 °C), while the band position around 1613 cm^{-1} at 50 °C suggests that the adsorption occurs predominantly in the S_1 mode.

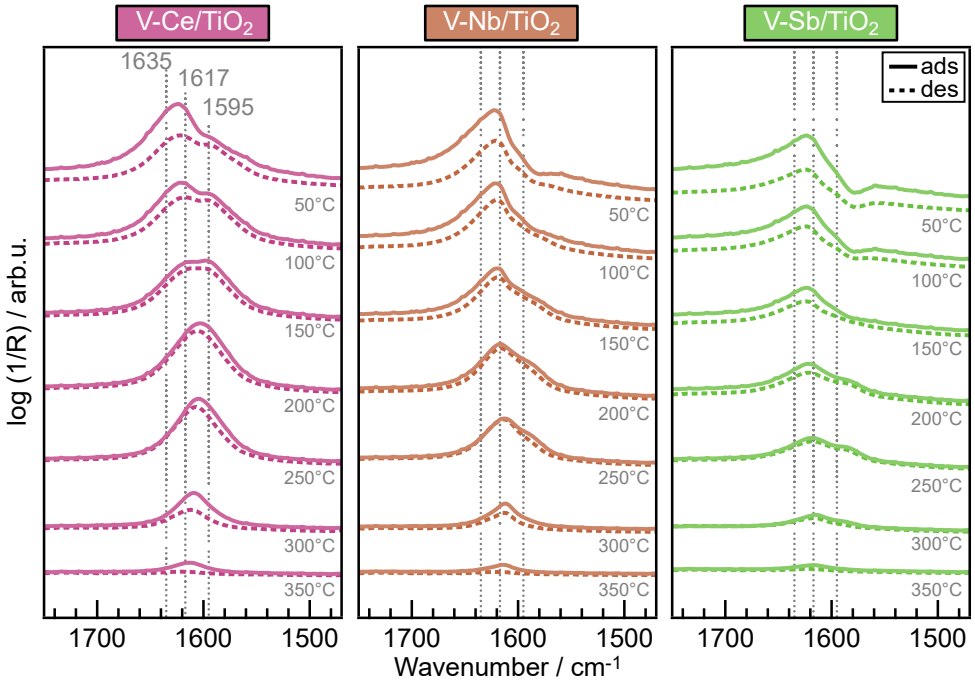

Figure 4.25: *DRIFT spectra for the adsorption and desorption of H_2O on the modified VO_x/TiO_2 catalysts at temperatures from 350 to 50 °C.*

The introduction of modifiers to the VO_x/TiO_2 system further altered the water adsorption characteristics. The Ce-modified catalysts (V-Ce/TiO_2) show a high contribution of a shoulder at 1595 cm^{-1} starting from temperatures of 150 °C. Under desorption conditions, a strong water-surface interaction is observed at mid-temperatures (150 to 250 °C). The spectra of the Nb-modified catalyst (V-Nb/TiO_2) at 50 °C show a band located at 1623 cm^{-1} and suggests the water adsorption predominantly in S_1,S_2 like configurations, rather than adsorption in multilayers (S_3,S_4). The desorption spectra with a similar band intensities at temperatures 150– 250 °C suggest a strong surface-water interaction in this range. The spectra of the Sb-modified catalyst (V-Sb/TiO_2) exhibit the overall lowest adsorption of water among the modified catalysts. At 50 °C, the main band around 1623 cm^{-1} indicates the water adsorption in the S_1,S_2 mode. A negative band around 1577 cm^{-1} potentially corresponds to vibrations of formic acid (-CO_3H) [141], originating from residual acetate species in the

Sb precursor that has been used in sample synthesis.

Water has been shown to negatively influence the SCR activity over VO_x/TiO_2 catalysts [142]. One may consider that a low adsorption of water and a rapid desorption from the catalyst surface are beneficial for the overall catalytic activity. For instance, a high vanadium loading has shown a weak adsorption of water and an overall high SCR activity (Section 4.1.1). The higher load leads to a coverage of the TiO_2 support, resulting in the formation of V-OH or V-(OH)-V groups on the surface (Section 4.3.1), which suggest to have a lower water adsorption capacity. In addition to that, the modification with the metal oxides indicated a weaker adsorption of water while also showing a higher SCR activity, compared to the unmodified reference. Nevertheless, the H_2O adsorption is not the only factor to be considered for the SCR activity, and the relevance of the water adsorption in the SCR reaction requires further investigations.

5 Conclusions and Outlook

This work aims to contribute to an overall improved fundamental understanding of VO_x/TiO_2 catalysts for the application in mobile sources, guiding towards a more rational catalyst design. The effect of the vanadium loading, implementation of different modifiers (oxides of Ce, Nb, Sb), as well as the impact of thermal aging, were investigated by various *ex-situ* characterization techniques, flow reactor measurements, and *in-situ* spectroscopic methods.

In the first part of this work, a comprehensive evaluation of VO_x/TiO_2 catalysts with varying vanadium loadings revealed that a high vanadium loading exhibits a high low-temperature activity in fresh state, compromising the long-term stability, whereas a low vanadium loading benefits in thermal stability, and in the case of the 1.5V catalyst, improved catalytic performance after aging. The catalyst deactivation through thermal aging was closely linked to physicochemical changes, sintering of TiO_2, and formation of V_2O_5 linked to a reduced availability of the VO_x species. The correlation between specific surface area (SSA) and NH_3-uptake with the NO_x conversion indicated that those parameters should generally not be considered as main design parameters for the SCR reaction. Rather, the redox properties seem to play a significant role in the conversion of NO_x. The second part explored the impact of metal oxide modifiers on the catalyst durability and activity. The inclusion of cerium oxide enhanced low-temperature activity, while the incorporation of niobium oxide significantly stabilized the VO_x species and titania support, preserving the surface area and VO_x dispersion throughout thermal stress. Notably, the antimony-modified catalysts demonstrated an exceptional preservation of the catalyst texture and catalytic performance after thermal stress. The observed improvements are attributed to the absence of crystalline V_2O_5 post-aging, stabilization of polymeric VO_x species, and potential contributions to redox properties by the cerium oxide and antimony oxide species. At a low loading, *in situ* Raman spectroscopy indicated that the dispersed monomeric VO_x species were preserved upon thermal stress in the presence of the modifiers, most notably with cerium oxide. In the third part, molecular probe infrared spectroscopy studies provided insights into the surface characterization and fundamental adsorption of the probing gases. The surface characterization allowed the

differentiation of the surface hydroxyl groups (OH) as well as adsorbed surface species of ammonia, NO, or water. Peak decomposition of NO adsorption bands enabled the comparison of surface species ratios. Upon the adsorption of water, both the vanadium loading and modification with metal oxides had an impact on the adsorption characteristics. For instance, on unmodified VO_x/TiO_2, the adsorption of water and coverage decreased with increasing vanadium loading. Those findings could provide potential for further investigations.

The findings in this thesis open up for future research on titania-supported vanadium oxide catalysts, beyond the application in the selective catalytic reduction (SCR) of nitrogen oxides (NO_x) to extend to a broader range of applications. The modifications of the VO_x/TiO_2 catalysts were conducted with a near-equimolar ratio of the modifier and vanadium. Further investigations could focus on a systematic optimization of the catalyst composition, by variation of both the vanadium and the modifiers loading. In this work, the catalysts were individually modified, while the combined effect of two or more modifiers has been unresolved. Future studies could examine the co-modification of VO_x/TiO_2 by various combinations, that may also include tungsten- and silicon-oxide. Subsequent studies should also address the catalytic performance under more practical conditions *via* hydrothermal aging as well as in the presence of contaminants (e.g., SO_2). Such assessments would provide additional insights into the long-term stability and robustness of the catalysts. Investigating the impact of the modifiers on the coordination and valence of vanadium would be an interesting subject for investigation. Advanced spectroscopic techniques such as *in situ* X-ray absorption fine structure (XAFS) could elucidate the local and electronic structure/coordination of vanadium as well as oxidation states, while nuclear magnetic resonance (NMR) could provide complementary information about the quantitative distribution and alteration of the different VO_x species. These methods might advance the understanding of structure–function relationships in this catalytic system. Finally, the surface analysis has demonstrated the effect of the modifiers on the formation of different surface NO_x species. Yet, the correlation between respective nitrate species and catalytic activity remains unresolved, which could be studied by transient spectroscopic studies through modulation excitation experiments and phase-sensitive detection analysis to give insights about active and spectator species.

Acknowledgments

This work is financially supported by the Swedish Energy Agency through the FFI program "Ultra-efficient recyclable De-NO_x catalysts for biofuel and hybrid powertrains" (No. 51318-1), the Swedish Research Council through the project "Infrared Spectroscopy in Time and Space" (Dnr. 2019-05528) and the Competence Centre for Catalysis, which is hosted by Chalmers University of Technology and financially supported by the Swedish Energy Agency and the member companies AB Volvo, ECAPS AB, Johnson Matthey Plc, Perstorp AB, Powercell AB, Preem AB, Scania CV AB, Umicore AG & Co. KG.

The research presented in this thesis has been performed at the Division of Applied Chemistry and Competence Centre for Catalysis (KCK). Parts of this work were conducted at the Johnson Matthey Technology Centre (Reading, UK), Chalmers Material Analysis Laboratory (CMAL), and the University of Patras (Greece).

A PhD thesis is never the result of the efforts done by only one; rather, it is a collaborative accomplishment shaped by the support, guidance, and encouragement of many individuals along the way.

Hence, I would like to thank:

- My supervisor Per-Anders Carlsson for the confidence and giving me the opportunity to work on this project. I am very grateful for your constant support, the freedom to explore, and the feedback throughout this time.
- My co-supervisor Anna Martinelli for the help with the Raman instrument and feedback on the manuscripts from an "outside" perspective.
- My co-supervisor Andreas Schaefer for all the support, ranging from practical to software-related matters, text corrections, as well as conducting the XPS and XRF measurements.
- Agnes Raj, Roberta Villamaina, Kaneshalingam Arulraj, Andrew Newman, and Mikaela Wallin for the collaboration and the

constructive meetings.

- Soghomon Boghosian, Theocharis Kentri, and Iliana-Maria Stergiou for the nice collaboration, last-minute support, and hosting me as a visiting researcher.

- My examiner Magnus Skoglundh for evaluating my research progress and providing a motivating environment in the KCK. Lasse Urholm and Lennart Norberg for their help and maintenance of the KCK setups and equipment.

- Lotta Pettersson, Anna Oskarsson, and Emma Andersson for the administrative work and organization of the various parties and events, making the division such a great place to work.

- All the current and former members of my working group, namely Chris, Felix, Guido, Mengqiao, Rasmus, Vasiliki, and Yanyue, who helped me with stimulating discussions and the practicalities in the beginning stage.

- All the people from Applied Chemistry and KCK, who accompanied me along the way, for the nice atmosphere and good spirit, which includes the Fika, sports sessions, after-works, and much more.

- A selected group, that has been a great source of distraction during my PhD journey, although situated in other places, our frequent reunions made me forget some stressful times. Shout-out to Christian, Laurin, Luca, Matthias, Nicholas, Sven, Tim, Tim, and Tim.

- Judith for your love, support, and patience. You enrich my life in so many ways and have made my final year so special.

Zum Schluss möchte ich meiner Familie danken – meinen Eltern, Großeltern, meiner Schwester Charlotte und meinem Schwager Kristian. Liebe Mama, lieber Papa, ohne eure Anstrengungen und Mühen, eure Erziehung und Ermutigungen, wäre dieser Weg nicht möglich gewesen.

References

[1] Munawer, M. E. Human health and environmental impacts of coal combustion and post-combustion wastes. *Journal of Sustainable Mining* **2018**, *17*, 87–96.

[2] Khodakarami, J.; Ghobadi, P. Urban pollution and solar radiation impacts. *Renewable and Sustainable Energy Reviews* **2016**, *57*, 965–976.

[3] U.S.E.P. Agency, Clean air act requirements and history, https://www.epa.gov/clean-air-act-overview/clean-air-act-requirements-and-history, Accessed: 2025-08-20.

[4] Nova, I.; Tronconi, E., *Urea-SCR Technology for deNO$_x$ After Treatment of Diesel Exhausts*; Springer, New York: **2014**, pp 3–31.

[5] The European Commission, Council Directive 91/441/EEC amending Directive 70/220/EEC on the approximation of the laws of the Member States relating to measures to be taken against air pollution by emissions from motor vehicles, Brussels, **1991**-06-26. https://eur-lex.europa.eu/legal-content/EN/ALL/?uri=CELEX%3A31991L0441, Accessed: 2025-08-20.

[6] The European Commission, COM(2022) 586: Proposal for a regulation on type-approval of motor vehicles and engines and of systems, components and separate technical units intended for such vehicles, with respect to their emissions and battery durability (Euro 7), Brussels, **2022**-11-10. https://single-market-economy.ec.europa.eu/publications/euro-7-standard-proposal_en, Accessed: 2025-08-20.

[7] Zhu, M.; Lai, J. K.; Wachs, I. E. Formation of N_2O greenhouse gas during SCR of NO with V_2O_5 by supported vanadium oxide catalysts. *Applied Catalysis B: Environmental* **2018**, *224*, 836–840.

[8] European Energy Agency, European Union emission inventory report 1990-2020. *Under the UNECE Air Convention*, **2022**. https://www.eea.europa.eu/publications/european-union-emissions-inventory-report, Accessed: 2025-08-20.

[9] EU emission standards for heavy-duty CI (diesel) engines: Steady-state testing. In dieselnet.com. `https://dieselnet.com/standards/eu/hd.php`, Accessed: 2025-08-20.

[10] Cheng, X.; Bi, X. T. A review of recent advances in selective catalytic NO_x reduction reactor technologies. *Particuology* **2014**, *16*, 1–18.

[11] Skalska, K.; Miller, J. S.; Ledakowicz, S. Trends in NO_x abatement: A review. *Science of The Total Environment* **2010**, *408*, 3976–3989.

[12] Roy, S.; Hegde, M.; Madras, G. Catalysis for NO_x abatement. *Applied Energy* **2009**, *86*, 2283–2297.

[13] Ando, J.; Tohata, H.; Isaacs, G. *NO_x Abatement for Stationary Sources in Japan*; U.S. Environmental Protection Agency, Cincinnati, Ohio, **1976**.

[14] Takagi, M.; Kawai, T.; Soma, M.; Onishi, T.; Tamaru, K. The mechanism of the reaction between NO_x and NH_3 on V_2O_5 in the presence of oxygen. *Journal of Catalysis* **1977**, *50*, 441–446.

[15] Havenith, C.; Verbeek, R.; Heaton, D.; Sloten, P. Development of a Urea DeNOx Catalyst Concept for European Ultra-Low Emission Heavy-Duty Diesel Engines. *SAE Technical Paper* **1995**, *952652*.

[16] Van Helden, R.; van Genderen, M.; van Aken, M.; Verbeek, R.; Patchet, J.; Kruithof, J.; Straten, T.; Gérentet de Saluneaux, C. Engine Dynamometer and Vehicle Performance of a Urea SCR-System for Heavy-Duty Truck Engines. *SAE Technical Paper* **2002**, *2002-01-0286*.

[17] Liu, Z. G.; Ottinger, N. A.; Cremeens, C. M. Vanadium and tungsten release from V-based selective catalytic reduction diesel aftertreatment. *Atmospheric Environment* **2015**, *104*, 154–161.

[18] Barceloux, D. G.; Barceloux, D. D. Vanadium. *Journal of Toxicology: Clinical Toxicology* **1999**, *37*, 265–278.

[19] Taylor, J.; Keith, S.; Cseh, L.; Ingerman, L.; Chappell, L.; Rhoades, J.; Hueber, A. *Toxicological profile for Vanadium*; U.S. Department of health and human services, Atlanta, **2012**.

[20] *U.S. EPA. IRIS Toxicological Review of Vanadium Pentoxide (External Review Draft, 2012)*; U.S. Environmental Protection Agency, Washington DC, **2011**.

[21] Ertl, G.; Knözinger, H.; Schüth, F.; Weithamp, J. In *Handbook of Heterogenous Catalysis*; Wiley-VCH: **2008**; Chapter 1, pp 1–15.

[22] Hu, X.; Yip, A. C. K. Heterogeneous Catalysis: Enabling a Sustainable Future. *Frontiers in Catalysis* **2021**, *1*, 667675.

[23] Chorkendorff, I; Niemantsverdrie, J. In *Concepts of Modern Catalysis and Kinetics*; John Wiley & Sons, Ltd: **2003**.

[24] Schmal, M. In *Heterogeneous Catalysis and its Industrial Applications*; Springer: **2016**.

[25] Koebel, M.; Madia, G.; Elsener, M. Selective catalytic reduction of NO and NO_2 at low temperatures. *Catalysis Today* **2002**, *73*, Environmental Catalysis, 239–247.

[26] Arnarson, L.; Falsig, H.; Rasmussen, S. B.; Lauritsen, J. V.; Moses, P. G. A complete reaction mechanism for standard and fast selective catalytic reduction of nitrogen oxides on low coverage $VO_x/TiO_2(001)$ catalysts. *Journal of Catalysis* **2017**, *346*, 188–197.

[27] Reif, K., *Diesel Engine Management*; Springer: **2014**.

[28] Lakshminarayanan, P. A.; Agarwal, A. K., *Design and Development of Heavy Duty Diesel Engines*; Springer: **2019**.

[29] Inomata, M.; Miyamoto, A.; Murakami, Y. Mechanism of the reaction of NO and NH_3 on vanadium oxide catalyst in the presence of oxygen under the dilute gas condition. *Journal of Catalysis* **1980**, *62*, 140–148.

[30] Ramis, G.; Busca, G.; Bregani, F.; Forzatti, P. Fourier transform-infrared study of the adsorption and coadsorption of nitric oxide, nitrogen dioxide and ammonia on vanadia-titania and mechanism of selective catalytic reduction. *Applied Catalysis* **1990**, *64*, 259–278.

[31] Ramis, G.; Yi, L.; Busca, G. Ammonia activation over catalysts for the selective catalytic reduction of NO_x and the selective catalytic oxidation of NH_3. An FT-IR study. *Catalysis Today* **1996**, *28*, 373–380.

[32] Topsøe, N. Y.; Dumesic, J. A.; Topsøe, H. Vanadia-titania catalysts for selective catalytic reduction of nitric-oxide by ammonia. II. Studies of active sites and formulation of catalytic cycles. *Journal of Catalysis* **1995**, *151*, 241–252.

[33] He, G.; Lian, Z.; Yu, Y.; Yang, Y.; Liu, K.; Shi, X.; Yan, Z.; Shan, W.; He, H. Polymeric vanadyl species determine the low-temperature activity of V-based catalysts for the SCR of NO_x with NH_3. *Science Advances* **2018**, *4*, 1–8.

[34] Marberger, A.; Ferri, D.; Elsener, M.; Kröcher, O. The Significance of Lewis Acid Sites for the Selective Catalytic Reduction of Nitric Oxide on Vanadium-Based Catalysts. *Angewandte Chemie - International Edition* **2016**, *55*, 11989–11994.

[35] Zhu, M.; Lai, J.-K.; Tumuluri, U.; Wu, Z.; Wachs, I. E. Nature of Active Sites and Surface Intermediates during SCR of NO with NH_3 by Supported V_2O_5-WO_3/TiO_2 Catalysts. *Journal of the American Chemical Society* **2017**, *139*, 15624–15627.

[36] Nuguid, R. J. G.; Ferri, D.; Marberger, A.; Nachtegaal, M.; Kröcher, O. Modulated Excitation Raman Spectroscopy of V_2O_5/TiO_2: Mechanistic Insights into the Selective Catalytic Reduction of NO with NH_3. *ACS Catalysis* **2019**, *9*, 6814–6820.

[37] Forzatti, P. Present status and perspectives in de-NO_x SCR catalysis. *Applied Catalysis A: General* **2001**, *222*, 221–236.

[38] Lai, J. K.; Wachs, I. E. A Perspective on the Selective Catalytic Reduction (SCR) of NO with NH_3 by Supported V_2O_5-WO_3/TiO_2 Catalysts. *ACS Catalysis* **2018**, *8*, 6537–6551.

[39] Busca, G.; Lietti, L.; Ramis, G.; Berti, F. Chemical and mechanistic aspects of the selective catalytic reduction of NO_x by ammonia over oxide catalysts: A review. *Applied Catalysis B: Environmental* **1998**, *18*, 1–36.

[40] Godiksen, A. L.; Rasmussen, S. B. Identifying the presence of $[V{=}O]^{2+}$ during SCR using in-situ Raman and UV Vis spectroscopy. *Catalysis Today* **2019**, *336*, 45–49.

[41] Lietti, L.; Alemany, J. L.; Forzatti, P.; Busca, G.; Ramis, G.; Giamello, E.; Bregani, F. Reactivity of V_2O_5-WO_3/TiO_2 catalysts in the selective catalytic reduction of nitric oxide by ammonia. *Catalysis Today* **1996**, *29*, 143–148.

[42] Vuurman, M. A.; Wachs, I. E.; Hirt, A. M. Structural determination of supported V_2O_5-WO_3/TiO_2 catalysts by in situ Raman spectroscopy and X-ray photoelectron spectroscopy. *Journal of Physical Chemistry* **1991**, *95*, 9928–9937.

[43] Pârvulescu, V.; Grange, P.; Delmon, B. Catalytic removal of NO. *Catalysis Today* **1998**, *46*, 233–316.

[44] Mamedov, E.; Cortés Corberán, V. Oxidative dehydrogenation of lower alkanes on vanadium oxide-based catalysts. The present state of the art and outlooks. *Applied Catalysis A: General* **1995**, *127*, 1–40.

[45] Kamata, H.; Ueno, S.-i.; Naito, T.; Yamaguchi, A.; Ito, S. Mercury oxidation by hydrochloric acid over a VO_x/TiO_2 catalyst. *Catalysis Communications* **2008**, *9*, 2441–2444.

[46] Dunn, J. P.; Stenger Jr, H. G.; Wachs, I. E. Oxidation of sulfur dioxide over supported vanadia catalysts: molecular structure-reactivity relationships and reaction kinetics. *Catalysis Today* **1999**, *51*, 301–318.

[47] Nguyen, T. H.; Thi Le, M. N.; Le Nguyen, D. A.; Mai, D. Q.; Duong Thai, N. P.; Nguyen, K. D.; Le, D. D.; Tran, P. H. Recent advances in selective 2,5-diformylfuran production from renewable biomass: Novel catalytic strategies and sustainable approaches. *Renewable and Sustainable Energy Reviews* **2025**, *215*, 115599.

[48] Madia, G.; Elsener, M.; Koebel, M.; Raimondi, F.; Wokaun, A. Thermal stability of vanadia-tungsta-titania catalysts in the SCR process. *Applied Catalysis B: Environmental* **2002**, *39*, 181–190.

[49] Jaegers, N. R.; Lai, J. K.; He, Y.; Walter, E.; Dixon, D. A.; Vasiliu, M.; Chen, Y.; Wang, C.; Hu, M. Y.; Mueller, K. T.; Wachs, I. E.; Wang, Y.; Hu, J. Z. Mechanism by which Tungsten Oxide Promotes the Activity of Supported V_2O_5/TiO_2 Catalysts for NO_x Abatement: Structural Effects Revealed by 51V MAS NMR Spectroscopy. *Angewandte Chemie - International Edition* **2019**, *58*, 12739–12746.

[50] Wachs, I. E. Catalysis science of supported vanadium oxide catalysts. **2013**, *42*, 11762–11769.

[51] Chen, C.; Cao, Y.; Liu, S.; Chen, J.; Jia, W. Review on the latest developments in modified vanadium-titanium-based SCR catalysts. *Chinese Journal of Catalysis* **2018**, *39*, 1347–1365.

[52] Lietti, L.; Nova, I.; Ramis, G.; Dall'Acqua, L.; Busca, G.; Giamello, E.; Forzatti, P.; Bregani, F. Characterization and Reactivity of V_2O_5–MoO_3/TiO_2 De-NO_x SCR Catalysts. *Journal of Catalysis* **1999**, *187*, 419–435.

[53] Alemany, L.; Lietti, L.; Ferlazzo, N.; Forzatti, P.; Busca, G.; Giamello, E.; Bregani, F. Reactivity and Physicochemical Characterization of V_2O_5-WO_3/TiO_2 De-NO_x Catalysts. *Journal of Catalysis* **1995**, *155*, 117–130.

[54] Chen, J.; Yang, R. Role of WO_3 in mixed V_2O_5-WO_3/TiO_2 catalysts for selective catalytic reduction of nitric oxide with ammonia. *Applied Catalysis A: General* **1992**, *80*, 135–148.

[55] Marberger, A.; Ferri, D.; Rentsch, D.; Krumeich, F.; Elsener, M.; Kröcher, O. Effect of SiO_2 on co-impregnated $V_2O_5/WO_3/TiO_2$ catalysts for the selective catalytic reduction of NO with NH_3. *Catalysis Today* **2019**, *320*, 123–132.

[56] Beale, A. M.; Lezcano-Gonzalez, I.; Maunula, T.; Palgrave, R. G. Development and characterization of thermally stable supported V–W–TiO_2 catalysts for mobile V_2O_5–SCR applications. *Catalysis, Structure and Reactivity* **2015**, *1*, 25–34.

[57] Lietti, L.; Svachula, J.; Forzatti, P.; Busca, G.; Ramis, G.; Bregani, F. Surface and Catalytic Properties of Vanadia-Titania and Tungsta-Titania Systems in the Selective Catalytic Reduction of Nitrogen Oxides. *Catalysis Today* **1993**, *17*, 131–140.

[58] Chapman, D. M.; Fu, G.; Augustine, S.; Watson, M.; Crouse, J.; Zavalij, L.; Perkins-Banks, D. New Titania Materials with Improved Stability and Activity for Vanadia-Based Selective Catalytic Reduction of NO_x. *SAE International Journal of Fuels and Lubricants* **2010**, *3*, 643–653.

[59] Kobayashi, M.; Kuma, R.; Masaki, S.; Sugishima, N. TiO_2-SiO_2 and V_2O_5/TiO_2-SiO_2 catalyst: Physico-chemical characteristics and catalytic behavior in selective catalytic reduction of NO by V_2O_5. *Applied Catalysis B: Environmental* **2005**, *60*, 173–179.

[60] Pan, Y.; Zhao, W.; Zhong, Q.; Cai, W.; Li, H. Promotional effect of Si-doped V_2O_5/TiO_2 for selective catalytic reduction of NO_x by V_2O_5. *Journal of Environmental Sciences* **2013**, *25*, 1703–1711.

[61] Yan, Z.; Shan, W.; Shi, X.; He, G.; Lian, Z.; Yu, Y.; Shan, Y.; Liu, J.; He, H. The way to enhance the thermal stability of V_2O_5-based catalysts for NH_3-SCR. *Catalysis Today* **2020**, *355*, 408–414.

[62] Jossen, R.; Heine, M. C.; Pratsinis, S. E.; Augustine, S. M.; Akhtar, M. K. Thermal stability and catalytic activity of flame-made silica-vanadia-tungsten oxide-titania. *Applied Catalysis B: Environmental* **2007**, *69*, 181–188.

[63] Marberger, A.; Elsener, M.; Nuguid, R. J. G.; Ferri, D.; Kröcher, O. Thermal activation and aging of a V_2O_5/WO_3-TiO_2 catalyst for the selective catalytic reduction of NO with NH_3. *Applied Catalysis A: General* **2019**, *573*, 64–72.

[64] Ye, B.; Jeong, B.; jin Lee, M.; Kim, T. H.; Park, S. S.; Jung, J.; Lee, S.; Kim, H. D. Recent trends in vanadium-based SCR catalysts for NOx reduction in industrial applications: stationary sources. *Nano Convergence* **2022**, *9*, DOI: 10.1186/s40580-022-00341-7.

[65] Wu, Z.; Jin, R.; Wang, H.; Liu, Y. Effect of ceria doping on SO_2 resistance of Mn/TiO_2 for selective catalytic reduction of NO with V_2O_5 at low temperature. *Catalysis Communications* **2009**, *10*, 935–939.

[66] Zhang, S.; Zhang, B.; Liu, B.; Sun, S. A review of Mn-containing oxide catalysts for low temperature selective catalytic reduction of NO_x with NH_3: reaction mechanism and catalyst deactivation. *RSC Adv.* **2017**, *7*, 26226–26242.

[67] Liu, Z.; Zhang, S.; Li, J.; Zhu, J.; Ma, L. Novel V_2O_5-CeO_2/TiO_2 catalyst with low vanadium loading for the selective catalytic reduction of NO_x by NH_3. *Applied Catalysis B: Environmental* **2014**, *158-159*, 11–19.

[68] Zhang, Y.; Zhu, X.; Shen, K.; Xu, H.; Sun, K.; Zhou, C. Influence of ceria modification on the properties of TiO_2-ZrO_2 supported V_2O_5 catalysts for selective catalytic reduction of NO by NH_3. *Journal of Colloid and Interface Science* **2012**, *376*, 233–238.

[69] Lian, Z.; Liu, F.; He, H.; Liu, K. Nb-doped VO_x/CeO_2 catalyst for NH_3-SCR of NO_x at low temperatures. *RSC Advances* **2015**, *5*, 37675–37681.

[70] Lian, Z.; Liu, F.; Shan, W.; He, H. Improvement of Nb Doping on SO_2 Resistance of VO_x/CeO_2 Catalyst for the Selective Catalytic Reduction of NO_x with NH_3. *Journal of Physical Chemistry C* **2017**, *121*, 7803–7809.

[71] Du, X.; Gao, X.; Fu, Y.; Gao, F.; Luo, Z.; Cen, K. The co-effect of Sb and Nb on the SCR performance of the V_2O_5/TiO_2 catalyst. *Journal of Colloid and Interface Science* **2012**, *368*, 406–412.

[72] Elbadawi, A. A. H.; Osman, M. S.; Razzak, S. A.; Hossain, M. M. VO_x-Nb/La-γAl_2O_3 catalysts for oxidative dehydrogenation of ethane to ethylene. *Journal of the Taiwan Institute of Chemical Engineers* **2016**, *61*, 106–116.

[73] Ye, D.; Qu, R.; Zheng, C.; Cen, K.; Gao, X. Mechanistic investigation of enhanced reactivity of NH_4HSO_4 and NO on Nb- and Sb-doped VW/Ti SCR catalysts. *Applied Catalysis A: General* **2018**, *549*, 310–319.

[74] Kwon, D. W.; Kim, D. H.; Lee, S.; Kim, J.; Ha, H. P. A dual catalytic strategy by the nature of the functionalization effect as well as active species on vanadium-based catalyst for enhanced low temperature SCR. *Applied Catalysis B: Environmental* **2021**, *289*, 120032.

[75] Kumar, P. A.; Jeong, Y. E.; Ha, H. P. Low temperature NH_3-SCR activity enhancement of antimony promoted vanadia-ceria catalyst. *Catalysis Today* **2017**, *293-294*, 61–72.

[76] Kleemann, M.; Elsener, M.; Koebel, M.; Wokaun, A. Investigation of the ammonia adsorption on monolithic SCR catalysts by transient response analysis. *Applied Catalysis B: Environmental* **2000**, *27*, 231–242.

[77] Kröcher, O.; Devadas, M.; Elsener, M.; Wokaun, A.; Söger, N.; Pfeifer, M.; Demel, Y.; Mussmann, L. Investigation of the selective catalytic reduction of NO by NH_3 on Fe-ZSM5 monolith catalysts. *Applied Catalysis B: Environmental* **2006**, *66*, 208–216.

[78] Thommes, M.; Kaneko, K.; Neimark, A. V.; Olivier, J. P.; Rodriguez-Reinoso, F.; Rouquerol, J.; Sing, K. S. Physisorption of gases, with special reference to the evaluation of surface area and pore size distribution (IUPAC Technical Report). *Pure and Applied Chemistry* **2015**, *87*, 1051–1069.

[79] Brunauer, S.; Emmett, P. H.; Teller, E. Adsorption of Gases in Multimolecular Layers. *Journal of the American Chemical Society* **1938**, *60*, 309–319.

[80] Lowell, S.; Shields, J. E.; Thomas, M. A.; Thommes, M. In *Characterization of Porous Solids and Powders: Surface Area, Pore Size and Density*; Springer Netherlands: Dordrecht, **2004**, pp 58–80.

[81] Bragg, W. H.; Bragg, W. L. The reflection of X-rays by crystals. *Proceedings of the Royal Society of London. Series A, Containing Papers of a Mathematical and Physical Character* **1913**, *88*, 428–438.

[82] L.E Smart, E. M., *Solid State Chemistry: An Introduction, Fourth Edition (4th ed.)*. CRC Press.: **2012**.

[83] Scherrer, P. Bestimmung der Größe und der inneren Struktur von Kolloidteilchen mittels Röntgenstrahlen. *Nachrichten von der Gesellschaft der Wissenschaften zu Göttingen, Mathematisch-Physikalische Klasse* **1918**, *2*, 98–100.

[84] Grünzler, H.; Gremlich, H., *IR Spectroscopy: An Introduction*; WILEY-VCH: **2002**.

[85] Larkin, P. In *Infrared and Raman Spectroscopy*; Elsevier: Oxford, **2011**.

[86] Harris, D., *Quantitative Chemical Analysis*; W. H. Freeman and Company, New York: **2010**.

[87] Meunier, F. Pitfalls and benefits of in situ and operando diffuse reflectance FT-IR spectroscopy (DRIFTS) applied to catalytic reactions. *Reaction Chemistry & Engineering* **2016**, *1*, 134–141.

[88] Paredes-Nunez, A.; Jbir, I.; Bianchi, D.; Meunier, F. C. Spectrum baseline artefacts and correction of gas-phase species signal during diffuse reflectance FT-IR analyses of catalysts at variable temperatures. *Applied Catalysis A: General* **2015**, *495*, 17–22.

[89] Velin, P.; Stenman, U.; Skoglundh, M.; Carlsson, P.-A. Portable device for generation of ultra-pure water vapor feeds. *Review of Scientific Instruments* **2017**, *88*, 115102.

[90] Hecht, E. In *Optics*; Pearson Education: **2017**.

[91] Michelson, A. A.; Morley, E. W. On the relative motion of the Earth and the luminiferous ether. *American Journal of Science* **1887**, *s3-34*, 333–345.

[92] Khoshhesab, Z. M., *Reflectance IR Spectroscopy*; Intech: **2012**.

[93] Bruker Optics VERTEX Series Research FT-IR Spectrometers: VERTEX 70/70v/80/80v/90v Brochure, `https://www.depts.ttu.edu/coe/research/mcc/documents/VERTEX_70-HYPERION_2000_22.pdf`, Accessed: 2025-08-20, 2008.

[94] Sirita, J.; Phanichphant, S.; Meunier, F. C. Quantitative analysis of adsorbate concentrations by diffuse reflectance FT-IR. *Analytical chemistry* **2007**, *79*, 3912–3918.

[95] Ferraro, J. R.; Nakamoto, K.; Brown, C. W., *Introductory Raman Spectroscopy (Second Edition)*, Second Edition; Academic Press: San Diego, **2003**.

[96] Christodoulakis, A.; Boghosian, S. Molecular structure and activity of molybdena catalysts supported on zirconia for ethane oxidative dehydrogenation studied by operando Raman spectroscopy. *Journal of Catalysis* **2008**, *260*, 178–187.

[97] Kentri, T.; Tsevis, A.; Boghosian, S. Heterogeneity of the vanadia phase dispersed on titania. Co-existence of distinct mono-oxo VO_x sites. *Dalton Trans.* **2023**, *52*, 7495–7511.

[98] Meier, R. J. On art and science in curve-fitting vibrational spectra. *Vibrational Spectroscopy* **2005**, *39*, 266–269.

[99] Bradley, M. *Curve Fitting in Raman and IR Spectroscopy: Basic Theory of Line Shapes and Applications*; **2007**.

[100] Burkardt, D. A.; Weisweiler, W.; can den Tillaart, J.; Schäfer-Sindlinger, A.; Lox, E. Influence of the V_2O_5 Loading on the Structure and Activity of V_2O_5/TiO_2 SCR Catalysts for Vehicle Application. *Topics in Catalysis* **2001**, *16*, 369–375.

[101] Kubacka, A.; Iglesias-Juez, A.; di Michiel, M.; Becerro, A. I.; Fernández-García, M. Morphological and structural behavior of TiO_2 nanoparticles in the presence of WO_3: Crystallization of the oxide composite system. *Physical Chemistry Chemical Physics* **2014**, *16*, 19540–19549.

[102] Saleh, R. Y.; Wachs, I. E.; Chan, S. S.; Chersich, C. C. The interaction of V_2O_5 with TiO_2(anatase): Catalyst evolution with calcination temperature and O-xylene oxidation. *Journal of Catalysis* **1986**, *98*, 102–114.

[103] Oliveri, G.; Ramis, G.; Buscaa, G.; Sanchez Escribanob, V. Thermal Stability of Vanadia-Titania Catalysts. *J. Mater. Chem* **1993**, *3*, 1239–1249.

[104] Won, J. M.; Kim, M. S.; Hong, S. C. The cause of deactivation of VO_x/TiO_2 catalyst by thermal effect and the role of tungsten addition. *Chemical Engineering Science* **2021**, *229*, 116068.

[105] Went, G. T.; Leu, L. J.; Lombardo, S. J.; Bell, A. T. Raman spectroscopy and thermal desorptlon of NH_3 adsorbed on TiO_2 (anatase)-supported V_2O_5. *Journal of Physical Chemistry* **1992**, *96*, 2235–2241.

[106] Srnak, T. Z.; Dumesic, J. A.; Clausen, B. S.; Törnqvist, E.; Topsøe, N. Y. Temperature-programmed desorption/reaction and in situ spectroscopic studies of vanadia/titania for catalytic reduction of nitric oxide. *Journal of Catalysis* **1992**, *135*, 246–262.

[107] Bredow, T.; Homann, T.; Jug, K. Adsorption of NO, NH_3 and H_2O on V_2O_5/TiO_2 catalysts. *Res. Chem. Intermed* **2004**, *30*, 65–73.

[108] Lai, J.-K.; Jaegers, N. R.; Lis, B. M.; Guo, M.; Ford, M. E.; Walter, E.; Wang, Y.; Hu, J. Z.; Wachs, I. E. Structure-Activity Relationships of Hydrothermally Aged Titania-Supported Vanadium-Tungsten Oxide Catalysts for SCR of NO_x Emissions with NH_3. *ACS Catalysis* **2021**, *11*, 12096–12111.

[109] Went, G. T.; Leu, L.-J.; Bell, A. T. Quantitative structural analysis of dispersed vanadia species in TiO_2(anatase)-supported V_2O_5. *Journal of Catalysis* **1992**, *134*, 479–491.

[110] Machej, T.; Haber, J.; M. Turek, A.; E. Wachs, I. Monolayer V_2O_5/TiO_2 and MoO_3/TiO_2 catalysts prepared by different methods. *Applied Catalysis* **1991**, *70*, 115–128.

[111] Tian, F.; Zhang, Y.; Zhang, J.; Pan, C. Raman Spectroscopy: A New Approach to Measure the Percentage of Anatase TiO_2 Exposed (001) Facets. *The Journal of Physical Chemistry C* **2012**, *116*, 7515–7519.

[112] Mukherjee, S. K.; Mergel, D. Thickness dependence of the growth of magnetron-sputtered TiO_2 films studied by Raman and optical transmittance spectroscopy. *Journal of Applied Physics* **2013**, *114*, 013501.

[113] Pittman, R. M.; Bell, A. T. Raman Studies of the Structure of Nb2O5/TiO_2. *J. Phys. Chem* **1993**, *97*, 12178–12185.

[114] Mazza, T; Barborini, E; Piseri, P; Milani, P; Cattaneo, D; Li Bassi, A.; Bottani, C. E.; Ducati, C Raman spectroscopy characterization of TiO_2 rutile nanocrystals. *Physical Review B - Condensed Matter and Materials Physics* **2007**, *75*, 045416.

[115] Čičmanec, P.; Ganjkhanlou, Y.; Kotera, J.; Hidalgo, J. M.; Tišler, Z.; Bulánek, R. The effect of vanadium content and speciation on the activity of VO_x/ZrO_2 catalysts in the conversion of ethanol to acetaldehyde. *Applied Catalysis A: General* **2018**, *564*, 208–217.

[116] Tang, C.; Zhang, H.; Dong, L. Ceria-based catalysts for low-temperature selective catalytic reduction of NO with NH_3. *Catalysis Science and Technology* **2016**, *6*, 1248–1264.

[117] Opara Krašovec, U; Orel, B; Šurca, A; Bukovec, N; Reisfeld, R Structural and spectroelectrochemical investigations of tetragonal $CeVO_4$ and Ce/V-oxide sol-gel derived ion-storage films. *Solid State Ionics* **1999**, *118*, 195–214.

[118] Wachs, I. E. and Jehng, J. M. and Deo, G. and Hu, H. and Arora, N. Redox properties of niobium oxide catalysts. *Catalysis Today* **1996**, *28*, 199–205.

[119] Guerrero-Pérez, M. O.; Fierro, J. L. G.; Bañares, M. A. Effect of synthesis method on stabilized nano-scaled Sb–V–O catalysts for the ammoxidation of propane to acrylonitrile. *Topics in Catalysis* **2006**, *41*, 43–53.

[120] Olga Guerrero-Pérez, M.; Fierro, J. L. G.; Bañares, M. A. Niobia-supported Sb–V–O catalysts for propane ammoxidation: effect of catalyst composition on the selectivity to acrylonitrile. *Phys. Chem. Chem. Phys.* **2003**, *5*, 4032–4039.

[121] Golinska-Mazwa, H.; BRojas, E.; López-Medina, R.; Ziolek, M.; Bañares, M. A.; Guerrero-Pérez, M. O. Niobiosilica Materials as Attractive Supports for Sb–V–O Catalysts. *Topics in Catalysis* **2012**, *55*, 837–845.

[122] Hadjiivanov, K.; Lamotte, J.; Lavalley, J. C. FTIR study of low-temperature CO adsorption on pure and ammonia-precovered TiO_2 (anatase). *Langmuir* **1997**, *13*, 3374–3381.

[123] Fernández-García, M.; Belver, C.; Hanson, J. C.; Wang, X.; Rodriguez, J. A. Anatase-TiO_2 nanomaterials: Analysis of key parameters controlling crystallization. *Journal of the American Chemical Society* **2007**, *129*, 13604–13612.

[124] Busca, G.; Marchetti, L.; Centi, G.; Trifirò, F. Surface characterization of a grafted vanadium-titanium dioxide catalyst. *Journal of the Chemical Society, Faraday Transactions 1: Physical Chemistry in Condensed Phases* **1985**, *81*, 1003–1014.

[125] Giraud, F.; Geantet, C.; Guilhaume, N.; Loridant, S.; Gros, S.; Porcheron, L.; Kanniche, M.; Bianchi, D. Experimental Microkinetic Approach of De-NO_x by NH_3 on $V_2O_5/WO_3/TiO_2$ Catalysts. 2. Impact of Superficial Sulfate and/or V_xO_y Groups on the Heats of Adsorption of Adsorbed NH_3 Species. *The Journal of Physical Chemistry C* **2014**, *118*, 15677–15692.

[126] Saur, O.; Bensitel, M.; Saad, A.; Lavalley, J.; Tripp, C. P.; Morrow, B. The structure and stability of sulfated alumina and titania. *Journal of Catalysis* **1986**, *99*, 104–110.

[127] Burcham, L. J.; Datka, J.; Wachs, I. E. In Situ Vibrational Spectroscopy Studies of Supported Niobium Oxide Catalysts. *Journal of Physical Chemistry B* **1999**, *103*, 6015–6024.

[128] Li, P.; Xin, Y.; Li, Q.; Wang, Z.; Zhang, Z.; Zheng, L. Ce-Ti amorphous oxides for selective catalytic reduction of NO with NH_3: Confirmation of Ce-O-Ti active sites. *Environmental Science and Technology* **2012**, *46*, 9600–9605.

[129] Eppler, R. A. Effect of Antimony Oxide on the Anatase-Rutile Transformation in Titanium Dioxide. *Journal of the American Ceramic Society* **1987**, *70*, 64–66.

[130] Hadjiivanov, K. I. Identification of neutral and charged N_xO_y surface species by IR spectroscopy. *Catalysis Reviews - Science and Engineering* **2000**, *42*, 71–144.

[131] Azambre, B.; Zenboury, L.; Koch, A.; Weber, J. V. Adsorption and desorption of NO_x on commercial ceria-zirconia ($Ce_xZr_{1-x}O_2$) mixed oxides: A combined TGA, TPD-MS, and DRIFTS study. *Journal of Physical Chemistry C* **2009**, *113*, 13287–13299.

[132] Hadjiivanov, K.; Bushev, V.; Kantcheva, M.; Klissurski, D. Infrared Spectroscopy Study of the Species Arising during NO_2 Adsorption on TiO_2 (Anatase). *Langmuir* **1994**, *10*, 464–471.

[133] Hadjiivanov, K.; Knözinger, H. Species formed after NO adsorption and NO + O_2 co-adsorption on TiO_2: An FTIR spectroscopic study. *Physical Chemistry Chemical Physics* **2000**, *2*, 2803–2806.

[134] Müller, P.; Hermans, I. Applications of Modulation Excitation Spectroscopy in Heterogeneous Catalysis. *Industrial & Engineering Chemistry Research* **2017**, *56*, 1123–1136.

[135] Thomas, J. M.; Thomas, W. J., *Principles and Practice of Heterogeneous Catalysis*; Wiley-VCH: **2014**.

[136] Wu, B.; Zhang, S.; Huang, M.; Zhang, S.; Liu, B.; Zhang, B. Theoretical insight into H_2O impact on V_2O_5/TiO_2 catalysts for selective catalytic reduction of NO_x. *Physical Chemistry Chemical Physics* **2024**, *26*, 14651–14663.

[137] Takeuchi, M.; Martra, G.; Coluccia, S.; Anpo, M. Investigations of the structure of H_2O clusters adsorbed on TiO_2 surfaces by near-infrared absorption spectroscopy. *Journal of Physical Chemistry B* **2005**, *109*, 7387–7391.

[138] Soria, J.; Sanz, J.; Sobrados, I.; Coronado, J. M.; Maira, A. J.; Hernández-Alonso, M. D.; Fresno, F. FTIR and NMR study of the adsorbed water on nanocrystalline anatase. *Journal of Physical Chemistry C* **2007**, *111*, 10590–10596.

[139] Kevorkyants, R.; Rudakova, A. V.; Chizhov, Y. V.; Bulanin, K. M. The origin of 1560 cm-1 band in experimental IR spectra of water adsorbed on TiO_2 surface: Ab initio assessment. *Chemical Physics Letters* **2016**, *662*, 97–101.

[140] Falk, M. The frequency of the H-O-H bending fundamental in solids and liquids. *Spectrochimica Acta Part A: Molecular Spectroscopy* **1984**, *40*, 43–48.

[141] Volp, G.; Grassian, V. H. Role(s) of adsorbed water in the surface chemistry of environmental interfaces. *Chemical Communications* **2013**, *49*, 3071–3094.

[142] Topsøe, N. Y.; Slabiak, T.; Clausen, B. S.; Srnak, T. Z.; Dumesic, J. A. Influence of water on the reactivity of vanadia/titania for catalytic reduction of NO_x. *Journal of Catalysis* **1992**, *134*, 742–746.